Introduction

At the time of this writing the physics responsible for the superconductivity of copper oxide compound materials is still not understood and object of very exciting research. Different theories have been proposed to explain the reason of a so high *critical temperature* in such superconductors, but none of them has been capable to fully predict the broad range of phenomena related to this phase transition. The scientific community seems to agree on one thing: the definition of the symmetry of the order parameter in high-T_C superconductors is the first fundamental prerequisite for a full comprehension of the physics of these compounds.

The realization of junctions with Josephson properties has been responsible for great improvements in understanding high-T_C superconductors. We will focus, among the different technologies capable of producing junctions with high-T_C compounds, especially on the so called *grain boundary junctions*, realized by carefully engineering the grain boundary between two diversely oriented crystals of superconducting compound. Because of the high anisotropy of the order parameter, it is possible to realize a weak-coupling between the superconducting order parameter in the two electrodes, necessary condition for the onset of the Josephson effect.

The realization of such junctions has allowed experiments [1, 2] which determined, once for all, the presence of the d-wave symmetry as dominant component of the order parameter in most copper-oxide based superconductors. In particular, experiments performed on grain boundary junctions realized with $YBa_2Cu_3O_{7-\delta}$ — i.e. the superconductor employed in this thesis work — have given evidence of the presence of a $s + d$-wave admixture[3] of the superconducting order parameter. Anyway, according to theory[4] any complex linear combination of d-wave and s-wave is possible and, therefore, the presence of an imaginary s-wave component of the order parameter should not to be excluded. Moreover, the existence of such component would be very interesting for the realization of an artificial two level system, based on the quantum dynamics of single Josephson junctions.
To better understand the physics of cuprate compound superconductors, different experiments have been proposed and realized, all of them sharing

the capability of mapping directly the superconducting order parameter in the different directions of the momentum space. Within such framework, we propose the realization of a Single Electron Transistor realized with high-T_C grain boundary junctions. This work tries to understand if two technologies used to realize grain boundary junctions — YBCO/YSZ bicrystal technology and YBCO/STO/MgO biepitaxial technology — are suitable for such single-electronics application.

A Single Electron Transistor (SET) is constituted by a series of two small Josephson junctions capacitively coupled to a gate electrode. The physical principle which enables its operation is the *Coulomb blockade of tunneling*, i.e. the impossibility of tunneling single electrons through the junctions because of the effect of the Coulomb repulsion. For the Coulomb blockade of tunneling to be effective, every tunnel junction has to comply two fundamental constraints.

- The junction's normal resistance R_N — i.e. the resistance of the junction measured at very high bias voltages — has to be higher than 25 kΩ, so that quantum fluctuations are ineffective in promoting tunneling events.

- For thermal fluctuations to be unsuccessful in fostering single electron tunneling, the capacitance of each junction has to be smaller than $e^2/2K_BT$. To give an idea of the order of magnitude, such capacitance should be smaller than 1 fF for temperatures close to 1 K.

Understanding whether the realization of an SET is feasible or not in a given technological platform means trying to understand if it is possible to realize junctions which satisfy the above mentioned restrictions. To characterize the normal resistance of the grain boundary Josephson junctions a simple measurement of the current-voltage characteristic of the junction can be used. On the other hand, measuring junction capacitances of the order of 1 fF is not straightforward.

In this work, the junction capacitance has been extracted from the measurement of the current-voltage characteristics of *Superconducting Quantum Interference Devices*(SQUID), acquired at different values of the external magnetic field. A SQUID is constituted by two Josephson junctions connected by two superconducting leads in a ring-like geometry. By applying an external magnetic field it is possible to strongly modify the current-voltage characteristic of the device and generate AC circulating currents in the loop which, under certain circumstances, can interfere non linearly with the LC resonator formed by the superconducting ring inductance and the junction capacitances. At evenly spaced values of the magnetic flux linked to the loop, such interaction can cause a current step to appear in the current voltage characteristic of the SQUID. The voltage at which such step occurs is related to the product LC. By estimating the SQUID inductance by separate means, it is possible to have an accurate measurement of the capacitance of the junctions of the SQUID. Such capacitances can further be used, together with the information of the normal resistance, to understand the biggest cross-section of a junction which permits to realize a Single Electron Transistor.

In the following chapters we will:

1. give a brief overview of the physics of superconductors, of the SETs and of the SQUIDs, with a detailed description on possible interactions between the SQUID and LC resonators (Chapter 1),

2. describe briefly the fabrication procedure and the measurement setup used to realize and characterize SQUIDs and SET prototypes (Chapter 2),

3. summarize the most significant results of the SQUID characterization together with the measurements of the SET prototypes, concluding with a suggestion for a junction dimension suitable for high-T_C single electronics applications (Chapter 3).

Contents

1 Superconductivity and Josephson Devices **1**
1.1 Electrodynamics of Superconductors 1
1.1.1 London equations and Meissner Effect 2
1.1.2 Kinetic inductance 3
1.2 Cuprate Superconductors 4
1.2.1 Crystal and electronic structure of YBCO 4
1.2.2 YBCO superconducting properties 5
1.3 Quasi-particle tunneling 7
1.4 Josephson relations 8
1.4.1 Magnetic field effect on a single junction: Fraunhofer pattern 11
1.4.2 Wide junction limit: the Sine-Gordon equation 12
1.5 The RCSJ model 13
1.5.1 The small capacitance limit: RSJ model 14
1.5.2 Energy analysis of the RCSJ model 15
1.6 DC SQUID 18
1.6.1 A constrain on the Junction phase differences 18
1.6.2 Negligible self-inductance case 20
1.6.3 Finite self-inductance case 21
1.7 High-T_C junctions 23
1.8 Single Electron Transistor 24
1.8.1 A normal-metal SET 26
1.8.2 A BCS-Superconductor SET 27
1.8.3 The high-T_C challenge 28
1.9 SQUID resonances 29
1.10 External LC resonance 31

2 Device fabrication **37**
2.1 Grain boundary Josephson junctions 37
2.1.1 Bicrystal technology 37
2.1.2 Biepitaxial deposition 38

2.2 Substrate Choice 43
2.3 Device design and Simulation 44
2.4 Device fabrication 50
2.4.1 Electron beam lithography 50
2.4.2 Lift-off 50
2.4.3 Grain-boundary compensation 51
2.4.4 Amorphous carbon mask and YBCO patterning . . . 53
2.5 Measurement Setup 56

3 Results and discussion 61
3.1 SQUID measurements 61
3.2 SET measurements 75

4 Conclusions 83

A Electron beam lithography 85

B Lift-off 89

C Other fabrication parameters 91

Chapter 1

Superconductivity and Josephson Devices

The following chapter is meant to give an overview of the fundamentals of superconductor electrodynamics and to discuss the basic elements of the superconducting electronic devices. We will try to explain with some detail how a single electron transistor can be used to measure directly the amplitude of the superconducting order parameter and, finally , we will treat the SQUID and Single junction interactions with LC resonators — which constitute the main tool for the junction capacitance analysis used in this work.

1.1 Electrodynamics of Superconductors

In 1911, not long time after ^{4}He was liquefied for the first time, H. Kamerling Onnes observed an abrupt loss of resistance in Mercury. Such phenomenon, called superconductivity, has been found in many metallic elements as well as compounds at very low temperatures. It took more than fifty years for the phenomenon to be explained from the theoretical point of view. Shortly after the demonstration by Leon Cooper of the instability of the Fermi sea under a weak attractive interaction, which could lead to the formation of a bound state, in 1957 Bardeen Cooper and Shrieffer published their theory of superconductivity. Before that, however, Heinz and Fritz London had proposed a simple theory to describe the electrodynamics of a superconducting metal

1.1.1 London equations and Meissner Effect

According to the London theory, the current in a superconductor can be modeled as the sum of a *normal current* $\mathbf{J_N}$, described by the Ohm's law, and a *super-current* $\mathbf{J_S}$, caused by paired-electrons — also known as *Cooper-pairs*. The Cooper pairs behave as Bose particles and are described by a macroscopic order parameter ψ, characterized by a well defined density n_S and phase θ:

$$\psi = \sqrt{n_S}\, e^{i\theta}, \tag{1.1}$$

To describe the electrodynamics of such a Bose condensate, we recall that the quantum-mechanical expectation value of the canonical momentum is linked to the phase gradient of ψ through the equation:

$$\mathbf{p} = \hbar \nabla \theta$$

and that the mechanical momentum $m\mathbf{v_S}$, the canonical momentum $\mathbf{p}$ of the Cooper-pairs and the vector potential $\mathbf{A}$ of the magnetic field are related through the expression:

$$\hbar \nabla \theta = m\mathbf{v_S} + 2e\mathbf{A} \tag{1.2}$$

Expressing the supercurrent density $\mathbf{J_S}$ in terms of the Cooper-pair velocity $\mathbf{v_S}$,

$$\mathbf{J_S} = 2e\, n_S\, \mathbf{v_S}$$

we can describe the electrodynamics of the super-current through the fundamental equation:

$$\hbar \nabla \theta = 2e \left\{ \Lambda \mathbf{J_S} + \mathbf{A} \right\} \qquad \text{where} \qquad \Lambda = \frac{m}{4e^2\, n_S} \tag{1.3}$$

The equation (1.3) describes the link between the phase, current and magnetic field and will be employed frequently to describe the behavior of the Cooper-pair electrodynamics while discussing the superconducting devices.

To obtain the first London equation it's enough to consider the Newton equation for the collisionless fluid of Cooper-pairs under the action of the electric field. Using the quantities defined in the fundamental relation (1.3), we can express the first London equation as:

$$\Lambda \frac{d\mathbf{J_S}}{dt} = \mathbf{E} \tag{1.4}$$

The second London equation is obtained from (1.3), taking the rotor of both members and recalling the definition of vector potential:

$$\Lambda\ \nabla \times \mathbf{J_S} + \mathbf{B} = \mathbf{0} \tag{1.5}$$

It is interesting to note how the current density behavior is affected directly by the external magnetic field while the electric field influences only its time variation.

The set formed by the Maxwell equations and the London equations fully describe the electrodynamics of a superconductor. In particular this set predicts the most striking feature of the superconductivity, know as the *Meissner effect*[1], i.e. the ability to expel the magnetic field from the bulk of a superconductor.
Let's consider, for simplicity, a superconductor extending in $z > 0$, with the x-y plane as interface between metal and vacuum. Justified by symmetry reasons, we can use as ansatz solution $\mathbf{B} = \mathbf{B}(z)$. In quasi-static conditions the solution of the set of Maxwell and London Equations will have the form $\mathbf{B} = B\hat{x}$ and, inside the superconductor, has to satisfy:

$$\partial_z^2 B = \frac{B}{{\lambda_L}^2} \quad \text{, where} \quad \lambda_L = \sqrt{\frac{\Lambda}{\mu_0}} \tag{1.6}$$

Thereby, $B(z)$ has to decay exponentially in z with characteristic length λ_L. Therefore the superconductor minimizes its free energy by expelling the magnetic field outside the bulk, permitting it to penetrate only for some units of λ_L that, for this reason, is called *London penetration depth.*

1.1.2 Kinetic inductance

The fundamental relation (1.3) has a direct interpretation. We can create a phase difference $\nabla\theta$ across two points of a superconductor through the application of a magnetic field, represented here by the vector potential $\mathbf{A}$, or by means of a current $\mathbf{J_S}$.

At zero external magnetic field, we can write the phase difference $\Delta\theta$ across the two electrodes as the sum of two contributions:

$$\Delta\theta = (L_{geom} + L_{kin})I \tag{1.7}$$

The first factor, i.e. the traditional geometric inductance L_{geom}, is obtained through the integration of the vector potential and is strongly affected by the geometry of the circuit. The second factor L_{kin}, called *kinetic inductance*, is a direct consequence of the collisionless behavior of the supercurrent and its ability to act as a kinetic energy reservoir. From the first London equation we can calculate the *kinetic energy density* $\mathcal{E}_{kin}$ of the Cooper-pairs as:

$$\mathcal{E}_{kin} = \int \mathbf{E} \cdot \mathbf{J_S} \, dt = \frac{\mu_0}{2} {\lambda_L}^2 \|\mathbf{J_S}\|^2 \tag{1.8}$$

[1] after Meissner and Ochsenfeld who discovered the magnetic field expulsion in 1933

The kinetic inductance is proportional to the square of *the London penetration depth* λ_L. In superconducting devices with dimensions smaller than 10 µm and $\lambda_L \approx$1 µm, the kinetic inductance can give non-negligible contributions to the dynamics of a superconducting device.

1.2 Cuprate Superconductors

In 1986 Bednorz and Müller at IBM Zürich Research Labs discovered a material, the $La_{1.85}Ca_{0.15}CuO_4$, with an exceptionally high critical temperature of 30 K. The T_C was high enough to suggest that the established formalism of BCS theory could not be used in a straightforward way to explain the behavior of such material. Since then many materials with still higher T_C has been found, all of them sharing a perovskite-like structure containing copper oxide planes. Shortly after the first high-T_C superconductor discovery, Wu and coworkers [5] introduced the $YBa_2Cu_3O_{7-\delta}$, frequently called YBCO. With a T_C of 93 K, this material has been the first compound with a superconducting transition above the boiling point of liquid nitrogen. The YBCO compound has been, and still is, subject of intense research, especially regarding the possibility of manufacturing cables and depositing thin film for the fabrication of Josephson junctions and electronic applications.

YBCO thin films has been used for the realization of the devices this thesis is focused on. In this section the crystal and electronic structure, as well as the superconducting properties of this material will be discussed.

1.2.1 Crystal and electronic structure of YBCO

The crystal structure of YBCO can be obtained stacking three different perovskite cells on top of each other. Copper occupies the vertices of every cubic cell while oxygen occupies the mid-point on the edges of each cube. The central perovskite cell contains an yttrium atom in the body centered position, while the neighbor cells have barium in the same position.
Oxygen vacancies are present on the central plane of the yttrium-centered cell, as well as in the edges directed along the a-axis. Such type of vacancy is responsible for the orthorhombic symmetry of the cell and contributes to the anisotropy in the electronic properties of the material. Copper is found as doubly and triply ionized cations and is, together with the oxygen cation O^{2-}, the main source of mobile charge carriers due to the formation of CuO_2 planes and the CuO chains running in the $\hat{b}$ direction. Yttrium cation Y^{3+} and barium cation Ba^{2+} ensure the unit cell to be electrically neutral. Optimally doped YBCO is obtained changing the concentration of oxygen in the CuO chains.

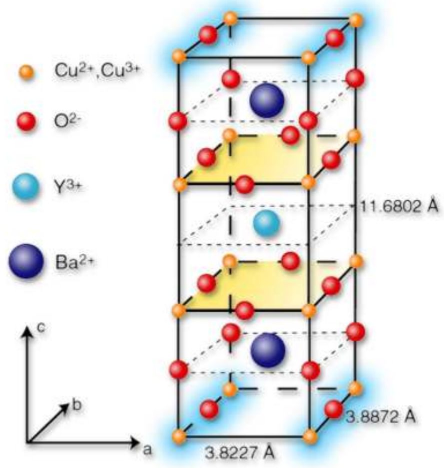

Figure 1.1: YBCO unitary cell structure. Copper oxide planes and chains are highlighted respectively in yellow and blue

The unit cell is 11Å high and about 3.8Å wide in both a and b directions because of rearrangement of the cell after the oxygen vacancy. Crystals are usually grown at high temperature, where structures are tetragonal. Therefore, at room temperature, the crystal develops stresses within the a-b plane which cause onset of the so called *twinning* — i.e. the crystal develops twin boundaries along the [110] which cause the CuO chains to switch orientation from the $\hat{b}$ to the $\hat{a}$ direction.
The atoms located outside the copper oxide chains and planes can be well described as fully ionic, with electrons tightly bound to localized states far from the Fermi Energy. These localized states will contribute to the electrical properties only acting as charge reservoir for both n or p-type doping of the Copper oxide planes and chains.

Therefore YBCO has small dispersion and poor conduction along c-axis and, in untwinned crystals, a considerable anisotropy in the resistivity along the a-b plane. Moreover, the carrier density is relatively low and is the cause for Coulomb repulsion to be very effective in coupling electrons in comparison with ordinary metals.

1.2.2 YBCO superconducting properties

The strong anisotropy in normal state electronic properties and crystal structure constitute the base for very unusual properties of the material in the superconducting state [6]. The behavior of the superconducting order parameter in the c-axis direction is still not well understood. At the

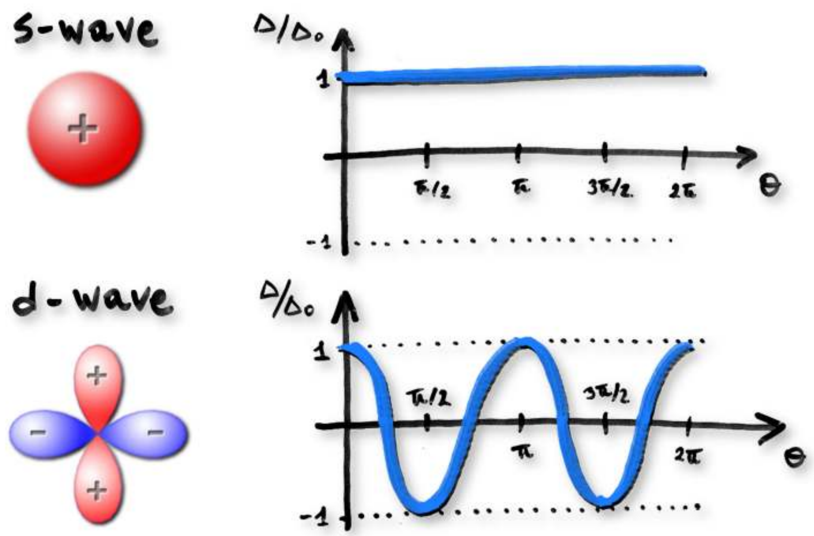

Figure 1.2: Comparison between BCS s-wave and d-wave order parameter.

time of this writing, some part of the scientific community believes in the presence of a weak coupling between distinct CuO_2 planes, forming intrinsic Josephson junctions, while others believe in the existence of an imaginary part of the order parameter with a fully developed gap, characterized by a very small amplitude in the c-axis direction. However CuO_2 planes are unanimously considered to be, together with the CuO chains, the seed of superconductivity in the compound. It is within the a-b planes that the biggest differences with traditional BCS superconductivity appear. The YBCO, like all cuprate superconductors, is characterized by d-wave symmetry of the order parameter, i.e. a four-lobed shape with sign change under rotation of $\pi/2$:

$$\Delta(\mathbf{k}) = \Delta_0 \mathbf{k} \cdot (\mathbf{a} - \mathbf{b}) \tag{1.9}$$

YBCO is characterized by a very short coherence length ξ — which is the distance on which Cooper pairs maintain phase coherence[2]. This feature makes YBCO extremely sensitive to both impurity concentrations and grain boundaries, and has hindered the fabrication of good Josephson junctions for long time because of the high sensitivity to the fabrication treatments. The counterpart of the nanometer-sized coherence length is the very long magnetic penetration depth λ, that ranges from 150 nm in the a-b planes up to 1.3 µm[3] and above along the c-axis [6].

[2]The short coherence length constrain is of fundamental nature since $\xi \sim \dfrac{\hbar v_F}{\Delta}$

[3]the value of λ_L along the c-axis depends strongly on the oxygen content of the material.

Material	T_C	Δ/e	λ	ξ
Pb	7.19 K	1.36 mV	39 nm	83 nm
Nb	9.25 K	1.57 mV	44 nm	40 nm
Al	1.175 K	170 µV	16 nm	1.6 µm
$\mathbf{YBa_2Cu_3O_{7-\delta}}$	93 K	15 mV	1.30 µm, c 150 nm, a-b	0.3 nm, c 1.5 nm, a-b

Table 1.1: Comparison between the superconducting properties of BCS type superconductors and YBCO [6]

Because of the large value of the ratio ξ/λ, YBCO is very well described by the London theory of superconductivity.

1.3 Quasi-particle tunneling

The following section is focused on showing how the traditional picture of electron and hole tunneling changes when a superconductor is used to realize a tunneling junction.

Let's consider at first a tunnel junction, which is constituted by two normal metal leads separated by a thin insulating barrier. The tunneling process can be represented by the creation of a hole-excitation in one of the leads, followed by the creation of an electron-excitation in the other one.
Under thermal equilibrium conditions the Fermi energy is equal in both leads. When a finite voltage is applied to the junction, the equilibrium condition is broken and it is possible to show that the current density J due to the tunneling transitions from both the left to the right lead, and vice versa, can be expressed as [7]:

$$J = \frac{2\pi e}{\hbar} \int_{-\infty}^{\infty} |\,T|^2 \; N_R(\epsilon - eV)\, N_L(\epsilon) \;\; [f(\epsilon - eV) - f(\epsilon)] \;\, d\epsilon \qquad (1.10)$$

where

- T is the tunneling matrix element,
- $N_R(\epsilon)$ and $N_L(\epsilon)$ are the density of excitation states in the right and left lead respectively,
- $f(\epsilon)$ is the Fermi distribution function, describing the average occupation number for the electron excitations[4],
- V is the applied voltage, and

[4]to describe an hole excitation $1 - f$ is used

- ϵ is electron excitation energy.

The expression (1.10) is quite general and can be employed to describe the tunneling both in normal metals and in superconductors. For normal metal junction, the density of excited states N_R and N_L are well approximated by a constant and, by integrating (1.10), a linear Ohm's law dependence of the current-voltage characteristic is obtained. When superconductors are employed in the tunnel junction, a different density of *quasi-particle excitation* states $D(\epsilon)$ has to be used. In BCS superconductors, such density has an energy dependence similar to the one shown in figure 1.3 and is well described by the equation:

$$D(\epsilon) = \begin{cases} \frac{N_F\,\epsilon}{\sqrt{\epsilon^2-\Delta^2}} & , |\epsilon| > \Delta \\ 0 & , |\epsilon| < \Delta \end{cases} \tag{1.11}$$

The equation 1.11 holds at temperatures close to 0 K, where the Fermi distribution is well approximated by an Heaviside step function. Introducing the density of states (1.11) in the expression (1.10) and proceeding with the integration, a strongly non linear current voltage characteristics is obtained. Such IV curve, shown in figure 1.3(b), is characterized by:

- a region of zero conductivity, for voltages smaller than $V_{th} = 2\Delta/e$ — as expected from the the gap in the density of states;

- an abrupt transition to values of conductivity typical of a normal metal junction.

The picture we have given here, however, does not fully describe the current voltage characteristic, since also the electrons which condense into the pair-state can contribute to the current transport. This kind of current transport, correctly predicted by B.D. Josephson, is described by the *Josephson relations* and will be presented in the next section.

1.4 Josephson relations

Let us consider a tunnel junction made by two superconducting leads, separated by a thin insulating barrier. If any finite overlap exists between the order parameter of the two electrodes in the potential barrier, Cooper-pairs can tunnel from one lead to the other without an applied voltage difference. Such effect, first predicted by B.D. Josephson [8] and experimentally verified for the first time by P.W. Anderson and J.M. Rowell [9], constitutes the main building block of all superconducting electronics.

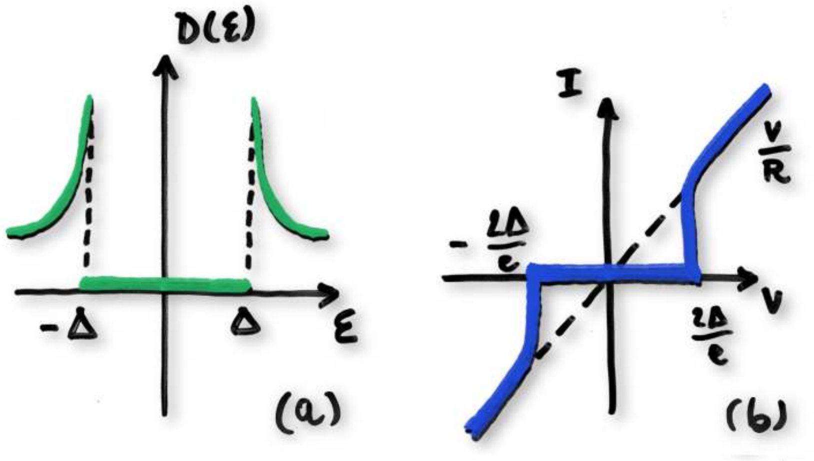

Figure 1.3: Density of excited states of BCS superconductor (a) and current-voltage characteristic for a superconducting tunnel junction (b). $D(\epsilon)$ is characterized by a fully developed energy gap and Von-Howe singularities at the energy gap Δ.

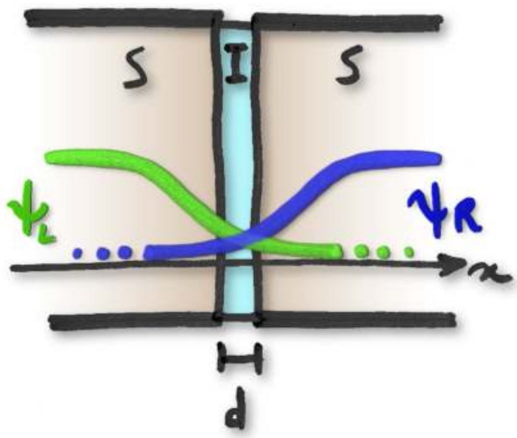

Figure 1.4: A superconducting tunnel junction. The order parameter of the two electrodes overlap, allowing the onset of the Josephson effect.

The time evolution of the Cooper-pair tunneling can be derived with the approach used by R. Feynman[10]. By using the expression (1.1) to describe the order parameter in both left and right lead and indicating with ϕ the difference between the phases of the two leads,

$$\phi = \theta_R - \theta_L$$

we can summarize the time evolution of the tunneling current J, flowing through the Josephson junction, with the *Josephson relations*:

$$J = J_c \sin\phi \tag{1.12}$$

$$\frac{d\phi}{dt} = \frac{2e}{\hbar} V \tag{1.13}$$

The *first Josephson relation* (1.12) predicts how the Cooper-pair tunneling current is influenced by the phase difference across the junction. The *second Josephson relation* (1.13) shows how the dynamics of such phase difference is affected by an voltage applied to the junction.
The parameter J_c, called *critical current density*, depends on the coupling matrix element K and on the densities of the Bose-condensate n_R and n_L in the left and right lead, with:

$$J_c = \frac{2eK}{\hbar}\sqrt{n_R n_L}$$

Under the hypothesis of uniform current distribution, we can operate a time integration of the current-voltage product and, using the Josephson relations, it is possible to calculate the energy gain of the junction due to the weak coupling [5]:

$$E_J = \int I_c \sin\phi \, \frac{\hbar}{2e}\frac{d\phi}{dt} \, dt = -\frac{\hbar}{2e} \, I_c \cos\phi \tag{1.14}$$

It is worth to point out that the behavior of a Josephson junction can be mapped into the problem of a *phase particle* moving in a periodic potential, called *washboard potential*. This very power full picture will be used further on in the chapter.

The characteristic of a Josephson junction is very non linear and this feature has made this device very interesting for electronics applications. However, for small values of ϕ, the junction can be nicely described as a simple lumped inductor, whose *Josephson inductance* L_J is given by:

$$L_J = \frac{\hbar}{2eI_c} \tag{1.15}$$

[5] we have discarded constant terms of the potential

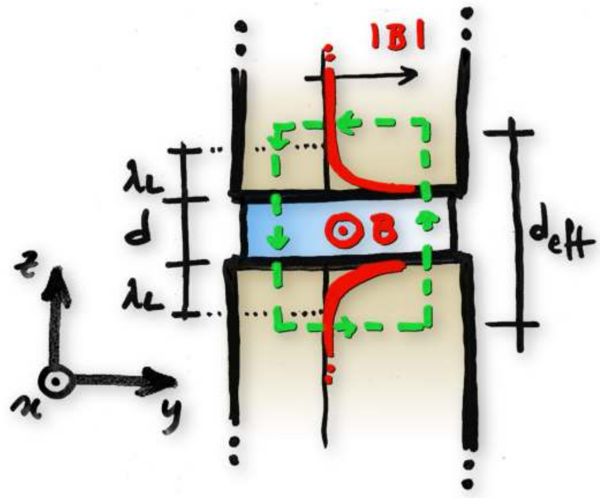

Figure 1.5: Path for the integration of the equation1.16

1.4.1 Magnetic field effect on a single junction: Fraunhofer pattern

The Josephson relations do not take into account the effect of a magnetic field linked to the junction. Nevertheless, the effect which the flux has on the junction can be predicted by integrating the fundamental relation (1.3) in a small circuit enclosing the junction, like the one shown in figure 1.5. As a result, the phase drop will has a spatial dependence in the direction normal to the magnetic field, described by the following equation:

$$\nabla\phi = \frac{2e}{\hbar} d_{eff} \left(\mathbf{n} \times \mathbf{B}\right) \tag{1.16}$$

where we have introduced the *effective thickness* of the junction with $d_{eff} \approx d + 2\lambda_L$. The phase variation across the junction plane will cause the Josephson current density to interfere with its components having different coordinate in the direction normal to the magnetic field.

In the simple case of a rectangular junction with a sinusoidal current phase relation — where $\mathbf{n}$ is directed toward $\hat{z}$ — immersed in a uniform magnetic field B — directed toward $\hat{x}$, as shown in figure (1.5) — it is possible to show that the critical current I_c depends on the flux Φ linked to the junction with:

$$I_c(\phi_y) = I_c(0) \left| \frac{\sin \phi_y/2}{\phi_y/2} \right| \qquad \text{,where} \quad \phi_y = 2\pi \frac{\Phi}{\Phi_0}$$

Where Φ is the total flux linked to the junction and Φ_0 is the flux quantum, defined as $\frac{h}{2e}$. The critical current interference pattern has the same shape

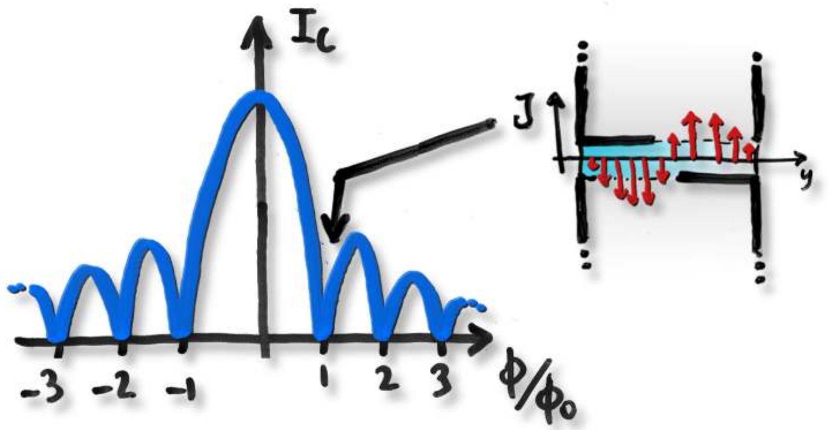

Figure 1.6: Critical current *Fraunhofer pattern* of a infinitely long junction. A sketch of the current distribution at one flux quantum is shown on the left.

of the interference pattern from an infinitely long rectangular slit. With a name borrowed from the rectangular slit diffraction pattern, the critical current pattern of such junction is called *Fraunhofer pattern*.

1.4.2 Wide junction limit: the Sine-Gordon equation

In the derivation of the Josephson relations we assume no variation of the phase within the plane of the junction. However, as far as the displacement currents and the inductive behavior of the superconducting leads is considered, spatial variations of the phase within the junction plane play a major role in the junction dynamics.
Forgetting for a moment about the Josephson effect, we incidentally notice the close resemblance between tunnel junction structure and the one of a wave-guide. Therefore, it is not surprising that the differential equations describing the electromagnetic field in our system have the form of a wave equation, where the Josephson currents act as a source of magnetic field. We can express the wave-equation for the Josephson wave-guide in terms of the phase $\phi(x, y)$ — function of the position (x, y) within the junction plane — and obtain the so called *Sine-Gordon equation*[7]:

$$\nabla^2_{xy}\phi - \frac{1}{\nu^2_{ph}}\partial^2_t\,\phi = \frac{\sin\phi}{\lambda^2_J} \tag{1.17}$$

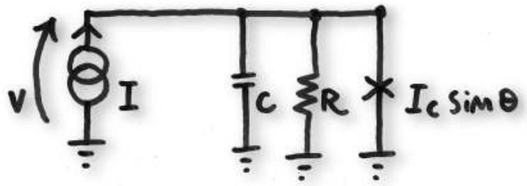

Figure 1.7: Lumped elements RCSJ model schematic of a Josephson junction. The element represented with a cross stands for an ideal Josephson element. Its characteristic is defined only by the critical current.

where the *Josephson penetration depth* λ_J and the *phase velocity* ν_{ph} are defined by:

$$\begin{cases} \nu_{ph} = \sqrt{\frac{1}{\epsilon\mu}\,\frac{d}{d_{eff}}} \\ \\ \lambda_J = \sqrt{\frac{\hbar/2e}{J_c\mu_0\,d_{eff}}} \end{cases}$$

If the time derivative term in equation (1.17) is neglected, the Sine-Gordon equation can be used to describe the phase distribution over the junction plane in the static case. Moreover, in the limit of small phase drops, the sinusoidal term can be linearized. The solution to such new equation are exponentially decaying with characteristic length λ_J.
We can interpret this result if we notice that, recalling (1.16), a phase variation is linked to the presence of a finite magnetic flux through the junction. Therefore, the Josephson currents act by screening the external and self-generated magnetic field like superconductors do. The phase drop over a junction can be approximated with a scalar all over the junction only if the smallest dimension of the junction is smaller than the Josephson penetration depth. Our devices will operate within this is the limit.

1.5 The RCSJ model

Within the small junction limit, the behavior of a Josephson junction can be fully described by a lumped elements model called Resistively Capacitively Shunted Junction or *RCSJ*. Such model uses, as the name itself suggests, a simple resistor R that describe the quasi-particle current and a lumped capacitor C describing the displacement currents in the junction. Both lumped elements shunt an ideal Josephson element, whose characteristic is described by the Josephson relations (1.12,1.13).

The dynamic system which describes the junction can be obtained from the Josephson relations and the Kirchoff current law, applied at the common circuital node:

$$\begin{cases} \frac{d\phi}{dt} = \frac{2e}{\hbar} V \\ \\ \frac{dV}{dt} = \frac{1}{C}\left[I - \frac{V}{R} - I_c \sin\phi\right] \end{cases} \tag{1.18}$$

Incidentally, we notice that the non-linear system in (1.18) describes the dynamics of a pendulum with inertia $\frac{\hbar C}{2e}$, subject to a damping force proportional to $\frac{\hbar}{2eR}$, under the action of both an externally applied torque I and the gravity torque $I_c \sin\phi$. This analogy can be very useful to understand the voltage current characteristic of a Josephson junction. To capitalize the analogy with the mechanical pendulum, it is worth renormalizing the system with internal units of time, current and voltage.

Following Stewart [11], McCumber [12, 13] and Johnson [14], we can use the $L_J C$ resonance frequency, otherwise called *plasma frequency* ω_J, as an embedded time unit while I_c and RI_c can be used as can be used as the unit of current and voltage. Starting from this set of units, it is possible to introduce — together with the *damping parameter* β_J — the normalized time τ, the normalized voltage η and the normalized bias current α:

$$\begin{gathered} \omega_J = \sqrt{\frac{2e}{\hbar}\frac{I_c}{C}} \\ \\ \beta_J = \frac{1}{\omega_J}\frac{1}{RC} \qquad\qquad \alpha = \frac{I}{I_c} \\ \\ \tau = \omega_J\, t \qquad\qquad \eta = \frac{V}{RI_c} = \beta_J \frac{d\phi}{d\tau} \end{gathered} \tag{1.19}$$

By using such quantities, the system (1.18) can be described by the following second order differential equation[6]:

$$\ddot{\phi} + \beta_J\,\dot{\phi} + \sin\phi = \alpha. \tag{1.20}$$

1.5.1 The small capacitance limit: RSJ model

The system (1.20) cannot be solved in closed form. However an analytical solution for the current-voltage characteristic can be found in the small capacitance limit $\beta_J \to \infty$. In the frame of the mechanical analog, the friction of the pendulum is so high that the effect of its inertia can almost be neglected and, for every given value of the torque α, the pendulum will reach promptly an equilibrium condition. In this limit we will talk about the *RSJ model*, since only the resistor will shunt the ideal Josephson junction. The equations of motion (1.19) can be written in the form:

$$\beta_J\,\dot{\phi} + \sin\phi = \alpha \tag{1.21}$$

[6]Note that we have used the Newton notation to indicate the normalized time derivative $\dot{f} = \frac{df}{d\tau}$

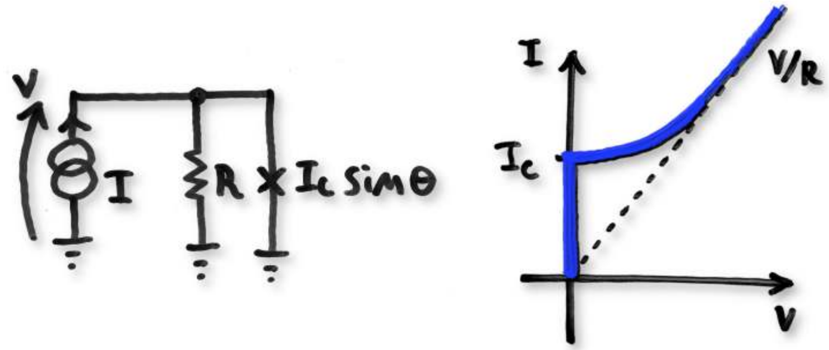

Figure 1.8: Lumped elements model and a typical current-voltage characteristic of a RCSJ model.

and solved by separation of variables. To obtain the current-voltage characteristic predicted by the model, we can calculate how the average voltage $\langle\eta\rangle$ changes as a function of the bias current α, obtaining a very simple relation:

$$\langle\eta\rangle = \beta_J \langle\dot{\phi}\rangle = \sqrt{\alpha^2 - 1} \tag{1.22}$$

which, in physical units, can be written as:

$$V = \begin{cases} 0 & , \quad I \leq I_c \\ \\ R\, I_c \sqrt{\left(\frac{I}{I_c}\right)^2 - 1} & , \quad I > I_c \end{cases} \tag{1.23}$$

The Josephson junction does not develop any DC voltage whenever the current, biasing the junction, is smaller than the critical current. When I_c is exceeded, a non zero DC voltage develops across the junction, tracing an hyperbolic curve that reaches the resistive linear behavior asymptoticly, as shown in figure (1.8).

1.5.2 Energy analysis of the RCSJ model

The full equation (1.20) is strongly non linear and a complete solution can only be obtained numerically. However we can still gain some insight by using some energy arguments. In the following treatment the junction angular velocity $\omega = \dot{\phi}$ will be used instead of the voltage η. We can write the energy balance of the junction in the normalized description by multiplying (1.20) by ω and separating the parts that can be expressed as the time derivative of an energy from the ones that cannot:

$$\frac{d}{dt}\mathcal{E}_0 = \frac{d}{dt}\left\{\frac{\omega^2}{2} - \cos\phi - \alpha\phi\right\} = \beta_J\, \omega^2 \tag{1.24}$$

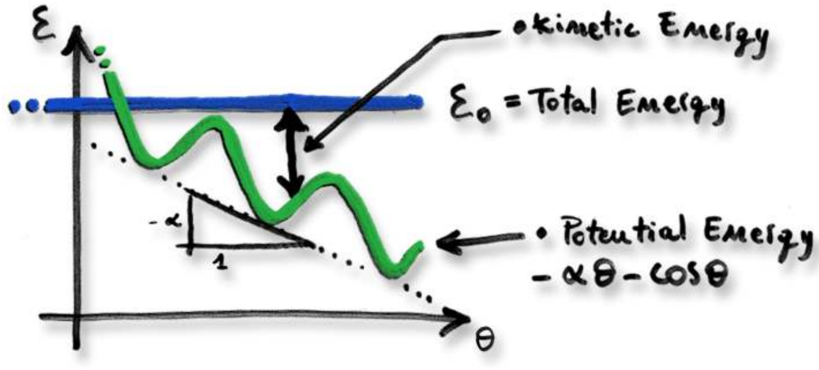

Figure 1.9: Graphical representation of the tilted washboard potential in the energy-conservative limit $\beta_J = 0$.

The total energy $\mathcal{E}_0$ is given by the sum of terms in the curly brackets, i.e.

- the charging energy term $\omega^2/2 \rightarrow \frac{V^2}{2C}$,
- the Josephson energy term $-\cos\phi \rightarrow -\frac{\hbar}{2e} I_c \cos\phi$,
- the energy generated by the current-bias generator $\alpha\phi \rightarrow IV$.

The term $\beta_J \omega^2$,on the right hand side of the equation, represents the power dissipated through the resistor V^2/R and cannot be included in the conservative term.
We have anticipated in section 1.4 that the behavior of the junction can be mapped one-to-one to the dynamics of a *phase particle* of unitary mass under the Josephson cosine potential. Because of the finite slope introduced by the applied bias current $\alpha \neq 0$, this picture is often indicated as *tilted washboard potential*[7].

When no bias-current is applied, the junction will describe damped oscillations until all the energy $\mathcal{E}_0$ is dissipated through the resistor. This transient will affect the dynamics for some RC time constants: the smaller the resistance R, the higher the power dissipated, the faster the equilibrium will be reached.
After such transient the phase particle will be in one of the local minima of washboard potential and the junction will be in the *superconducting state.*
The picture described up to now is true whenever the washboard potential has a local minimum, i.e. for currents smaller than the critical one.
When the bias current goes beyond such threshold, no more local minima

[7]for small values of α the skewing action of the bias current energy term resembles the tilting the Josephson potential energy

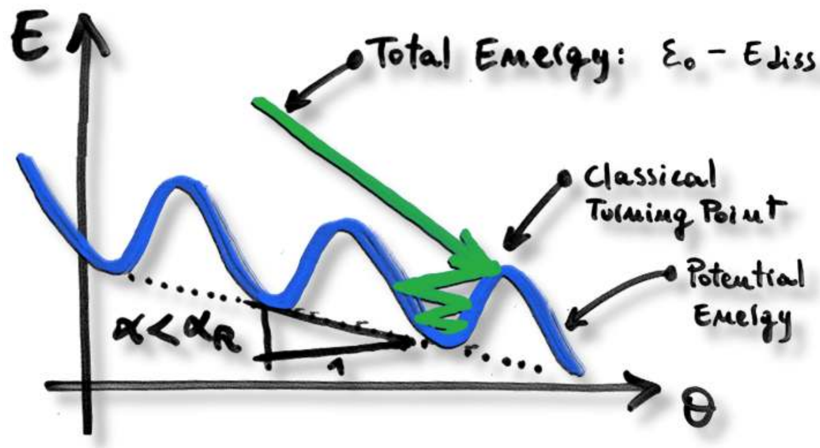

Figure 1.10: Tilted washboard potential with dissipation $\beta_J > 0$. The phase particle re-trapping can occur only for $I < I_R$.

exist and the phase particle slides down the wiggled profile of the potential — when this condition occurs, the junction is said to be in the *running* or *voltage state*. Applying very high bias currents $\alpha \gg 1$, the phase particle reaches a limit velocity, i.e. a voltage $V \approx I/R$, determined by the damping parameter β_J.

When the bias current is decreased back to values approaching the critical current, the phase particle will not be trapped into a local minimum of the potential. The reason for such phenomenon has its roots in the finite value of the kinetic energy of the phase particle, which should instead be zero for the trapping to occur. In other words, the resistor has to dissipate more energy than the bias-current generator can provide between two maxima of the washboard potential. If we represent, as in figure 1.10, the tilted washboard potential together with the total energy — whose value is not constant due to the dissipation mechanism — the retrapping will occur when the two curves intersect. The highest slope of the washboard potential at which the above mentioned intersection occurs is called retrapping current α_R and its value is given by:

$$\alpha_R = \frac{4}{\pi}\beta_J \qquad \text{, or in physical units} \qquad I_R = \frac{4Ic}{\pi R}\sqrt{\frac{\hbar I_c}{2eC}} \tag{1.25}$$

The equation (1.25) reflects the picture we have described so far. With smaller values of the resistance R it will be harder to trap the junction into a local minima by ramping down the bias current. Therefore, the value of the re-trapping current will be lower.

We incidentally notice that, using the values of both re-trapping current

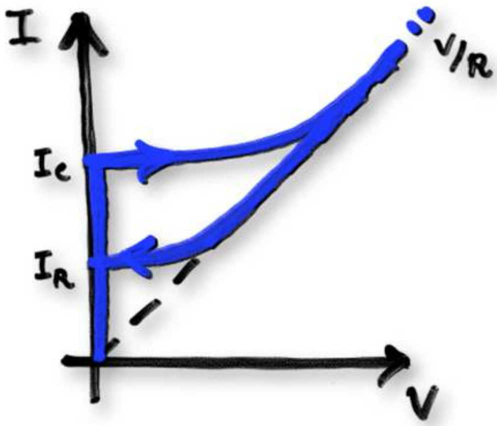

Figure 1.11: Hysteretic current-voltage characteristic predicted by the RCSJ model.

and critical current, we can estimate the capacitance of the junction without any need for time or frequency resolved measurements. An RCSJ current-voltage characteristic resembles the one shown in figure (1.11).

1.6 DC SQUID

The Josephson interferometer, also called *Direct-Coupled Superconducting Quantum Interference Device* or *DC SQUID*, is constituted by two Josephson junctions, connected in parallel by two superconducting leads as shown in figure 1.12.
In the following sections we will assume the SQUIDs to be constituted by infinitely small Josephson junctions. This is a good approximation only for magnetic fields that generate a flux through each junction whose value is much smaller than a flux quantum.

1.6.1 A constrain on the Junction phase differences

For the order parameter to have any physical meaning, i.e. being a single valued function, the line integral of the phase gradient in (1.3) has to be a multiple of 2π in every closed circuit. This has to be also true for a path like γ — shown in figure 1.12 — that passes through both the junctions and gets buried into the bulk of the superconducting leads that connect them. By integrating the fundamental relation (1.3) in such circuit and

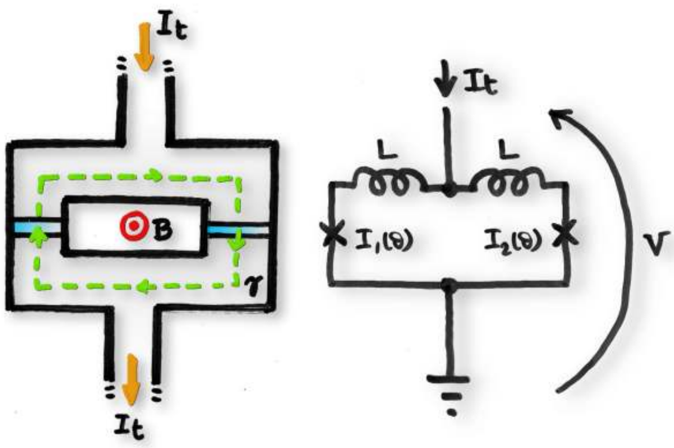

Figure 1.12: DC SQUID geometry (left) with its lumped elements model (right).

introducing the *gouge-invariant phase difference*[8] φ, we obtain a relation that acts locking the phase-drops on the two junctions:

$$\varphi_1 - \varphi_2 = 2\pi \frac{\Phi}{\Phi_0}$$

In other words, we can change the phase difference between the two junctions by applying an external magnetic field, i.e. imposing an external flux Φ. The total current I_t of the SQUID will be given by the sum of the currents of the single junctions:

$$I_t = I_1(\varphi_1) + I_2(\varphi_2) \tag{1.26}$$

There will be constructive interference when the currents have the same sign and destructive interference when the two junctions generate currents in opposite directions.

The critical current of the SQUID will be directly influenced by the interference of the junctions and its value will, in general, be found as a solution of the following maximization problem:

$$\begin{cases} I_c = max\{\ I_1(\varphi_1) + I_2(\varphi_2)\ \} \\ \\ \varphi_2 - \varphi_1 = 2\pi \frac{\Phi}{\Phi_0} \end{cases} \tag{1.27}$$

Different contributions can add up to the magnetic flux Φ. We mainly distinguish between

[8]The gouge invariant phase difference can be defined by a local relation $\nabla\varphi = \nabla\phi - \frac{2e}{\hbar}\mathbf{A}$

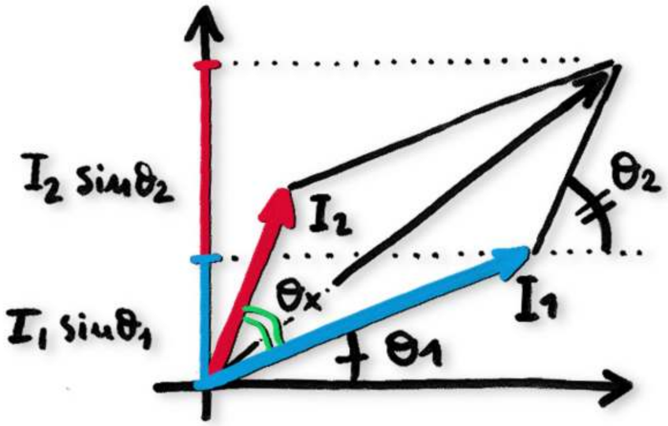

Figure 1.13: Graphic representation of the SQUID current by complex vector representation of the current-phase relations.

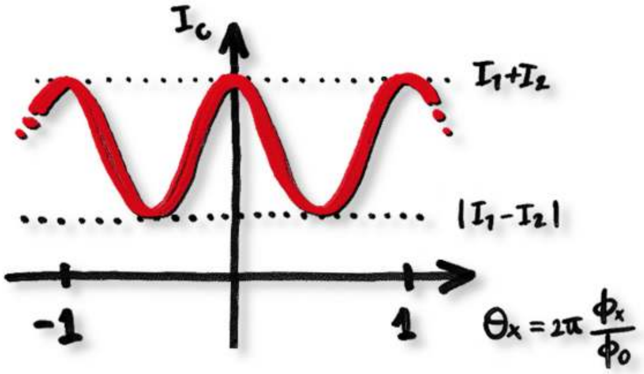

Figure 1.14: Critical current pattern of a SQUID in the negligible self-inductance limit.

- *external flux* contributions Φ_x, generated by external magnetic fields, and
- *self flux* contributions $L\, I_{loop}$, dependent on the current distribution of the SQUID.

1.6.2 Negligible self-inductance case

We consider first the case of an interferometer with negligible self-inductance L and sinusoidal current phase relation for both junctions[9] $I_i(\varphi_i) = I_i \sin\varphi_i$.

[9]to thin the notation we have used the same symbol for the current phase relation and the critical current; however, when referring to the current phase relation, we will

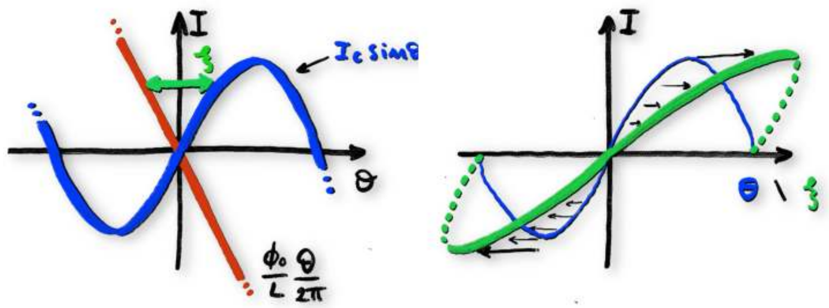

Figure 1.15: Graphical representation of the definition of $\xi(\phi)$ and its distortion effect on the current-phase relation.

Because of the sinusoidal dependence we can consider the two current-phase relations as vectors in a complex plane, with length proportional to the critical current and angle equal to the phase difference, as shown in figure 1.13. The total current will be given by the imaginary part of the vector addition of the currents $\mathbf{I_1}$ and $\mathbf{I_2}$. Therefore, the critical current can be identified in the modulus of such vector addition.

The $L = 0$ is a very special case since, for a fixed value of the external flux Φ, the two current vectors have constant relative orientation, i.e. the vector addition moves as a rigid body in the complex plane while changing the total current I_t.
Exploiting this observation we can write the SQUID critical current as:

$$I_c = \sqrt{(I_1 + I_2)^2 + 2\, I_1 I_2 \cos\left(2\pi \frac{\Phi}{\Phi_0}\right)} \tag{1.28}$$

I_c will be a periodic function of the magnetic flux Φ, with period Φ_0. The maximum critical current is obtained when Φ is a multiple of the flux quantum, so that the current of the two junctions add up in phase to $I_c = I_1 + I_2$. When instead Φ is equal to $\frac{\Phi_0}{2}(1 + 2n)$, with integer n, the two junctions are in phase opposition and their current flow in opposite direction, contributing to the critical current with $|I_1 - I_2|$.
The capability of resolving the small value of one flux quantum, makes a SQUID the most sensitive device to the magnetic field.

1.6.3 Finite self-inductance case

When the effect of the self-inductance of the SQUID loop is included in Φ, the problem becomes analytically intractable. The new flux contribution

explicitly write the phase dependence within brackets.

can be written as:

$$\Phi_{\text{self}} = L\, I_{\text{loop}} \qquad \text{,where} \qquad I_{\text{loop}} = \frac{1}{2}\left[I_1(\varphi_1) - I_2(\varphi_2)\right] \tag{1.29}$$

By applying an external flux, we change the configuration of currents that, generating a magnetic field and therefore a finite flux, changes itself the phase difference once more. If we come back to the representation of the currents as vectors in the complex plane, the angle between the vectors depends on the orientation of the vectors themselves. In principle, we should find a self consistent solution for the current distributions at every value of the magnetic flux.

A different approach has been used by T.A.Fulton [15, 16] by finding a transformation of the phases ϕ_i that permits to map the finite inductance problem into a negligible-inductance one, by employing a distorted current-phase relation. To do this, two self-inductances L_1 and L_2 are defined and put in series to the single junctions, so that the sum of them is equal to the self-inductance of the SQUID loop:

$$L = L_1 + L_2 \qquad \Rightarrow \qquad \Phi_{self} = \frac{1}{2}\left(L_1\, I_1(\varphi_1) - L_2\, I_2(\varphi_2)\right) \tag{1.30}$$

When this is done a *self-field including phase difference* ξ_i can be found. Its value is completely determined by φ_i through the inductance and the undistorted current phase relation, with:

$$\xi_i(\varphi_i) = \varphi_i + \frac{\pi}{\Phi_0} L_i\, I_i(\varphi_i) \tag{1.31}$$

Using ξ_i instead of the φ_i, the phase constraint (1.6.1) can be expressed as in the negligible inductance limit. The effect of the transformation $\phi_i \rightarrow \xi_i$ in the current phase relation I_i is to skew it with an angle proportional to L_i. Moreover, if the inductance exceeds a threshold value given by:

$$L_i^{th} = \frac{\Phi_0}{2\pi} \left.\frac{dI_i}{d\varphi_i}\right|_{max} \tag{1.32}$$

the distorted version of the current phase relation will be a multivalued function.

When both L_1 and L_2 are lower than their threshold value L^{th} and the current phase relations are continuous "well-behaved" functions, the critical current pattern will be itself a continuous "well-behaved" function and its maximum and minimum value will be still given by $|I_1 \pm I_2|$. In qualitative terms, the inductance will affect the critical current pattern by making it look more triangle like, as in figure 1.16.

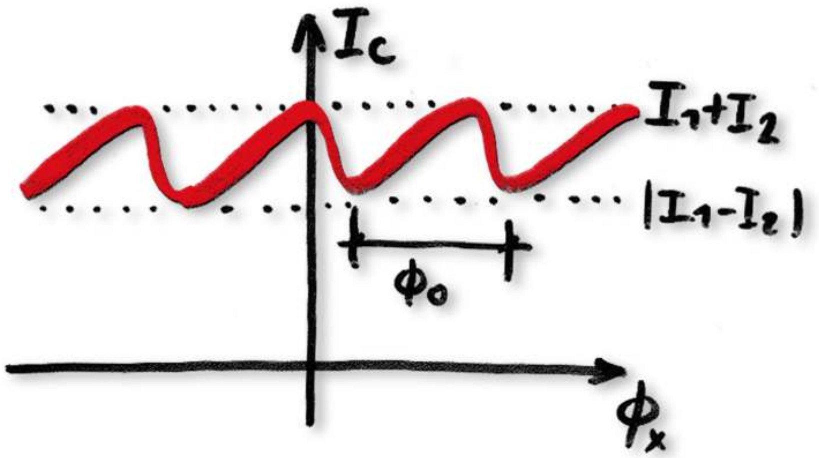

Figure 1.16: Critical current interference pattern for a finite self-inductance case below the inductance threshold L_{th}.

On the other hand, when L_i goes above its threshold, the critical current pattern resemble a saw-tooth function, still with periodicity Φ_0 and maximum value $I_1 + I_2$. Nevertheless, the value of the difference cannot be determined from the graph and curve fittings might be necessary to extrapolate more information.

1.7 High-T_C junctions

We have previously mentioned that YBCO is characterized by a very small coherence length. This has been a serious problem for the fabrication of junctions in early experiments with high-T_C superconductors because of the vanishing coupling between the superconducting leads necessary for the Josephson effect to take place. However different technologies, like bicrystal or biepitaxial technology, have made possible to realize good quality Josephson junction by exploiting some accurately engineered artificial grain boundaries. A brief discussion about such junction will be given in chapter 2.

It's worth to point out one more peculiarity of the high-T_C junctions. We have seen how the Josephson critical current J_c depends, in the BCS s-wave case, on the product of the amplitude of the order parameter in the two superconducting electrodes. Therefore, we should reasonably expect the anisotropy of the order parameter to have a big influence on the Josephson critical current, depending on the relative orientation of the crystal lattice in the two leads. Sigrist and Rice [17] were the first to point out such dependence, suggesting the following expression for the critical current:

$$J_C = J_0 \, (\Delta_L \cdot \mathbf{n})(\Delta_R \cdot \mathbf{n}) \tag{1.33}$$

In 2002 Lombardi and coworkers [18] have published measurements of the critical current of biepitaxial YBCO junctions, strongly supporting the d-wave order symmetry and the Sigrist-Rice formula. Later on, in 2005, Hilgenkamp and coworkers [3] have published data of the same kind, giving a striking evidence of the different behavior of the critical current in ramp edge junctions in twinned and untwinned YBCO ramp-edge junctions. In particular, the existence of vanishing critical current at 43° from the direction of the maximum in untwinned YBCO crystals has provided a strong indication of the existence of a small s-wave component superimposed on the d-wave part.

1.8 Single Electron Transistor

The label transistor is used to identify a general three terminal device constituted by a current channel that can be modulated by means of an applied signal to a gate electrode. In a *Single Electron Transistor* the conductive channel is constituted by the series of two tunnel junctions insisting on a common electrode called *island*. The current modulation occurs because of inhibition of single electron tunneling events into and out of the island when no voltage is applied to the gate electrode. This phenomenon, called *Coulomb blockade of tunneling*, can be suppressed whenever we induce in the island a charge higher than a certain threshold.

For the conductivity modulation to occur, the charging energy E_c of each junction, given by

$$E_c = \frac{e^2}{2C} \quad , \tag{1.34}$$

has to be higher than the thermal fluctuations energy $k_B T$. To satisfy this constrain and fabricate a device that could operate at temperatures around 1 K, the junction capacitances have to be smaller than 1 fF.

Moreover the conductivity of the junction has to be small enough so that quantum fluctuations will not wash away the blockade. This is because, in an SET, the time uncertainty for any energy measurement is limited by an RC time constant, where C is the capacitance of the junction while R is the quasi-particle conductance. As a result, the energy-time uncertainty principle acts as a constrain for our devices, imposing:

$$\Delta E \cdot \Delta t = \frac{e^2}{2C} \cdot RC > \hbar \quad \Rightarrow \quad R > \frac{2\hbar}{e^2} \approx 25 \text{ k}\Omega \tag{1.35}$$

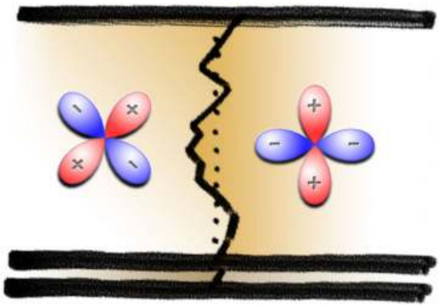

Figure 1.17: Sketchy representation of a grain-boundary Josephson junction. Ideal and real — meandered — grain boundary are both represented.

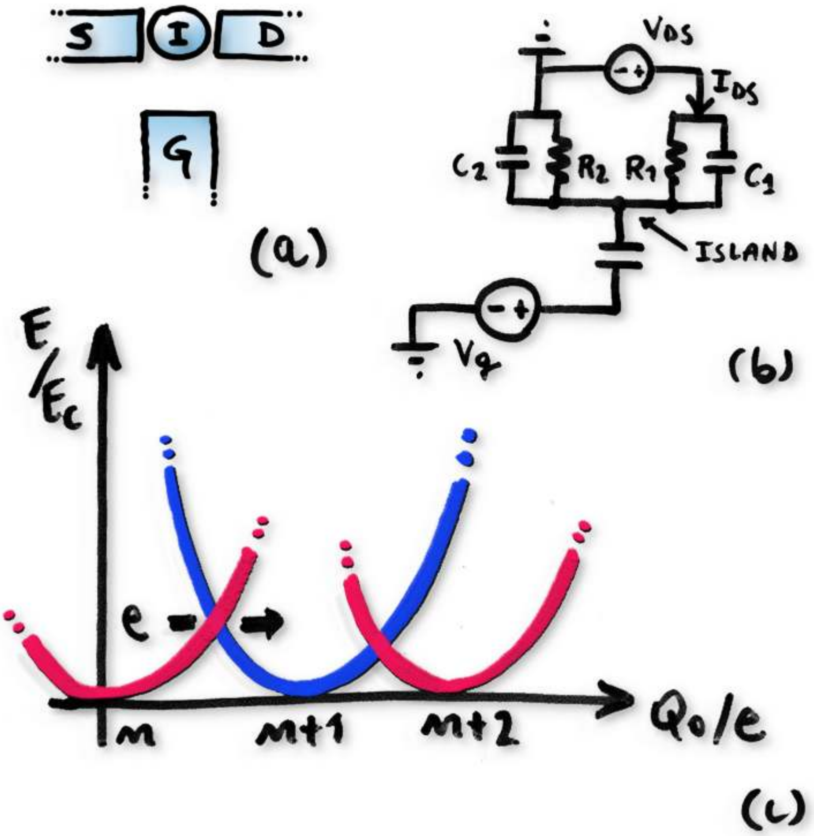

Figure 1.18: Sketch of the structure of a normal-metal SET (a) with its lumped elements model (b) and energy diagram (c). S, D and G stand respectively for Source, Drain and Gate.

The behavior of a SET changes substantially whether normal conductor or superconducting island and leads are used. After the discussion of the behavior of an all normal-conducting SET, we will generalize the picture to a superconducting SET and explain how a such device can give direct information of the order parameter symmetry in a d-wave Coulomb blockade electrometer.

1.8.1 A normal-metal SET

We will consider first a normal metal SET where no voltage is applied between source and drain. If we discard constant energy terms [7], the energy of an SET can be expressed as:

$$E = \frac{(C_g V_g + ne)^2}{C_1 + C_2 + C_g} \tag{1.36}$$

where we have indicate with C_i the capacitances of the junctions, with ne the charge present in the island and with $C_g V_g$ the charge induced in the island by a voltage V_g applied to the gate electrode.

Because of the integer number of electrons n that can be contained in the island, the SET energy is characterized by a set of parabolas, centered at voltages multiple of e/Cg. The device will try constantly to minimize its energy by sitting on the bottom of one of the parabolas: we will identify this state with $\hat{n}$.
When sweeping the gate voltage, the energy of the SET follows the parabola at $\hat{n}$ up to a degeneracy point, where the parabola at $\hat{n}+1$ is crossed. For higher voltages higher than the crossing point $\frac{e}{C_g}(\hat{n}+1/2)$, it is energetically favorable to abandon $\hat{n}$ and switch to the next parabola and ,when this occurs, a single electron can tunnel into the island.
The remarkable fact is that, since no energy barrier hinder this process, at the degeneracy point a current can be generated with any vanishingly small voltage. We will obtain a steady current in the bias circuit whenever the gate capacitor induces in the island a charge multiple of e.

For other values of the gate voltage a current can still be created by a series of single electron tunneling processes. Nevertheless the processes will have to overcome an energy barrier ΔE_j that depends both on the voltage drop across the tunneling junction we want to tunnel through, and on the charge induced on the island by the gate electrode.

Indicating with $\pm$ the transition in the tunneling processes $n \to n \pm 1$ occurring in the junction j, we can express the energy barrier ΔE_j as:

$$\Delta E_j^{\pm} = \frac{e^2}{C_\Sigma} \left\{ \left[\frac{1}{2} \pm \left(n - \frac{C_G V_G}{e} \right) \right] \pm \frac{C_j V_{DS}}{e} \right\} \tag{1.37}$$

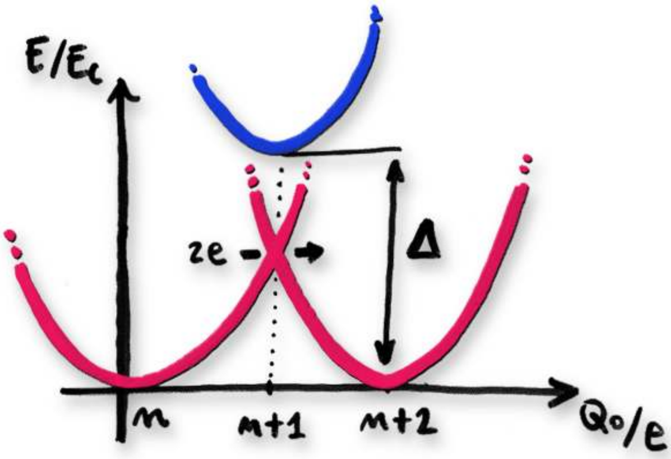

Figure 1.19: Single electron tunneling in a BCS-superconductor SET.

The rate Γ_j at which such tunneling process occur across the junction j strongly depend on the energy barrier ΔE_j of the junction:

$$\Gamma_j = \frac{1}{e^2 R_j}\left(\frac{\Delta E_j}{exp\{\Delta E_j/k_B T\} - 1}\right) \tag{1.38}$$

For negative values of ΔE_j it is possible to obtain finite tunneling rates and a finite current I_{DS}, passing through the transistor, can be generated as a sequence of the tunneling processes into the island Γ_1 and out from it Γ_2.

What is really important for our experiment is the periodicity of the SET current, for small V_{DS} voltages, while sweeping the gate voltage V_G. Depending whether we have a *normal-metal* or *superconducting SET*, the periodicity will be a multiple of a single electron or a Cooper-pair charge times C_g.

1.8.2 A BCS-Superconductor SET

Let's consider a superconducting SET being in one of the parabolas defined by (1.36) with an even number of electrons n_{even} in the island. At temperatures lower than T_C, all electrons can pair up and the whole charge in the island will consist exclusively of Cooper-pairs. Again, by sweeping the gate voltage, we can trace up the parabolic branch to the next parabola whose minimum is at $n_{even} + 1$. At this point we expect a tunneling to occur but, due to lack of availability of a "partner" quasi-particle excitation, pairing into Cooper pair cannot take place.

For this reason, the minimum of the set of parabolas with odd island charge has to be lifted by an amount equal to the energy gap Δ. In particular, if the charging energy e^2/C_Σ is small, it can happen that the even-charge parabolas cross each other at a degeneracy point at an energy lower than Δ. In this case Cooper-pair can tunnel and the periodicity of the current at low V_{DS} will be doubled. Experiments on BCS type SET have shown the evidence of such period doubling with decreasing temperatures or at magnetic fields high enough to make the metal normal-conducting.

1.8.3 The high-T_C challenge

The realization of an all high-T_C SET would make possible to investigate the presence of a possible imaginary *s*-wave part overlapped to the dominant *d*-wave order parameter. To reveal such component, we would exploit the periodicity doubling of the SET current, measured at low bias voltage.

Quite recently [19] quantum behavior of the phase has been observed in YBCO junctions at temperatures close to 20 mK, despite the belief that the quasi-particle excitations present in nodal directions of the *d*-wave could cause the loss of phase coherence within the Josephson junction. The direct detection of a fully developed *s*-wave gap in the quasi-particle excitation spectrum could support such observation, encouraging the efforts for the realization of a purely *d*-wave phase qubit and the application of high-T_C superconductors in the field of quantum computing.

As we have mentioned beforehand in this chapter, very fundamental physics considerations limit the operation of a Coulomb blockade electrometer to temperatures lower than $\frac{e^2}{2K_B C_\Sigma}$ for SET with junction resistance higher of the *Von Klitzing resistance*. The high resistance constraint, very difficult to achieve in traditional high-T_C junctions, can be satisfied in submicrometer sized grain boundary junctions with high mis-orientation angle of the neighbor crystals [10]. We will introduce these junctions in chapter 2. Moreover very small capacitances — preferably less than 1 fF — are then needed for an SET to be operative.

These junctions are very difficult to realize since local loss of superconductivity of the film can occur because of oxygen out diffusion. Moreover coupling between the substrate and the superconducting film plays a big role in determining the junction capacitance [20][21] and a careful selection of the substrate material has to be done. In particular, traditional perovskite substrates, such as strontium titanate, seem to work badly due to the paramount value of the dielectric constant which ranges from 100 at

[10] This is due to the fact that whenever tunneling in the c-axis direction comes into play, the overlap of the order parameter in the two sides of the junction decreases considerably, enhancing the junction resistance.

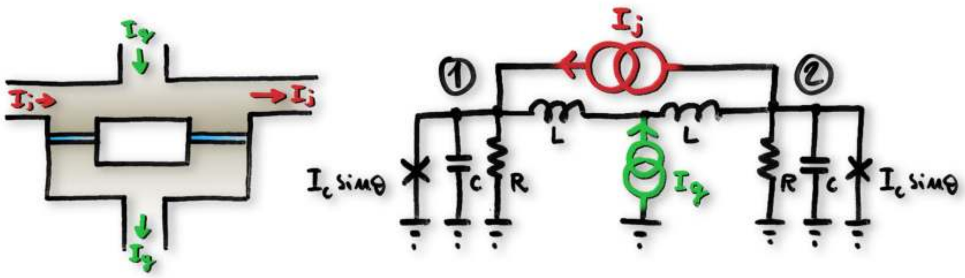

Figure 1.20: SQUID with injection lines (left) and lumped elements model of the system (right).

200 K to values higher than 1000 at 4 K and below. This contribution to the junction capacitance imposes an even more stringent requirement on the junction size, which becomes too small to be realized.
Moreover, even if such a SET could be build, its characteristics should be measured by very sensitive RF techniques[22], that would be strongly disturbed by the high dielectric losses of traditional perovskite materials.

In this thesis we have investigated the possibility to fabricate an all high-T_C single electron transistor with YBCO grain boundary Josephson junctions. For the substrate material we have selected YSZ bicrystals because of the low value of dielectric constant at both room and cryogenic temperature, because of the low dielectric losses at radio frequency and, finally, because of the good quality of the artificial grain boundaries obtainable in these materials.
To make an estimation of the capacitance of these junctions, we have studied the current-voltage characteristics of Josephson interferometers fabricated on the same chip.

1.9 SQUID resonances

In previous section we have explained the importance of fabricating grain boundary junctions with small capacitance. Measuring of so small capacitances are generally quite complicated. Estimations based on (1.25) and on the measurement of the hysteresis of the the junction is not always accurate. The junction can in fact switch to the running state at currents lower than the critical one, because of thermal fluctuations, impairing the accuracy of the capacitance estimation. Moreover we might be interested on the behavior of the capacitance at high frequencies rather than its DC value.

An accurate method of measuring the junction capacitance involves the measurement of the resonant frequency of the LC resonator composed by a SQUID loop self inductance and by the junction capacitances. The interaction of the Josephson AC currents with the LC resonator causes a series of current steps to appear in the DC current-voltage characteristic of the SQUID. In the following paragraph we will explain how the measurement of a current voltage characteristic can be used to estimate with high accuracy the capacitance of the junctions of a SQUID.

To model our SQUIDS we can use a lumped-elements model shown in figure 1.20. RCSJ models are used to describe the two junctions while lumped inductances model the SQUID self-inductance. The gate-current I_g enables us to measure the current-voltage characteristic of the SQUID. The *control current* I_j is responsible for generating the phase difference between the two junctions. The following treatment will assume perfect symmetry for both branches of the interferometer. However, the main results can be generalized also for asymmetrical critical currents, a case which is very frequent in high-T_C devices due to the lack of precise control over the meandering of the grain boundary.

Following D.B. Tuckerman and J.H. Magerlein [23], we can express the Kirchoff equations for the two nodes 1 and 2 of the circuit in Figure 1.20, and express all quantities in terms of the nodal phases φ_1 and φ_2. By expressing the equations by a new set of variables φ_s and φ_d, obtained through the following linear combination of the nodal phases,

$$\varphi_s = \frac{1}{2}[\varphi_1 + \varphi_2] \quad , \quad \varphi_d = \frac{1}{2}[\varphi_1 - \varphi_2] \tag{1.39}$$

its possible to separate the effect of the two current generators and to isolate the inductance contribution in only one of the equations, i.e. the one in φ_d:

$$\begin{cases} C\ddot{\varphi}_s + \frac{1}{R}\dot{\varphi}_s + I_c\frac{2e}{\hbar}\cos\varphi_d \, \sin\varphi_s = \frac{2e}{\hbar}\frac{I_g}{2} \\ C\ddot{\varphi}_d + \frac{1}{R}\dot{\varphi}_d + \frac{2}{L}\varphi_d + I_c\frac{2e}{\hbar}\cos\varphi_s \, \sin\varphi_d = \frac{2e}{\hbar}I_j \end{cases} \tag{1.40}$$

The equation in φ_s resembles very much the classic RCSJ model and therefore cannot be attributed to model the steps in current we are interested in. Because of the energy limit imposed by the LC resonator, it is reasonable to assume that φ_d cannot go into any running state and, therefore, will describe some kind of harmonic oscillation. When the φ_s hits the φ_d oscillation frequency, the product of harmonic functions in φ_s and φ_d give a DC contribution and, consequently, a current step. However, when the oscillation frequency match the LC resonator one, the peak in current will be maximized.

The considerations above are synthesized in the following *ansatz*:

$$\varphi_s = m\,\omega t + \alpha + \frac{\pi}{2}m \quad , \quad \varphi_d = \delta \sin \omega t + \beta + \frac{\pi}{2}m \tag{1.41}$$

By solving the system (1.40) with the ansatz above and separating the DC component from the $\sin \omega t$ and $\cos \omega t$ AC components, it is possible to obtain a set of self consistent equations for the ansatz parameters.

The model predicts that, at a voltage $\frac{\hbar}{2e}\frac{2m\omega}{R}$, some portion of the the gate current I_g will be drained through the Josephson junction, while the remaining part will go through the resistor. Such Josephson DC contribution, called *excess current* I_x,

$$I_x = \frac{\hbar}{2e}\frac{\omega\delta^2}{2mR}$$

depends on the average power of the phase oscillation $\frac{\delta^2}{2}$ — result obtained by Zappe and Landmann in [24] — whose values have to satisfy the self-consistent relations:

$$\begin{cases} I_j = \frac{\hbar}{2e}\frac{\beta}{L} + I_c J_m \sin\alpha \; \cos\beta \\ \frac{\hbar}{2e}\frac{\delta}{L}\left(\omega^2 CL - 1\right) = I_c\left[J_{m+1}(\delta) - J_{m-1}(\delta)\right]\sin\alpha \; \sin\beta \\ \frac{\hbar}{2e}\frac{\omega\delta}{R} = I_c\left[J_{m+1}(\delta) + J_{m-1}(\delta)\right]\cos\alpha \; \sin\beta \end{cases} \tag{1.42}$$

When the voltage is fixed at multiples of the LC resonant voltage, the equations are satisfied for $\alpha = 0$ and the excess current I_x has a maximum for $I_j = \frac{\Phi_0}{4L}$ when m is odd and at $I_j = 0$ when m is even. In other words, current steps occur at even and odd multiples of resonant voltage $\frac{\hbar\omega_{LC}}{2e}$. The even resonances follow the behavior of the critical current interference pattern while the odd resonances give have a maximum current when the critical current pattern has its minimum.

This feature is a fingerprint of this resonator-SQUID interaction and can be used to estimate the frequency of the LC resonant frequency. Since we can measure roughly half of the inductance of the SQUID loop from the periodicity of the critical current pattern, we can infer the inductance L of the SQUID and, therefore, estimate the junction capacitance C with high accuracy at high frequencies through a DC measurement.

1.10 External LC resonance

In the previous section we have seen that the interaction of the a couple of Josephson junctions with the LC resonator, formed by the tunnel-junction

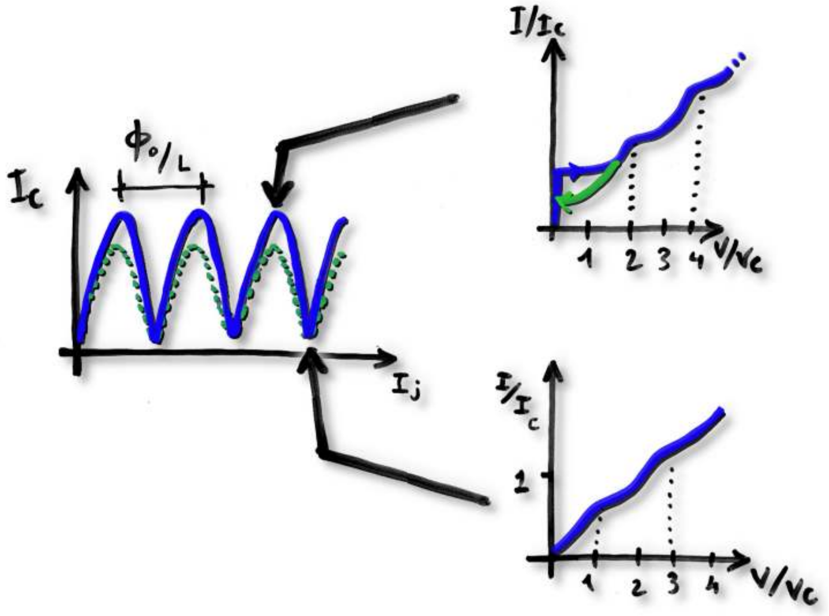

Figure 1.21: Representation of the results predicted by Tuckermann and Magerlin in [23].

capacitances and by the superconducting SQUID ring, can give rise to steps in the critical current when the phase difference φ_d hits the frequency of the the LC resonator. However, this is not the only phenomenon that can generate steps in the current-voltage characteristic. Excess current steps can also occur when a single junction is connected to the current generator through a series LC resonator, as shown in Figure 1.22 . To simplify the circuit and capture the essence of such interaction, we will consider a simple RSJ model to describe the junction behavior.

The circuit dynamics can be described by a set of three differential equa-

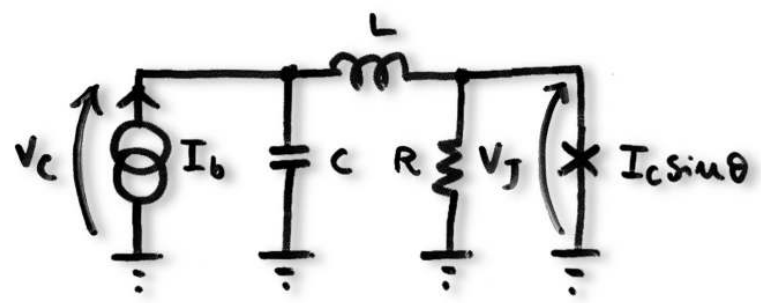

Figure 1.22: Lumped elements model of a stray capacitive coupling which can give rise to steps in the IV curve.

tions composed by

- the second Josephson relation (1.13),
- the Kirchoff Current law at the ground node, and
- the Kirchoff voltage law evaluated around the mesh.

Indicating with V_J the voltage across the junction, with φ the junction phase difference and with V_C the voltage across the capacitor, we can write the set of equations as:

$$\begin{cases} \frac{d\varphi}{dt} = \frac{2e}{\hbar} V_J \\ \frac{dV_C}{dt} = \frac{1}{C}\left[I_g - I_c \sin\varphi - \frac{1}{R} V_J\right] \\ \frac{dV_J}{dt} = \frac{R}{L}\left[V_J - V_C - I_c L \cos\varphi \ \frac{2e}{\hbar} V_J\right] \end{cases} \tag{1.43}$$

where I_c, R, L and C are respectively the junction critical current, the lumped resistance of the junction and the inductor and capacitor describing the resonator.

As in the dynamic system (1.40), the third equation contains the product between the Josephson current and the voltage V_J. Such term can give rise to a frequency mixing effect and, eventually, can be responsible for the generation of a DC current step.

For values of the bias current I_b higher than the junction critical current, a finite voltage $V_J = \frac{\hbar}{2e}\omega$ will develop across the junction and, consequently, the ideal Josephson junction will contribute with a current composed by a comb of harmonics at frequencies multiple of ω.
Noticing that the series LC resonator behaves as a short circuit for voltages close to its resonance, we would not be surprised if some interaction occurs in the neighborhood of $\omega_{LC} = (LC)^{-\frac{1}{2}}$. To obtain an approximate solution for the current-voltage characteristic in such region, we can think about using an approach similar to the one of Tuckerman and Magerlein in [23]. Setting the following *ansatz* for the phase time dependence:

$$\varphi = \varphi_0 + \omega t + \nu \sin(\omega t + \varsigma) \tag{1.44}$$

and using it to solve the circuit, we obtain a self-consistent equation which can be solved for the DC and AC components at the frequency ω:

$$\begin{cases} I_x = I_g - \frac{\hbar\omega}{2eR} = -I_c J_1(\nu)\sin(\varphi_0 - \varsigma) \\ \frac{\hbar\omega}{2eR}\nu + I_c\left[J_0(\nu) + J_2(\nu)\right]\sin(\varphi_0 - \varsigma) = 0 \\ \frac{\hbar\omega^2 C}{2e}\nu = I_c(1 - LC\omega^2)\left[J_0(\nu) - J_2(\nu)\right]\cos(\varphi_0 - \varsigma) \end{cases} \tag{1.45}$$

Such set of equations is very similar to the one of Tuckerman and Magerlein, shown in the previous section.

From the first equation we obtain the excess current I_x, whose amplitude describes the current peak we are interested in. By using a Bessel function equality, used also in the previous section, we can express I_x as a function of the the power of the phase harmonic term $\frac{\nu^2}{2}$, very general result obtained by Zappe and Landmann [24].
The second and third equations can be rewritten as:

$$\left[\frac{2eI_c}{\hbar\omega}\right]^2 = \left[\frac{1}{R}\,\frac{\nu}{J_0(\nu)+J_2(\nu)}\right]^2 + \left[\frac{\omega C}{1-LC\omega^2}\,\frac{\nu}{J_0(\nu)-J_2(\nu)}\right]^2 \tag{1.46}$$

$$\tan(\varphi_0-\varsigma) = -\left[\frac{J_0(\nu)-J_2(\nu)}{J_0(\nu)+J_2(\nu)}\right]\frac{1-LC\omega^2}{\omega RC} \tag{1.47}$$

Equation (1.46) can be solved approximately by noticing that the second term on the right hand side diverges when ω gets close to resonance. By using the asymptotic approximation:

$$\omega = \omega_{LC} + \delta\omega \qquad \rightarrow \qquad \omega^2 \approx \frac{1}{LC}\left[1 + 2\frac{\delta\omega}{\omega_{LC}}\right]$$

and approximating the Bessel functions with their values in zero, we obtain an expression for the phase oscillation:

$$\nu \approx \frac{4eLI_c}{\hbar}\,\frac{\delta\omega}{\omega_{LC}} \tag{1.48}$$

and for the tangent of the difference between the phase references φ_0 and ς:

$$\tan(\varphi_0-\varsigma) \approx 2\frac{\sqrt{LC}}{RC}\,\frac{\delta\omega}{\omega_{LC}} \tag{1.49}$$

Equation (1.49) has a direct interpretation, since the LC resonator contributes to shift the phase difference $\varphi_0-\varsigma$ by π when crossing the resonance. This phenomenon is general to any resonator and, in our system, manifests itself by switching the sign of the DC current contribution when passing through the voltage V_{LC}.

It is worth to point out that:

- the voltage width of the current-peak depends inversely on the quality factor of the resonator $\frac{RC}{\sqrt{LC}}$;

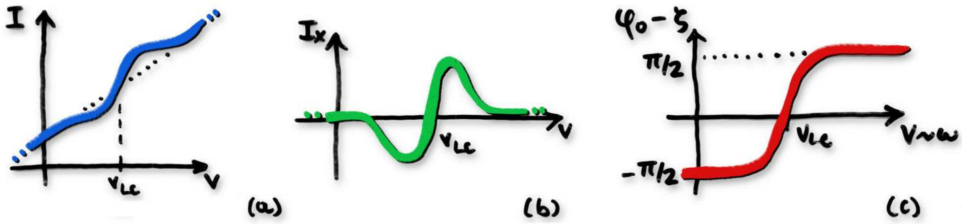

Figure 1.23: Close-up of a current step of a generated by the interaction between a Josephson junction with a series LC resonator (a). Excess current contribution (b) and phase reference difference $\varphi_0 - \varsigma$ when crossing the resonance voltage — the resonator contributes with a phase shift of π.

- the amplitude of the a.c. voltage term, and therefore the step height, is proportional to the critical current of the junction. Therefore, a suppression of the critical current by an applied magnetic field will cause the suppression of the excess current I_x, i.e. the current steps caused by the interaction between the single junctions and the LC resonator will have the same variation with magnetic field of the critical current pattern of the junction.

The analysis of the magnetic field dependence of the excess current steps can be used to assess whether its generating process is the internal SQUID-LC resonance or the stray capacitance effect discussed now. The SQUID resonances of odd order are in fact maximized when every other excess-current generating process is minimized.

Chapter 2

Device fabrication

2.1 Grain boundary Josephson junctions

After the discovery of the first high-T_C superconductors, it was soon realized the difficultly in realizing applications based on these materials[25]. The very short coherence length of the order parameter, of the order of one nanometer, seemed to preclude the realization of high-quality Josephson junctions. To unveil the basic properties of cuprate superconductor interfaces the bicrystal technology was invented. Such technology permitted to engineer well defined grain boundaries which, under certain conditions, proved to have Josephson properties.

2.1.1 Bicrystal technology

As the name suggests, the bicrystal technology is based on "gluing" together two single crystals to form a single sample. The two crystals are carefully cut along the desired directions, brought in contact along the freshly cut surfaces and annealed below the melting point under an high applied pressure in ultra-high vacuum conditions. As an example we show in Figure 2.1 a TEM micrograph where the grain boundary between the two YSZ crystals is clearly visible. In high-T_C applications, such sample is further diced, polished along a desired direction and used as substrate to epitaxially grow an high-T_C superconductor thin film.
The surface orientation of the substrate acts as a "template" for the orientation of the deposited superconducting film. Because of the different orientations of the crystal in the two halves of the substrate, the artificial grain boundary present in the substrate is reproduced into the film. The bicrystal technology has historically been the first technique to study grain boundary properties of cuprate superconductors, permitting to discover that

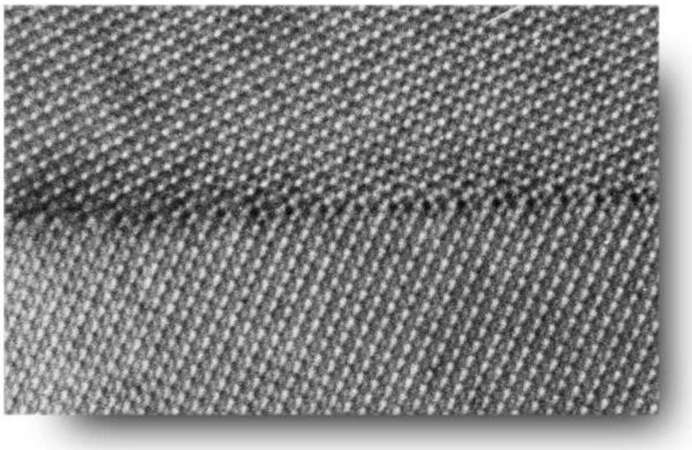

Figure 2.1: HRTEM micrograph of a YSZ bicrystal. Courtesy of Evgeny Stepantsov.

large-angle boundaries form excellent Josephson junctions.
Grain boundaries are usually classified according to the displacement and the rotation of the abutting crystals, as shown schematically in Figure 2.2. In particular it is customary to distinguish between the tilt and twist components of the misorientation. Tilt refers to a rotation around an axis lying within the plane of the grain boundary. Twist refers instead to a rotation of the crystal grains around the normal to the grain boundary plane. In Figure 2.2 examples of [001]-tilt, [100]-tilt boundary and [100]-twist boundary junctions are shown.

In this work YBCO films deposited on YSZ bicrystals have been used to realize superconducting devices. Such YBCO bicrystal, sketched in Figure 2.2(d), is characterized by 12° [100]-tilt in both abutting crystals while the [001]-tilt rotation has been selected to be 0° and 45° in the two halves. A 150 nm YBCO thin film has been deposited by pulsed laser deposition, i.e. by ablating a YBCO sintered powder target using an externally modulated KrF excimer laser. The sample is further covered with a 25 Å thick layer of gold, deposited by magnetron sputtering. The gold layer helps to preserve the YBCO superconducting properties, obstructing the oxygen out diffusion. The parameters used for the YBCO film deposition are similar to the ones shown in Appendix, in Table C.1.

2.1.2 Biepitaxial deposition

A strong limitation of the bicrystal technology for electronics application comes from the fact that all devices have to be aligned along the artificial

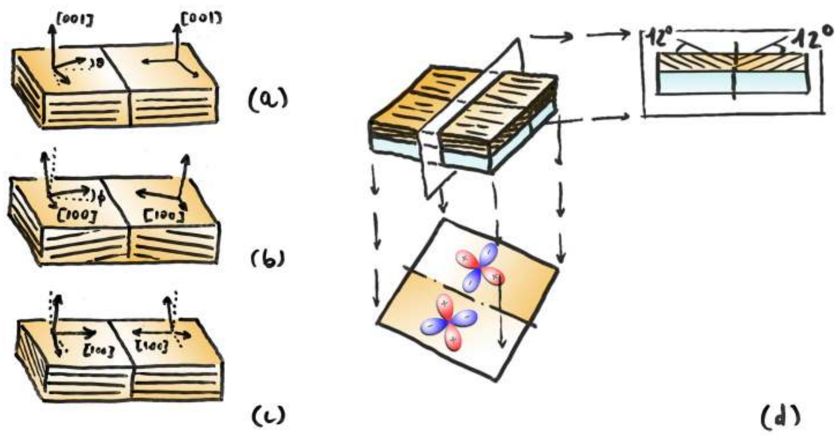

Figure 2.2: Schematic diagram showing the crystallography of (a) a [001]-tilt boundary, (b) a [100]-tilt boundary, and (c) a [100]-twist boundary. A representation of the YSZ bicrystal used in this work is shown in (d) by representing the order parameter orientation.

grain boundary line. However, such limitation can be overcome by employing the biepitaxial technology.

In the biepitaxial technology single crystal substrates are used and a thin film of a suitable material, called *seeding layer*, is epitaxially grown on top of its surface. The seeding layer is further patterned by argon ion milling, with an amorphous carbon (a-C) mask on top. After removing the carbon mask , such sample is used as a substrate for the epitaxial deposition of a high-T_C superconductor thin film. The film will have different crystal orientations depending on whether the deposition occurs in the seeding layer region or on the bare substrate. In this way an artificial grain boundary is located at a position corresponding to the edge of the seeding layer. A cross-section of a biepitaxial junction like the one used in this work is shown in Figure 2.4.

To fabricate a biepitaxial sample, an series of fabrication steps has to be done. We will further refer to Figure 2.3 when mentioning each step number:

- **STO seeding layer deposition (1-2)**: a thin strontium titanate film is grown uniformly by ablating a sintered powder target using an externally modulated KrF excimer laser.

- **Amorphous carbon mask preparation (3-8)**: We will give a more detailed description of such steps when talking about the device fabrication and YBCO patterning, in section 2.4.4.

- **Seeding layer patterning (9)**: the STO layer is milled with a Kauffman broad argon ion beam source, with a procedure similar to the one

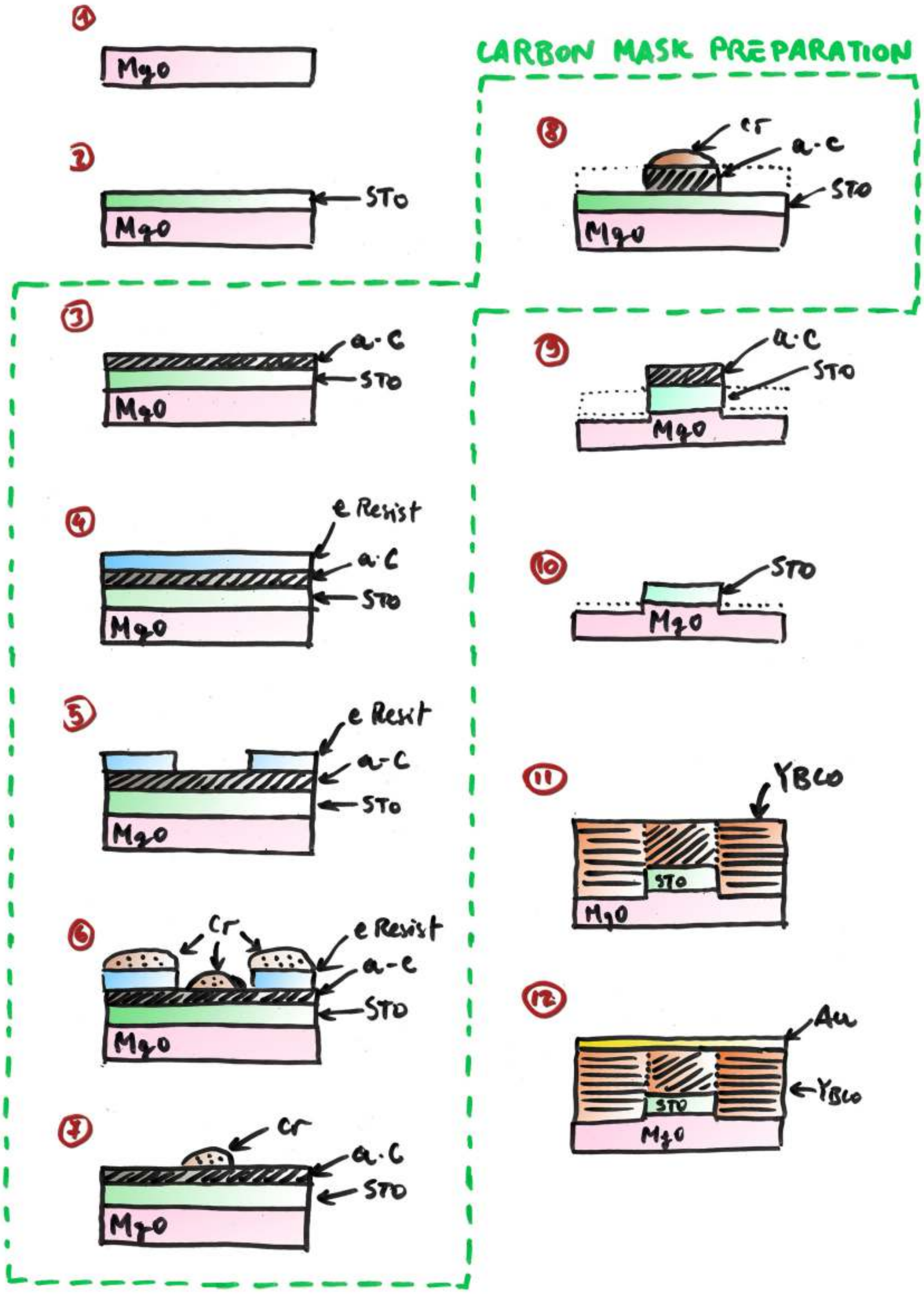

Figure 2.3: Steps of fabrication nedded to realize a biepitaxial sample.

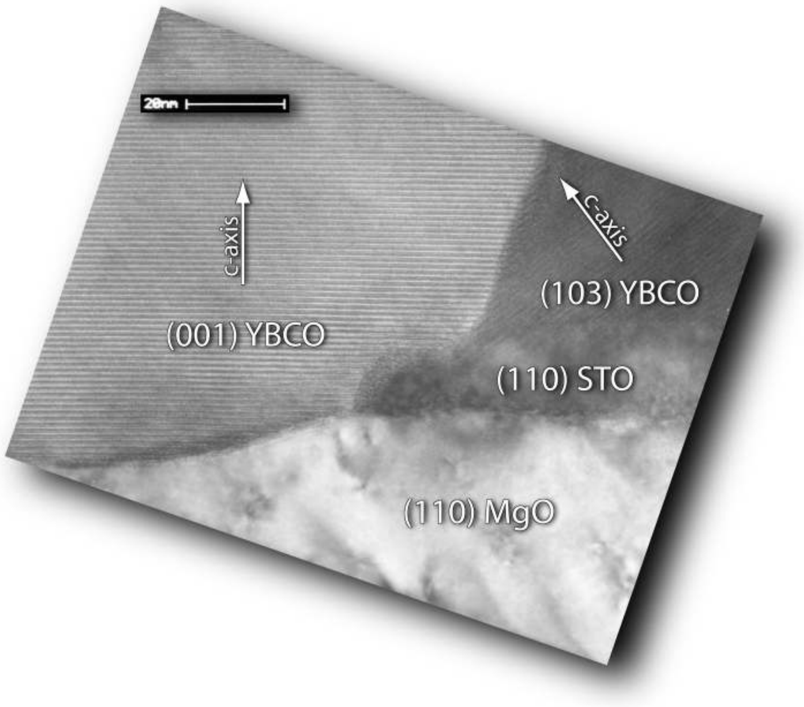

Figure 2.4: HRTEM micrograph of a biepitaxial YBCO junction with STO seeding layer on a MgO substrate. We are extremely grateful to Henrik Pettersson and the Microscopy and Microanalysis group at the Applied Physics Laboratory, Chalmers University of Technology, for providing us with the image.

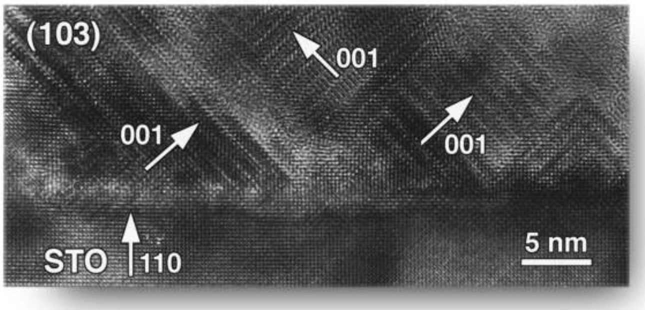

Figure 2.5: HRTEM of a biepitaxial YBCO film fabricated on a STO pure [110] substrate [26]. The presence of intrinsic 90° tilt grain boundaries between the (103) and ($\bar{1}03$) domains is evident.

used to pattern the devices in the YBCO film.

- **Sample plasma cleaning (10)**: a 30 min oxygen plasma cleaning procedure has been used to remove the carbon mask without affecting the other materials.

- **YBCO pulsed laser deposition (11)**:the film has been deposited by pulsed laser deposition, ablating a YBCO sintered powder target using an externally modulated KrF excimer laser.

- **Protective cap-gold deposition (12)**: a 25 Å thick layer of gold is deposited by magnetron sputtering.

The parameters used in the fabrication procedure are summarized in Appendix C, in Table C.2 and C.1.

As shown in Figure 2.4, the YBCO film grows in the [103] direction, i.e. with the c-axis tilted by 45° respect to the substrate surface normal, whenever having a (110) STO surface underneath. Nevertheless, the growth of the YBCO film on the (110) oriented MgO substrate surface occurs along the [001], with the c-axis aligned with the normal to the substrate. Moreover, the YBCO $\hat{a}$ and $\hat{b}$ directions are rotated by 45° respect to the [100] and [110] direction of the MgO, to better accommodate the high lattice mismatch.

It's worth to point out that YBCO can grow with two competing crystallographic orientations when deposited on a perfectly [110] oriented STO surface. YBCO can in fact grow in the (103) direction or along the ($\bar{1}03$) one, switching the c-axis orientation and developing undesired grain boundaries that would impair the characteristic of the Josephson junctions. Such growth mode gives, as result, a film structure similar to the one shown

Material	$\frac{\Delta a}{a}$	$\frac{\Delta b}{b}$	$\frac{\Delta c}{c}$	ϵ	$\tan\delta$
$SrTiO_3$	$+2.0$	$+0.7$	$+0.1$	227	6×10^{-2} 100 K,300 GHz
MgO	-9.0	-6.7	-7.4	9.65	5×10^{-4} 100 K,300 GHz
$(Y)ZrO_3$	$+3.6$	6.3	5.8	25	8×10^{-3} 100 K,300 GHz

Table 2.1: Dielectric properties of STO, MgO and YSZ and lattice mismatch $\Delta a_i/a_i$ for with YBCO unit cell at different crytal orientations [27].

in Figure 2.5. To select only one direction its custom to use *vicinal* substrates, characterized by a slightly misaligned surface orientation. In this work we have used substrates with 6° vicinal angle, i.e. the angle between the substrate normal and its nominal direction.

2.2 Substrate Choice

In section 1.8.3 we have mentioned how the selection of a suitable substrate material can be determinant for a successful realization of a high-T_C SET. In Table 2.1 we compare the dielectric properties of a traditional substrate material for YBCO epitaxial deposition such as *strontium titanate* (STO) with non perovskite ones that have been selected as substrate material for the realization of the devices of this work.

The Table 2.1 shows the lattice mismatch between the YBCO and different possible candidate substrate materials. The optimal fitting of lattice parameter offered by STO, together with a — not shown — good matching of the thermal expansion coefficient, has been historically the main reason for the selection of such material as suitable substrate. The smaller the lattice mismatch, the easier it is to achieve epitaxial growth of the YBCO film. However, the high value of the dielectric constant ϵ in STO, as well as in many perovskite based materials, is a constraint that is not acceptable for the successful realization single electronics devices. Moreover the power dissipated at high frequencies by such materials, expressed in the loss tangent $\tan\delta$, is rather high and would impair the performances of our devices. Magnesium Oxide (MgO) and Yttria Stabilized Zirconia ($(Y)ZrO_3$ – YSZ) permit to achieve better performances in both senses, still allowing the epitaxial deposition YBCO, and therefore have been selected as substrate to realize the devices of this work.

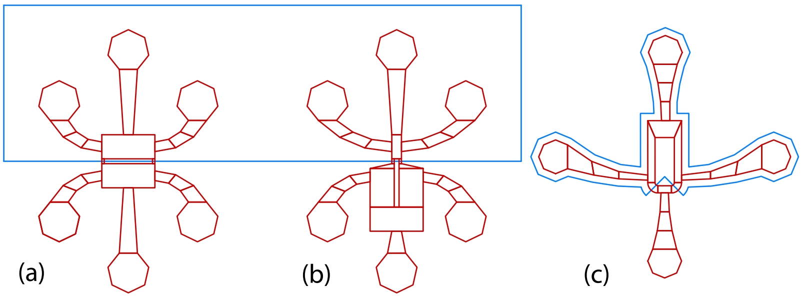

Figure 2.6: Grain boundary elongated (a) and Normally elongated (b) SQUID design used in the bicrystal sample. The design (c) has been used the biepitaxial sample.

2.3 Device design and Simulation

The chip layout has been designed to fit 5×5 mm substrates for both bicrystal and biepitaxial samples. The smallest pad dimension has been fixed to 90 µm, with 45 µm spacing between them to facilitate the wire bonding. At the same time, the largest possible number of pads has been fit in order to maximize the number of devices realized on the same chip. In the Biepitaxial sample only SQUIDs has been realized while, on the bicrystal one, we have fabricated both SQUIDs and SETs.

The SQUID design used in the biepitaxial and the bicrystal samples is quite different. We have mentioned before that the bicrystal samples have, as an intrinsic constraint, the need to align all the devices along the grain boundary line.
Previous investigations[28] have given the evidence of a strong kinetic contributions to the SQUID inductance when the current density distribution in the SQUID has a component along the c-axis. To further investigate such phenomenon, we have realized two elongated geometries with complementary orientation. In the grain boundary elongated geometry, shown in Figure 2.6(a), the transport occurs mainly within the a-b planes while, in the normally elongated geometry, shown in Figure 2.6(b), the current is forced to have a the c-axis component. A sketch of the current density orientation relative to the YBCO film for both geometries is given in Figure 2.7. In both designs the SQUID loop dimensions has been fixed to 2×20 µm. This allows to measure about ten critical current SQUID modulations with the values of magnetic fields available and, contemporary, avoid an unwanted distortion of the interference pattern due to big self-inductance effects. The junction sizes has been set to 1 µm and 2 µm in the normally elongated geometry. In the grain boundary elongated one, 1 µm and 2 µm and 4 µm wide junctions are available. These five different designs will be further

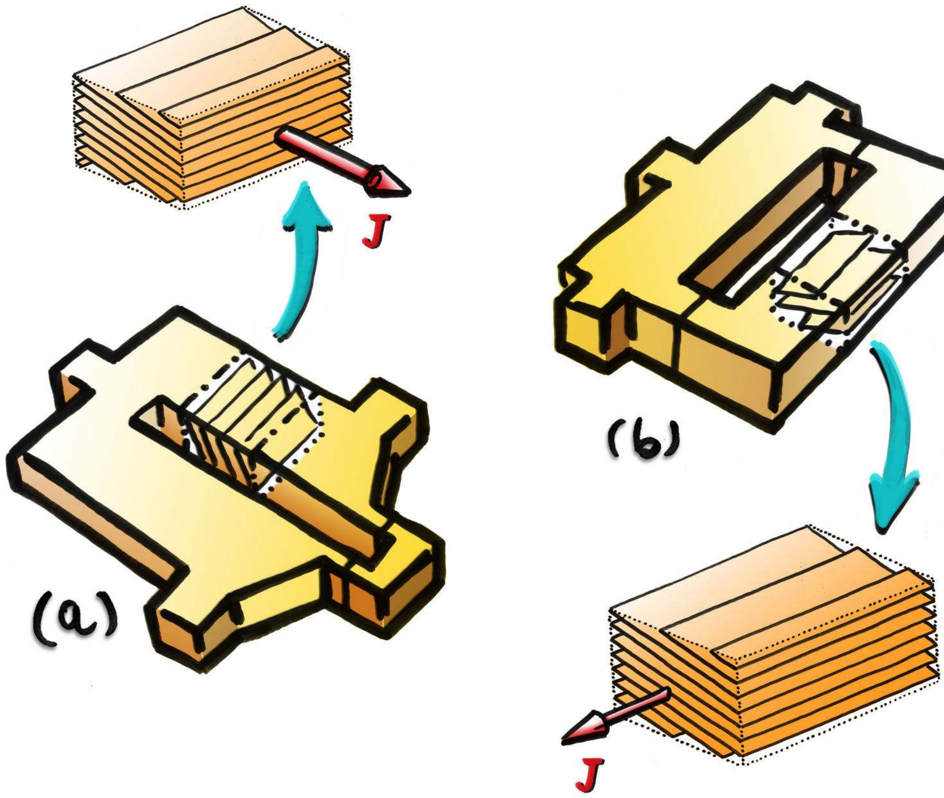

Figure 2.7: Two possible orientations of the Current density relative to the YBCO ab planes: in the grain-boundary elongated geometry (b) the current flows mainly within the ab-planes; in the normally elongated one (a) the current distribution has a bigger component of current transport in between the planes, along the c-axis.

indicated in order with *YSZ#1* up to *YSZ#5*.
In the biepitaxial sample the alignment constraint does not hold anymore. A different geometry, shown in Figure 2.6, has been chosen to probe the effect of the junction orientations. A bigger hole of 20×8 µm has been used while the junction size has been kept fixed to 3 µm. These geometry will further be indicated with *MgO/STO*.

All geometries have been simulated with the 3DMLSI software[29]. A value of London penetration depth λ_L has to be given as input to the software together with the geometry of both the SQUID and injection line. The 3DMSLI output consists of the the SQUID self-inductance L_{SQD}, the injection line self-inductance L_{INJ} and the SQUID-Injector mutual inductance $M_{\text{INJ-SQD}}$.
While the mutual inductance consists only of a geometric contribution, all self-inductances returned by the simulation software comprehend both the geometric and the kinetic parts. Therefore, some knowledge about the physics of these two contributions has to be exploited to distinguish between them. As stated in section 1.1.2, the kinetic inductance is always proportional to the square of λ_L. On the other hand, the geometric inductance, at least for small values of λ_L, has an almost constant value. The geometric and kinetic component can therefore be distinguished by repeating the simulations at different values of λ_L and by fitting the returned values with a simple linear model:

$$L_i(\lambda_L) = L_i + \frac{dL_i}{d\lambda_L^2}\lambda_L^2$$

The result of such fittings very much resembles, in all the geometries, the plots in Figure 2.8. In Table 2.3 the zero and first order regression coefficients are reported for all SQUID designs together with the correlation coefficient R^2. Values of R^2 close to unity correspond to very good fitting of the data. As expected, all self-inductances are very nicely fit by the model while the mutual inductances are almost constant functions of λ_L^2. The geometric part of the self-inductances can therefore be approximated with L_i while $\frac{dL_i}{d\lambda_L^2}\lambda_L^2$ returns roughly the kinetic inductance contribution.

We finally have simulated the inductance given by the "non-ideal" leads, feeding current to the injection line. Figure 2.9 show, as an example, the geometries used to describe the real and ideal injection line in the simulations for the geometry (a) of Figure 2.6. Such inductance contribution has been estimated to be always less than 0.5 pH. An exception is the upper injection line in the normally elongated geometry, in which the contribution can rise up to 1.5 pH.

To design the Single Electron Transistor, we have employed the smallest junction size that could permit the YBCO to be still superconducting after

SQUID	**YSZ#1**	**YSZ#2**	**YSZ#3**	**YSZ#4**	**YSZ#5**	**MgO/STO**
SQUID Geometry	(a)	(a)	(b)	(b)	(b)	(c)
Hole dimensions, µm	2×20	2×20	2×20	2×20	2×20	8×20
Junction Width, µm	1	2	1	2	3	3
L_{SQD}, pH	16.33	16.12	16.67	16.35	16	29.9
$\frac{dL_{SQD}}{d\lambda^2}$, pH/µm^2	120.8	90.15	117.49	87.51	69.45	166.6
R^2	0.999	0.999	1.000	0.999	0.999	1.000
M, pH	9.37	9.53	4.28	4.67	5.32	21.55
$\frac{dM}{d\lambda^2}$, pH/µm^2	1.52	1.311	0.754	0.86	1.09	0.83
R^2	0.988	0.971	0.915	0.914	0.915	0.896
L_{INJ}, pH	12.66	12.74	9.418	10.58	12.95	22.96
$\frac{dL_{INJ}}{d\lambda^2}$, pH/µm^2	41.15	40.68	22.51	24.27	27.71	126.99
R^2	0.999	0.999	1.000	1.000	0.999	1.000

Table 2.2: Linear least-squares fitting parameters and correlation factor R^2 for the SQUID geometries. In the SQUID geometry row, (a),(b) and (c) refer to Figure 2.6 . The mutual inductance values, diversely than the self-inductance ones, are badly fitted by a linear approximation and tend to saturates to a constants for high-values of London penetration depth.

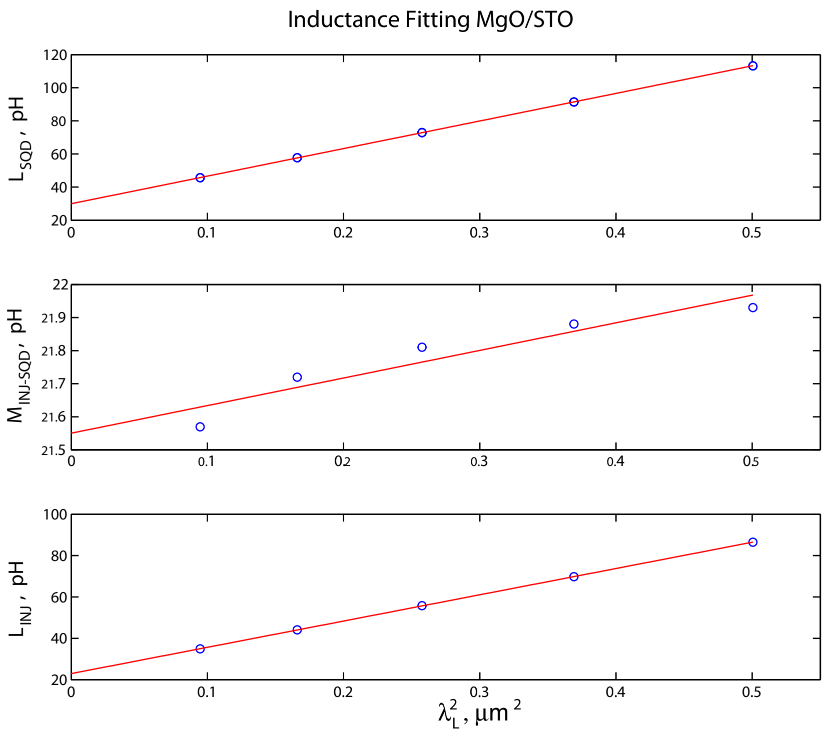

Figure 2.8: Linear fitting of the self and mutual inductances between SQUID loop and Injection Line.

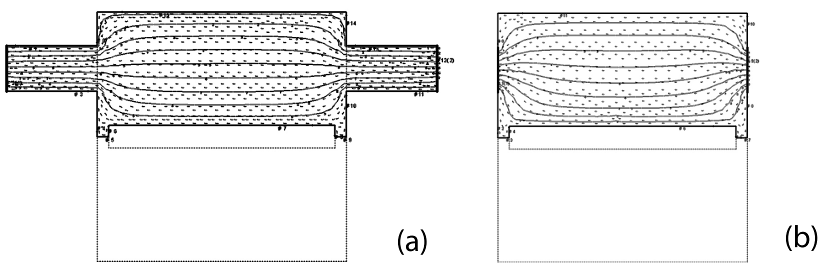

Figure 2.9: Geometry used to simulate the effect of a real(a) and ideal(b) injector and current density distribution in the geometry YSZ#3.

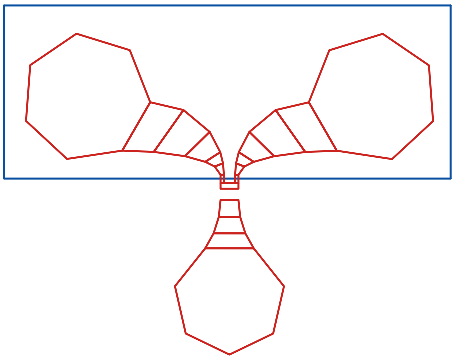

Figure 2.10: High T_C Single Electron Transistor design.

the device patterning. The SET junctions are 0.3 and 0.5 µm close to the grain boundary position and, as shown in Figure 2.10, broaden up to 4 µm with increasing distance from the junction region. In this way the leads act as oxygen reservoirs and contribute to preserve as much as possible the YBCO superconductivity. To further shrink the 150 nm thick junctions, the SET has been milled by using a Kauffman Broad Argon Ion source[1] to a thickness of 100 nm.

[1]An aluminum mechanical mask has been used to prevent the SQUID to be etched as well

2.4 Device fabrication

In this section we will review the procedure needed to pattern the devices. Because of the close similarity of patterning bicrystals and biepitaxial samples, we will describe only the procedure to pattern the devices in the YBCO bicrystals. Such procedure is slightly more complicated because of the need to identify the exact grain boundary position and adapt the whole pattern to each individual sample.

2.4.1 Electron beam lithography

All the device structures have been defined by electron beam lithography. We have used a commercial JEOL 5DII. The system is provided with a LaB_6 source, emitting electrons at 50 keV, and a set of five lenses. The first three make the beam collimated and coaxial with the electron-optic system. Two objective lenses, called 4^{th} and 5^{th} lens, are available with different working distances and width of the pupil. By using either the 4^{th} ot the 5^{th} lens, high current–low resolution and small current–high resolution exposure modes are respectively possible. The two exposure modes also differ for the field sizes, i.e. the maximum area that the beam can expose without any movement of the stage. The pattern, defined in an `AutoCAD DXF` file, is converted into a format readable by the machine using a proprietary *JEOL* software. The settings used to expose the different layers are shown in Appendix A.

2.4.2 Lift-off

Positive resist has been used in all lithgraphies. This kind of resist becomes soluble in the resist-developer when exposed to the electron beam. The lithography technique used, called *lift-off*, is based on the following steps, sketched in Figure 2.11:

- the sample is covered with a thin layer of resist by spin-coating.
- the resist is exposed with the desired pattern.
- the resist film is developed.
- a thin film of a desired material is deposited on top of the structure.
- the remaining resist, together with the material on top of it, is *lifted off* with the aid of some solvent.

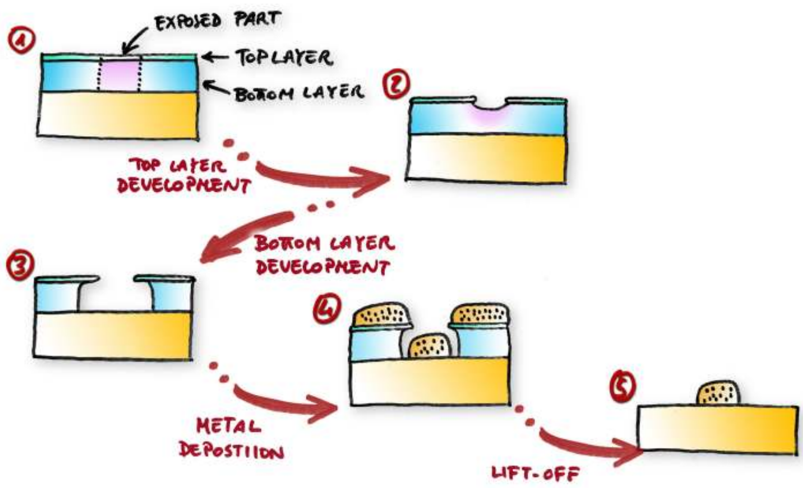

Figure 2.11: Steps used in the lift-off technique. A double layer of resist is used to realize the undercut structure.

For the unexposed resist to be removed after the metal deposition it is important that the metal film deposited on the bare substrate is physically separated from the one deposited on top of the resist layer. This limits the thickness of the metal film deposited to be smaller than the resist one. To further avoid the film to be deposited on the edge of the resist layer it is custom to use directional deposition techniques — such as the electron beam evaporation — and to develop a resist structured with an undercut. A very simple way to realize such structure, sketched in Figure 2.11, is to coat the sample with two layers of resist which can be developed independently. By developing the bottom layer with long enough time it is possible to control the depth of the undercut. The details of the procedure used in such fabrication step are summarized in Appendix B.

2.4.3 Grain-boundary compensation

The first fabrication steps, indicated from 1 to 5 in Figure 2.12, involve the definition of reference crosses and rulers as well as gold pads. Such structures are defined evaporating a 2400 Å thick film of Gold, using the above mentioned lift-off technique.
To proceed with the YBCO patterning steps it is necessary to modify the e-beam mask, so that the position of the “devices” block can be adapted to the specific position and orientation of the grain boundary relatively to the reference system defined in the previous lithography step. To implement this step, two optical micrographs are taken in the region where the rulers

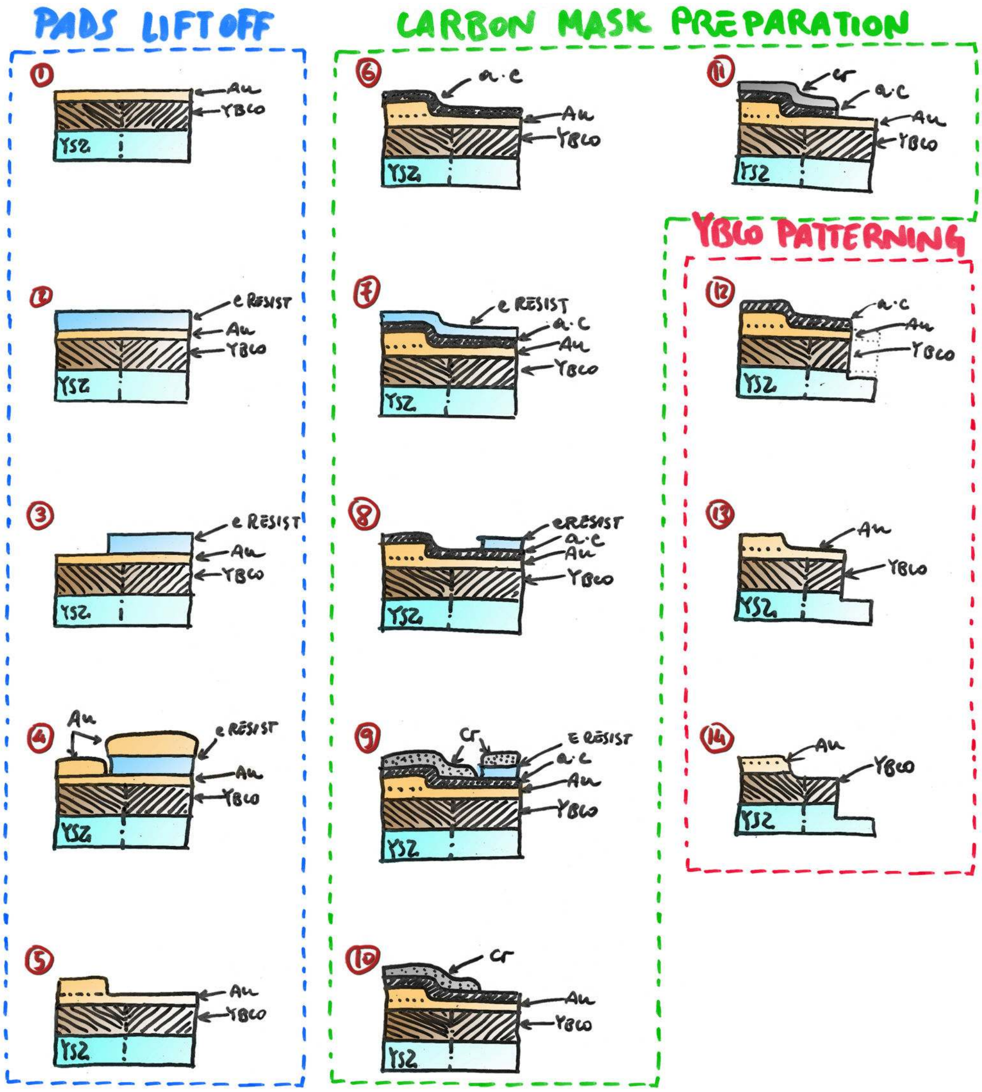

Figure 2.12: Steps used in the bicrystal sample fabrication.

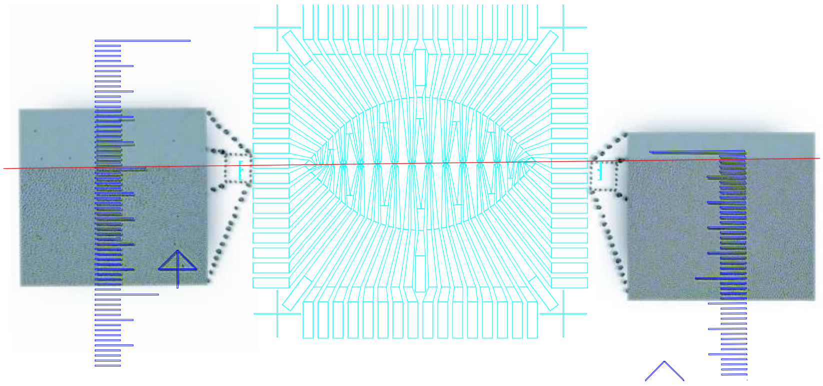

Figure 2.13: Insertion of the grain boundary position information by using optical micrographs. The e-beam lithography pattern can be corrected to compensate the misplacement from the nominal position.

are defined. If we assume the grain boundary to be perfectly straight, it is possible to extrapolate its position in the whole sample from the optical micrographs of rulers, as it is shown in Figure 2.13. Thereafter, the whole block of devices is translated and rotated to compensate for the new grain boundary orientation and offset from the nominal central position.

2.4.4 Amorphous carbon mask and YBCO patterning

The updated pattern can be used to fabricate an amorphous carbon mask. Such mask will partially cover and "protect" the YBCO film from the etching action of the argon ion beam while milling. The reason for employing amorphous carbon instead of the resist layer itself is due to the the extraordinary slow etching rate of the YBCO — a normal resist layer would etch much faster than the YBCO under the Ar^+ beam. The amorphous carbon has been selected among other materials[30] because of its etching rate under argon ion beam, much slower than the YBCO one, as well as the ease of removal under oxygen plasma. To realize the carbon mask, we have executed the following steps (we refer to Figure 2.12 while numbering the steps):

- A thin amorphous carbon film is deposited uniformly on the sample (6).
- A thin chromium mask is deposited by lift-off on top of the carbon film (6→10). Previous to the chromium evaporation, alignment of each device with the grain boundary is controlled and, if necessary, corrected as shown in Figure 2.14.

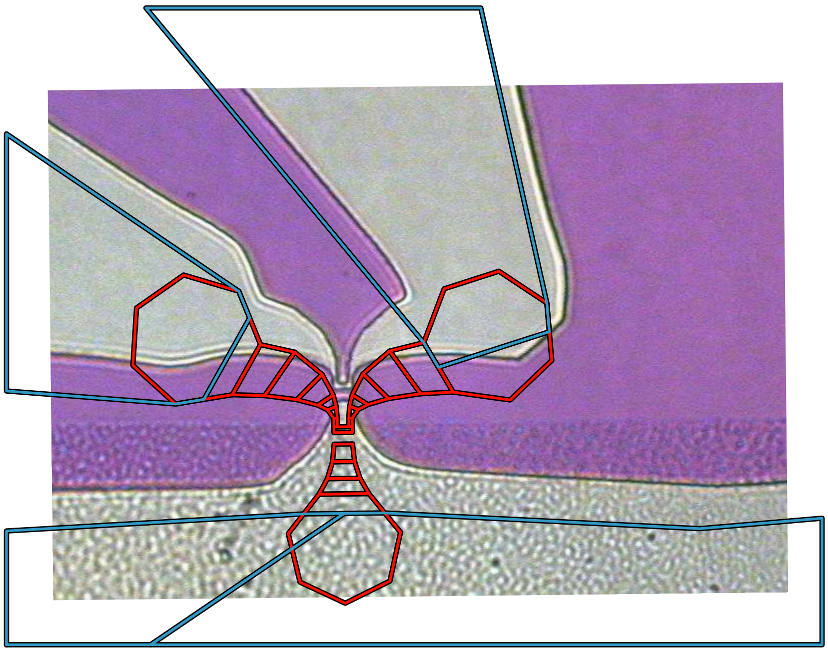

Figure 2.14: Correction of a single device position — SET in this case — employing optical micrographs of individual devices.

- The amorphous carbon film is selectively removed from the regions left uncovered by the chromium mask by oxygen plasma etching (11).
- The YBCO film is milled by using Kauffman broad argon ion beam source (12). The etching procedure is repeated until an infinite resistance is measured between two insulated Au/YBCO islands on the chip.
- The residual carbon mask is removed by oxygen plasma reactive ion etching (13).
- The cap-gold film is removed by argon ion milling (14).

Some optical micrographs of the final devices are shown in Figure 2.15 .

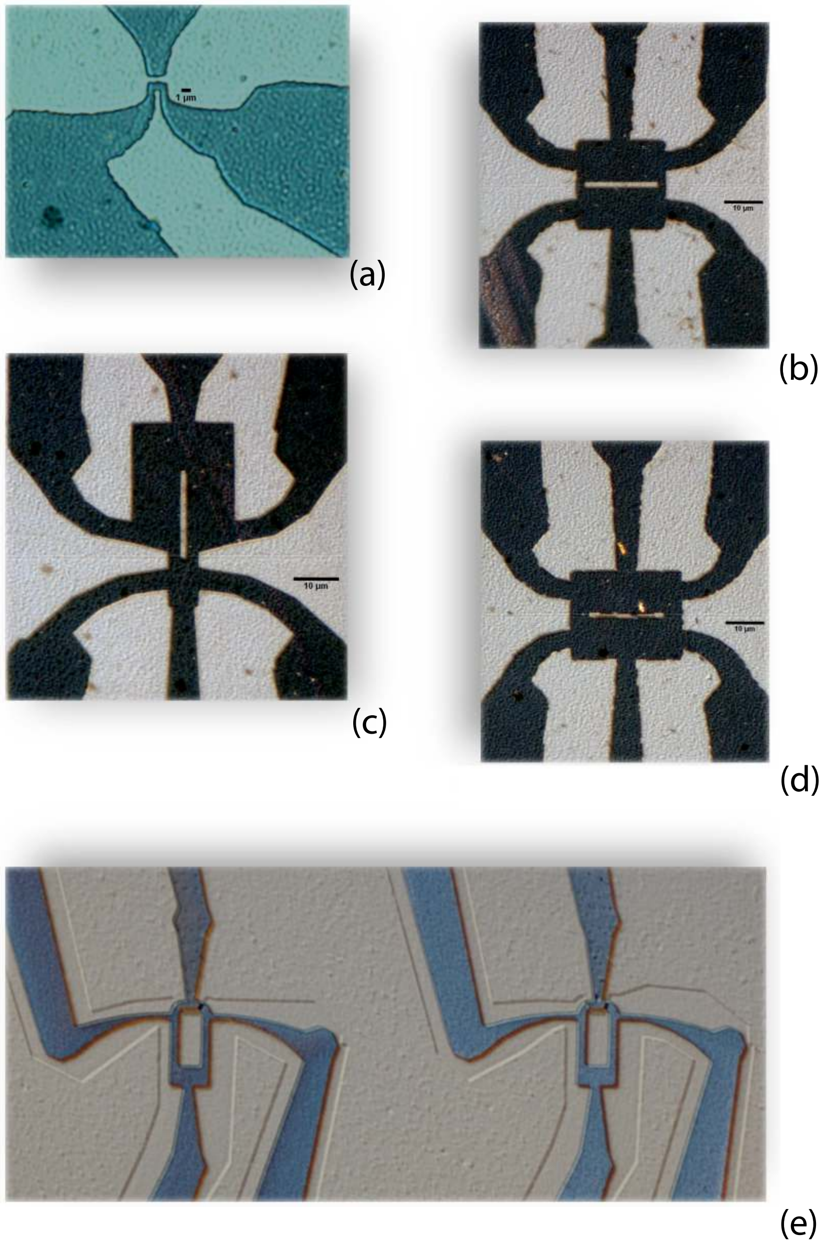

Figure 2.15: Optical micrographs of the measured superconducting devices: (a) Shows one SET realized in the YSZ bicrystal; (c) (b) and (d) show respectively the bicrystal SQUIDS indicated respectively with YSZ#1, YSZ#3 and YSZ#5; (e) shows two biepitaxial SQUIDs.

2.5 Measurement Setup

All measurements have been done in an Oxford Instruments Heliox VL system, a ^{3}He charcoal-absorber based cryostat capable of reaching temperatures below 300 mK. The structure of a cryostat similar to the one used is shown in Figure 2.16. While measuring, the Heliox VL deepstick is inserted in a liquid ^{4}He dewar, which contains both a μ-metal and a superconducting magnetic shield. The whole system is located into an Electromagnetic Interference shielded room. The system is equipped with a small magnetic coil which can generate magnetic fields of the order of 2 mT.
Temperatures of 4.2 K can be obtained dipping the stick into the ^{4}He bath. A temperature of 1 K can be reached by pumping on the liquid ^{4}He contained in the so called ^{4}He pot. When this temperature is reached, a charcoal absorber can be heated up to release ^{3}He and liquid ^{3}He gets condensed into the so called ^{3}He pot. By pumping on such liquid with the charcoal absorption pump — now free of ^{3}He gas — the cryostat reaches 280mK. All devices have been measured in current bias mode, generating a slow[2] sawtooth signal with an Agilent 33220A. Such signal generator is connected with a resistance R_{ser} which limits the current that can be fed into the device. The resistance value, ranging from 100 kΩ to 1 MΩ, is chosen so that the impedance of the measured device is always much smaller than R_{ser} and, at the same time, a suitable current interval is spanned. The current fed into the device is obtained by measuring the voltage across the resistor R_s with a battery driven Princeton Applied Research 5113 differential pre-amplifiers. An amplifier of the same kind is used to directly measure the voltage drop across the SQUID. All the voltages are then converted into digital form by a National Instruments DAQ. The SQUIDs have been measured in two different ways, shown in Figure 2.17. When measuring the current-voltage characteristic at varying magnetic fields, a Yokogawa 7651 DC source, set in the current source mode, has been used to drive the current trough the internal coil of the cryostat. When measuring the current-voltage characteristic for different values of the *injection current* I_j, the Yokogawa source has been set in the voltage source mode and used as input to an instrumentation amplifier. The instrumentation amplifier, connected as shown in Figure 2.18, acts as ground breaker and ensures that all the current injected into one line is taken away from the other injector lead, avoiding to drain current into other terminals. The insertion of a 5.5 kΩ resistor in series to the injection leads permits to limit the current fed to $V_{YOKO}/5.5$ kΩ — V_{YOKO} being the voltage generated by the Yokogawa source. To avoid instabilities of the instrumentation amplifier, a resistance of 1 MΩ

[2] The current bias fundamental frequency was never higher than 10 Hz.

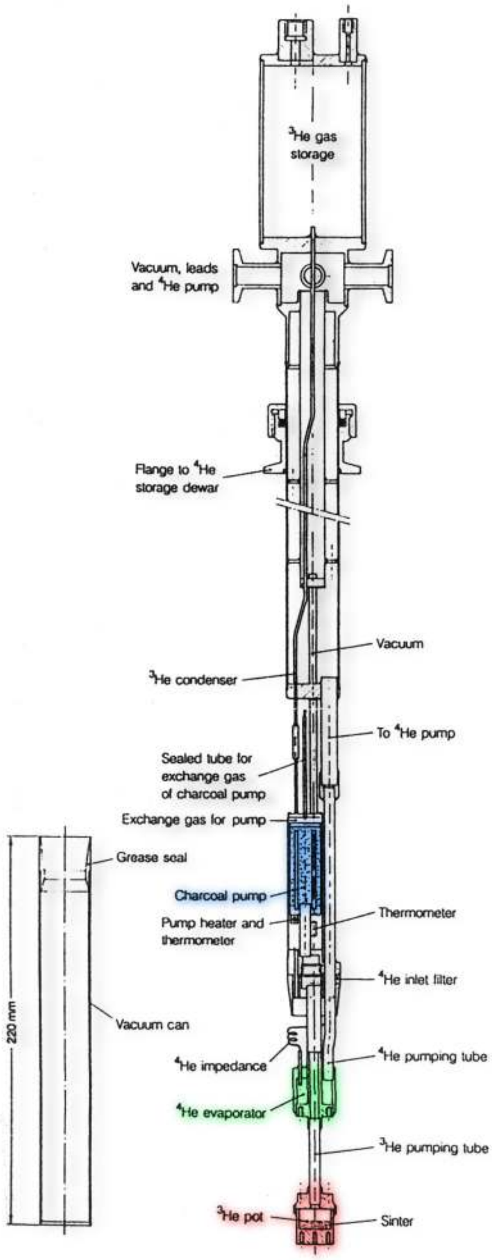

Figure 2.16: Schematic of an L^{4}He charcoal-absorber cryostat[31]. Charcoal absorber ^{4}He-pot and ^{3}He-pot are highlighted rispectively in blue, green and red.

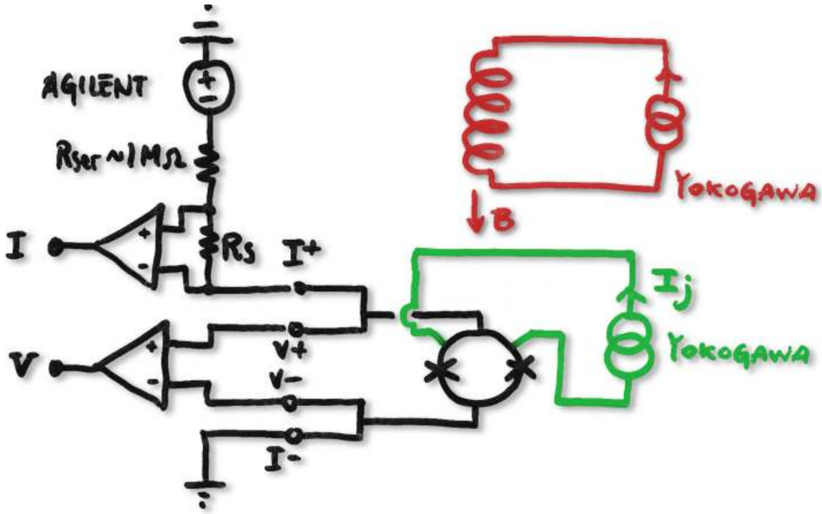

Figure 2.17: Schematic of the SQUID measurement setup. The Yokogawa current generator can be used to feed current to the coil (red circuit) and generate magnetic field, or to feed current through one interferometer branch through the injection lines (green circuit). The ground-breaking between current source and the measurement setup is not shown.

is used to shunt the two independent grounds. The SET has been measured by current bias, as shown in Figure 2.19. The gate voltage has been swept by the Yokogawa generator in the voltage source mode, as shown in Figure 2.19 .

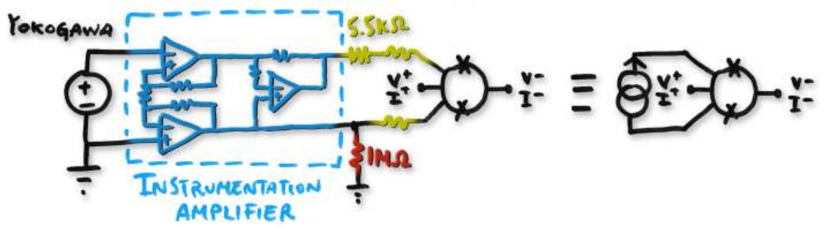

Figure 2.18: An instrumentation amplifier (INA) is used as ground-breaking circuit. The injection current value is set by the control resistance in series with the resistance of the cryostat leads. To avoid the instability of the INA, a 1 MΩ resistance shunts the independent grounds.

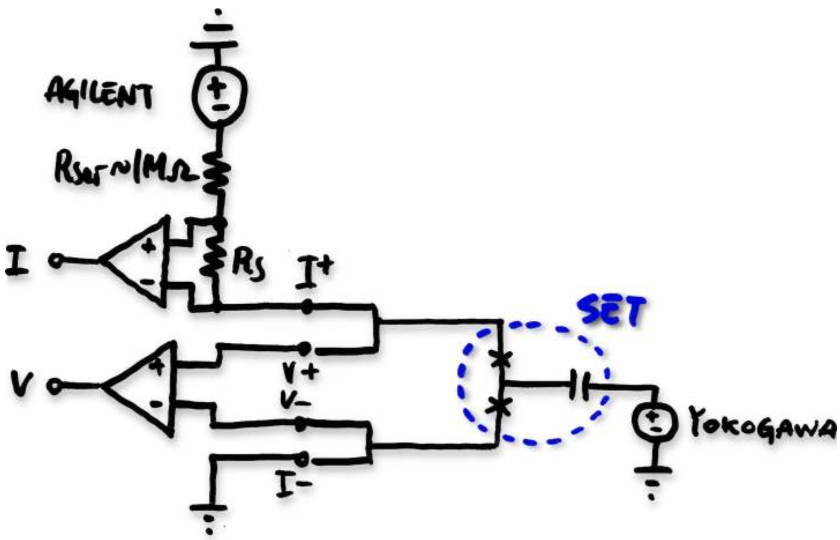

Figure 2.19: Lumped elements model of the SET measurement setup.

Chapter 3

Results and discussion

The goal of this thesis work is to establish whether it is feasible to realize a Single Electron Transistor based on YBCO grain-boundary junctions. As discussed in section 1.8.3, to realize an SET we need, as basic building block, tunnel junctions with both small capacitance and high normal resistance. Small capacitances are needed for the charging energy of the SET to be higher than any possible thermal energy fluctuation. In particular, for coulomb blockade of tunneling to be effective at a temperature of 1 K, junctions with capacitance lower than 1 fF are needed. Moreover the normal resistance of each junction has to be higher than 25 kΩ for quantum fluctuations to be ineffective in washing away the Coulomb blockade.
If the estimation of a junction's normal resistance requires only to measure the slope of the current-voltage characteristic at high bias voltage, measuring capacitances lower than 1 fF is certainly more complicated.

3.1 SQUID measurements

To determine the capacitance of the Josephson junctions of this work, we have carried on the characterization out some SQUIDs, realized in two different technologies — biepitaxial and bicrystal technology. The value of junction capacitance has been extracted by measuring the voltage at which a particular current peak occurs in the current-voltage characteristic. Such peak, attributed to a so called *SQUID resonance*, is caused by the non linear interaction between the Josephson circulating currents with a resonator formed by the junction capacitance and the inductance of the superconducting SQUID loop.
A detailed description of this phenomenon is given in section 1.9. Anyway

we recall that the voltage at which such step occurs has to be a multiple of:

$$V_{\text{SQUID}} = \frac{\hbar}{2e}\sqrt{\frac{2}{LC}}$$

where C is the capacitance of a single junction of the SQUID, while L is the SQUID self-inductance. In particular, the current step due to the first order of resonance, which occurs at V_{SQUID}, will be maximized whenever we induce an "effective" external flux Φ_x of:

$$\Phi_x = \Phi_0 \left[\frac{1}{2} + n\right] \qquad \text{, with integer } n$$

By measuring the voltage at which the current step occurs we can have an accurate estimation of the product LC and, with an independent measurement of L, we can determine the value of capacitance C. The methodology used to extract the SQUID self inductance L will be treated later in this section.

The characterization of all the SQUIDs presented in this section[1] has been done by measuring the current voltage characteristic at different values of "effective" magnetic flux, generated by injecting a constant current I_{inj} through one of the branches of the Josephson interferometer. All the measurements shown in this chapter have been performed at 280 mK.
In figure 3.1(c) we show two current-voltage characteristic curves of a SQUID, acquired at two distinct values of injection current which correspond to values of "effective" magnetic flux of Φ_0 (blue curve) and $\Phi_0/2$ (green curve). A current peak is clearly visible at voltages close to 0.5 mV in the green curve while, in the blue one, such peak disappears. To enhance the peak visibility, in Figure 3.1(d) we have plotted the difference between the SQUID current and the linear fit obtained at high bias voltages. Such current will further be indicated as *Josephson current contribution.* Figure 3.1(e) represents the differential conductance dI/dV plotted against the voltage drop across the SQUID. We can see that the current peak occurs roughly at the intersection of the two conductance graphs. Finally, we represent in 3.1(d,e) the conductance expressed in dBS with:

$$G|_{\text{dBS}} = 10\ \log_{10}\left[\frac{|G|}{1S}\right]$$

and plotted against

[1]An exception is the measurement of the biepitaxial SQUID MgO/STO#2, which has been characterized only by measuring the I-V curves with different applied magnetic fields

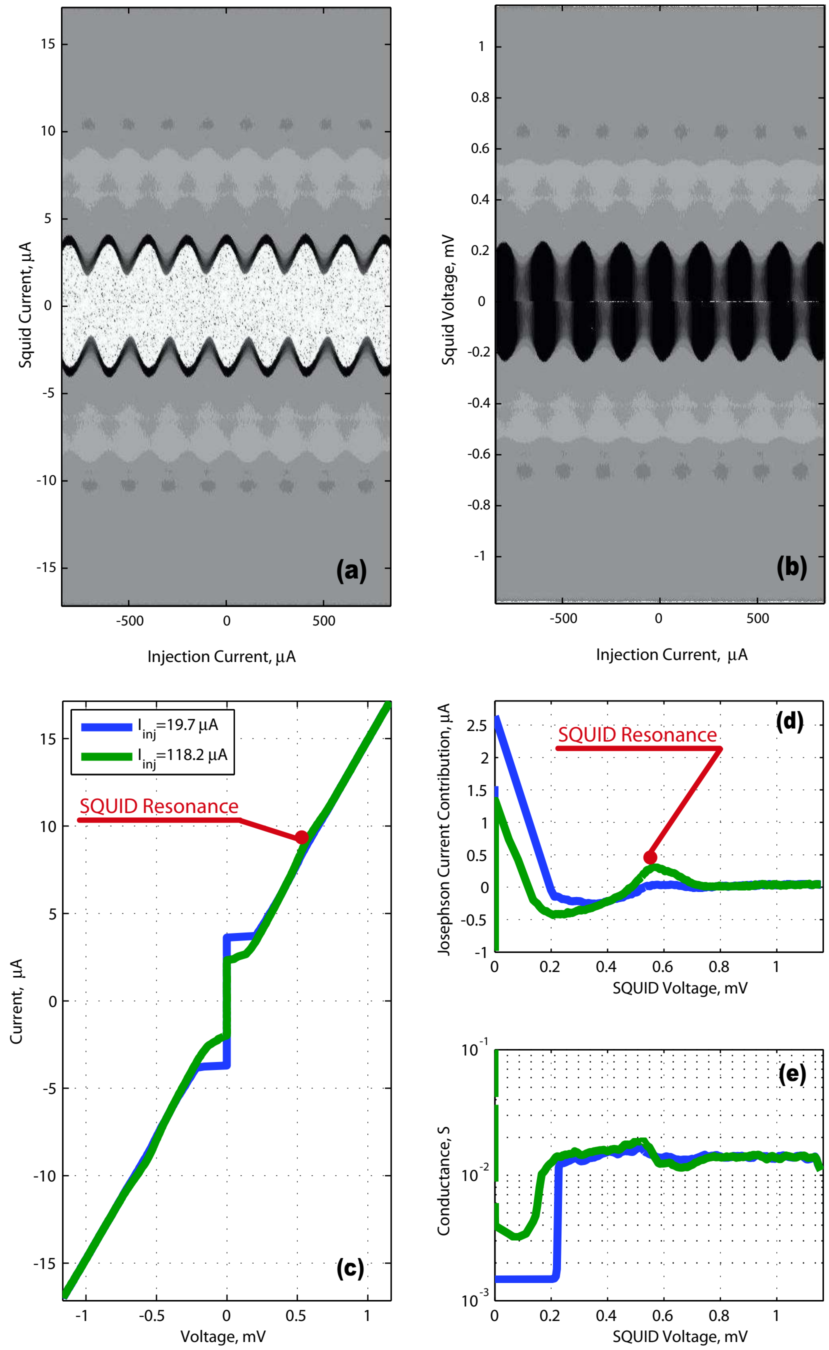

Figure 3.1: Plots of the bicrystal SQUID YSZ#1: G-I plot(a); G-V plot (b); I-V characteristic (c); Josephson current contribution (d); Conductance plot (e). The measurement has been done at 280 mK.

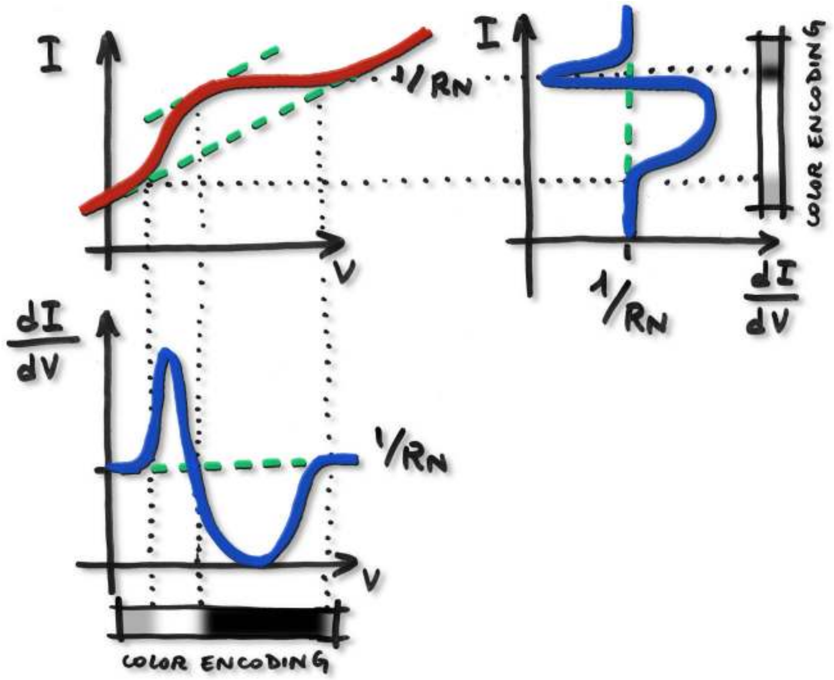

Figure 3.2: Graphical representation of a excess current peak by plotting the differential conductance as a function of voltage or current. The measurement has been done at 280 mK.

- the *injection current* I_{inj} and
- the current I or the voltage V across the squid;

We will further refer to *G-I* and *G-V plots* when talking about the $G(I_{\text{inj}}, I)$ or the $G(I_{\text{inj}}, V)$ color plot.

The G-I and G-V plots graphs contain a lot of information and some explanation might help to correctly interpret the graphs. The conductance is represented by gray-scale color encoding. High values of conductance are represented with a bright color while, vice versa, low ones are represented by a dark color. As a consequence of this representation, a peak is identified whenever a bright-dark colored sequence is found in the plot. The bright region represents the part of the current step at which the current grows up. On the other hand, the dark region represent the flat part of the step, at which the extra current contribution diminishes with increasing voltage. Figure 3.2 provides a support to this interpretation.
It's worth to point out that the two regions of the step will have different visibility whether we are looking at the G-I plot or at the G-V plot. The rising part of the current step will in fact have a big extension in current together with a small variation of voltage. Therefore, this part of the step

will be predominant in the G-I plot while in the G-V plot will be concentrated into a single line. On the contrary, the "plateau" of the current step will have an almost constant current and a big extension in voltage, i.e. it will be more visible in the G-V rather than in the G-I plot, where it will be concentrated on a curve.
Furthermore, it is worth to notice that the critical current interference pattern is represented as the boundary of the bright colored central region of the The G-I plot[2]. The G-I plot, therefore, conveys in one single graph the information of the critical current pattern and the current step features we are interested in.

The same kind of SQUID resonance step has been observed in two other biepitaxial SQUID, indicated with MgO/STO#2 and MgO/STO#3. Figure 3.3 and 3.4 respectively show the set of plots for these two devices.
In such measurements the excess current caused by the SQUID resonance occupies a wide voltage range and its contribution is immediately visible from the IV curves. Such current step however is overlapped with a series of smaller steps, occurring at evenly spaced voltages. Current steps of the same kind have been observed also in the measurements of bicrystal SQUIDs YSZ#3 and YSZ#5. The set of plots for these devices are shown in Figure 3.5 and 3.6. We believe that the origin of such steps resides in the non linear interaction of the SQUID, acting a single distributed junction, with an external resonator. Such resonator might be formed by the superconducting leads which are capacitively coupled to the substrate and, therefore, act as a transmission line. At evenly spaced frequencies such structure acts as a short circuit and, in the neighborhood of such spectral regions, we can describe the resonator with a series LC lumped model. The interaction of a single junction with such resonator has been described in section 1.10. Here we only highlight that such junction-resonator interaction causes the current step to be proportional to the critical current for all orders of resonance, as it has been observed in our measurements.

After having identified the voltage at which the SQUID resonance occurs, we still need to estimate the SQUID self-inductance to extract a value of junction capacitance. We recall, from section 1.6, that the SQUID critical current is a periodic function of the external flux, with periodicity of one flux quantum Φ_0. If the external flux is generated — as in our experiments — by injecting a current through one branch of the Josephson interferometer,

[2]The presence of black dots in such region are due to the presence of noise in the voltage measurements that, in theory should be oscillating around zero for currents below the critical one.

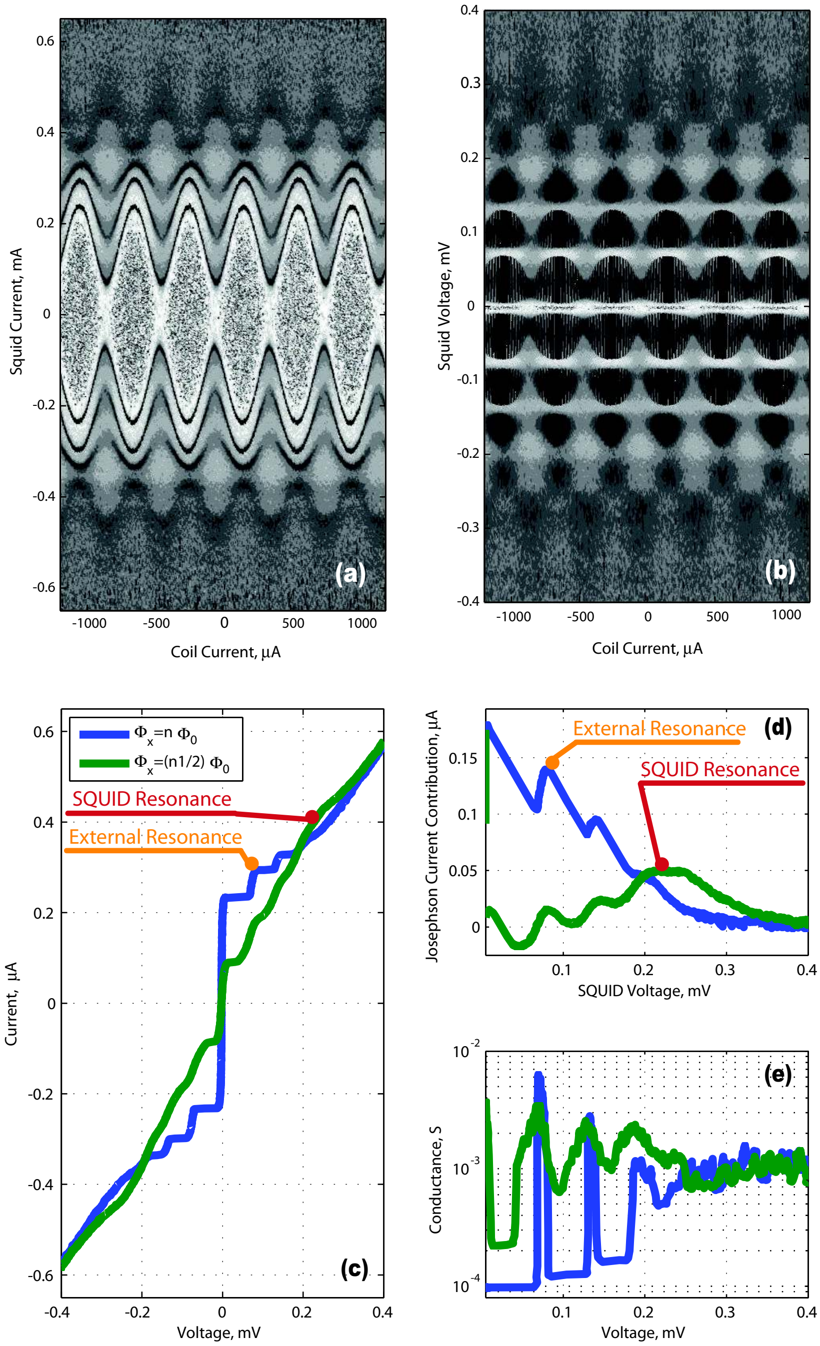

Figure 3.3: Plots of the bicrystal SQUID MgO/STO#2: G-I plot(a); G-V plot (b); I-V characteristic (c); Josephson Current contribution (d); Conductance plot (e). The measurement has been done at 280 mK.

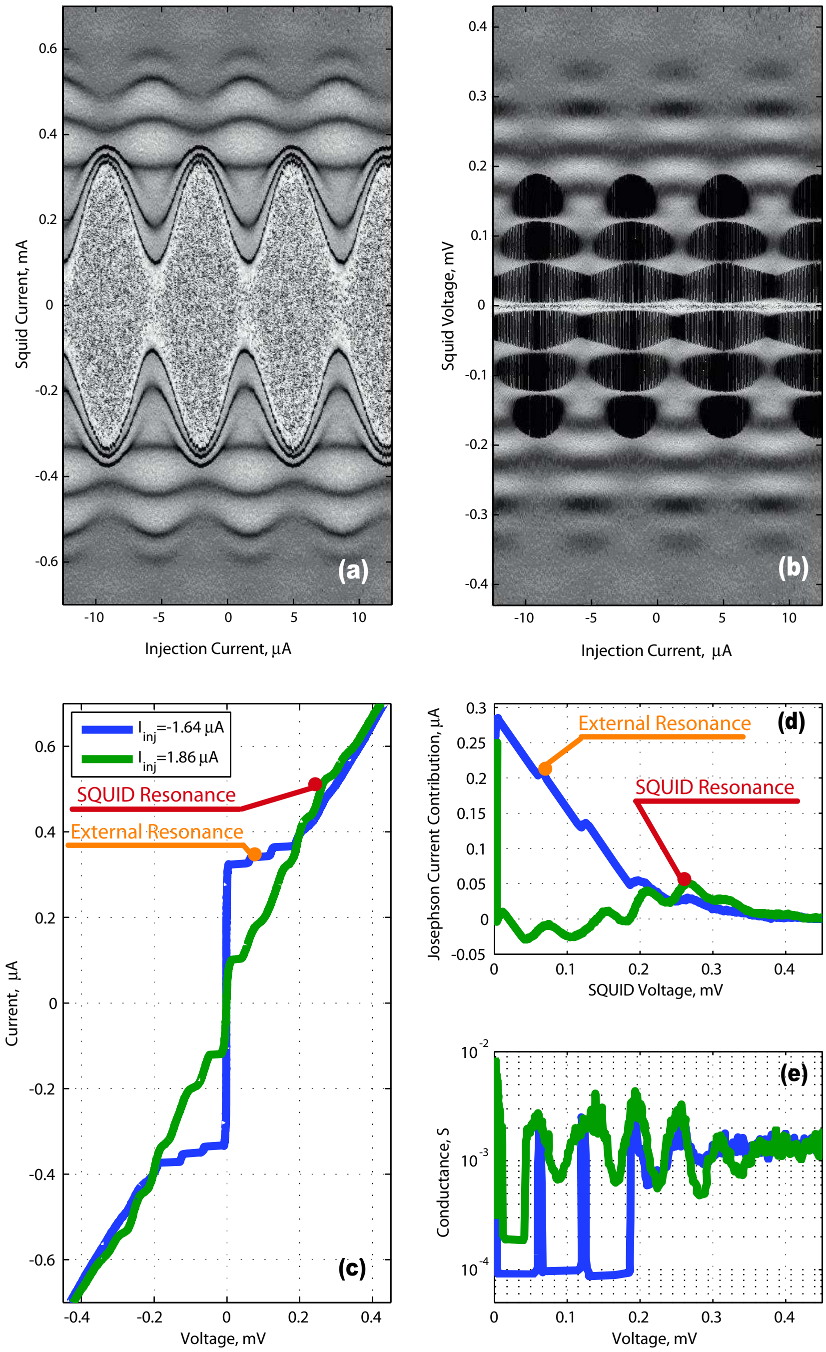

Figure 3.4: Plots of the bicrystal SQUID MgO/STO#3: G-I plot(a); G-V plot (b); I-V characteristic (c); Josephson Current contribution (d); Conductance plot (e). The measurement has been done at 280 mK.

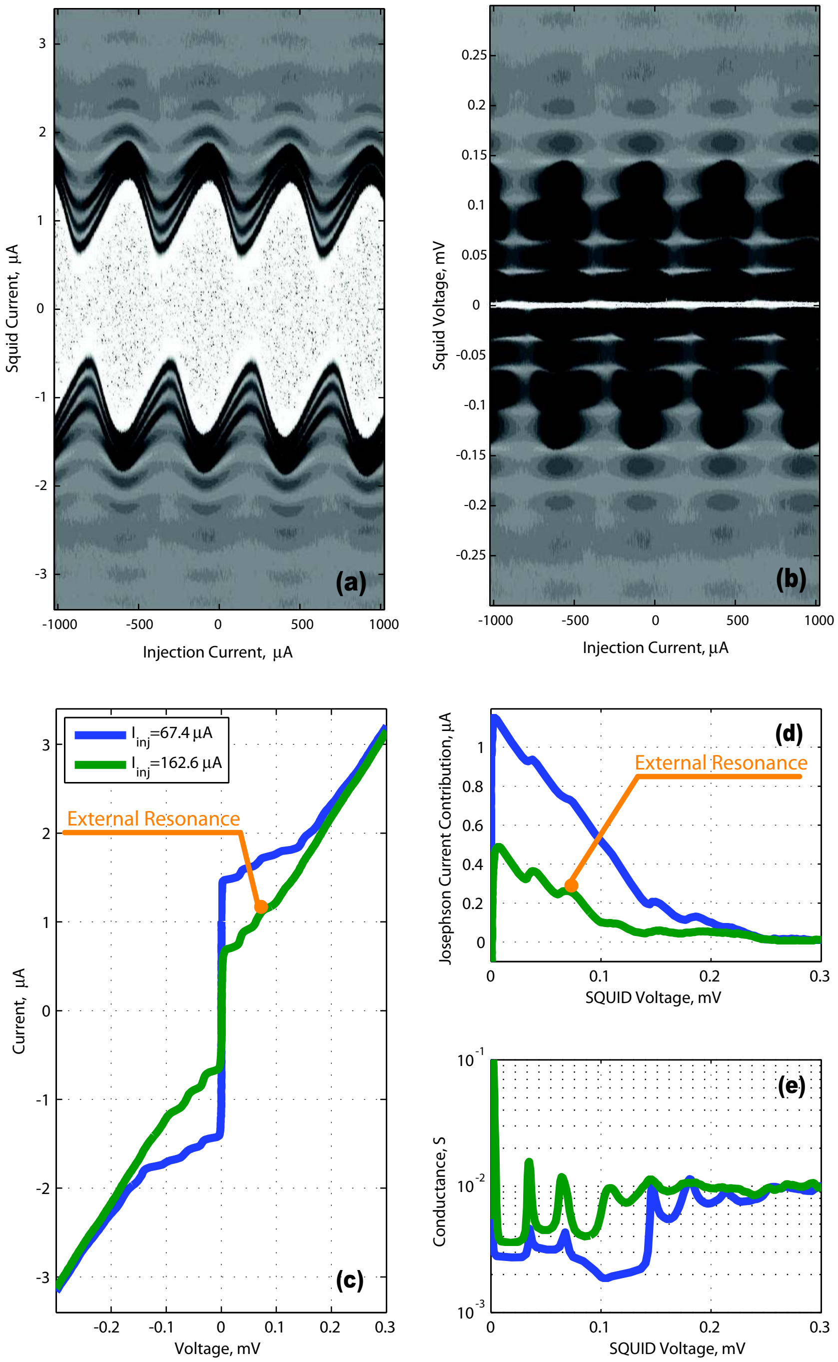

Figure 3.5: Plots of the bicrystal SQUID YSZ#3: G-I plot(a); G-V plot (b); I-V characteristic (c); Josephson Current contribution (d); Conductance plot (e). The measurement has been done at 280 mK.

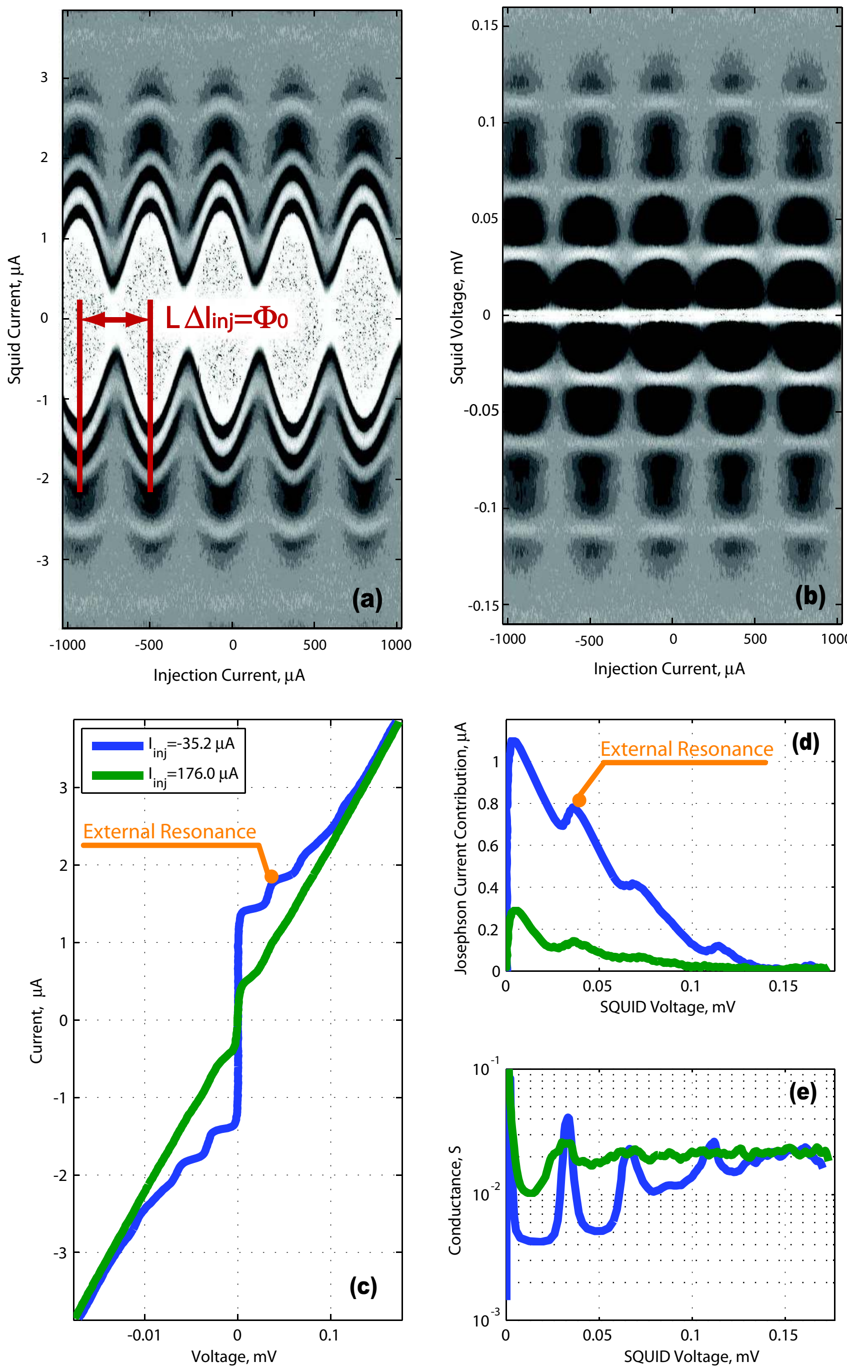

Figure 3.6: Plots of the bicrystal SQUID YSZ#5: G-I plot(a); G-V plot (b); I-V characteristic (c); Josephson Current contribution (d); Conductance plot (e). The measurement has been done at 280 mK.

we can extract a value of inductance L_{meas} from the current period ΔI_{inj} as:

$$L_{\text{meas}} = \frac{\Phi_0}{\Delta I_{\text{inj}}}$$

In Figure 3.6 we give a graphical representation of the origin of the above mentioned formula.

Different contributions add-up to the measured inductance, i.e.:

- a geometric mutual inductance $M_{\text{INJ-SQUID}}$ between the injection line and the SQUID loop,and
- a kinetic inductance contribution L_{kin} due to collisionless behavior of the cooper pair fluid.

To distinguish between them, we can repeat the simulations done in the design phase — summarized in section 2.3 — taking care of adjusting the nominal dimensions of the model to fit the real geometry of each SQUID. Optical micrographs of the devices, like the ones shown in Figure 2.15, can be used in this phase.
We recall, after section 2.3, that $M_{\text{INJ-SQUID}}$ is almost invariant with the London penetration depth while, on the other hand, the kinetic inductance contribution L_{kin} is proportional to the square power of the London penetration depth λ_L. We can therefore estimate both $M_{\text{INJ-SQUID}}$ and L_{kin} from the linear fits of such quantities against λ_L^2.

In Table 3.1 we summarize some of the physical quantities measured for the different devices together with the outcome of the 3DMLSI simulations. We indicate with *1 degree order* and *0 degree order* respectively the slope and the intercept of the linear fitting $L_i(\lambda_L^2)$, where L_i can be $M_{\text{INJ-SQUID}}$, L_{SQUID} or L_{INJ}.

A value for the kinetic inductance contribution can be extracted by subtracting the simulated mutual inductance value $M_{\text{INJ-SQUID}}$ from the measured one L_{meas}. A consequence of the anisotropy in London penetration depth of the YBCO (as indicated in Table 1.1) is that we should be able to observe a bigger kinetic inductance whenever the current transport has a component in the c-axis, at which λ_L has its maximum value. Our measurements are qualitatively in line with this consideration if we notice that the extracted kinetic inductance contribution is:

- almost negligible for the devices YSZ#3 and YSZ#5, where the current transport occurs mainly along the ab planes,
- bigger for the SQUID YSZ#1, where the current transport has its largest component among the bicrystal SQUIDs, and

Sample Type	YSZ			MgO/STO	
Device ID	**1**	**3**	**5**	**2**	**3**
Geometry	(a)	(b)	(b)	(c) θ=13°	(c) θ=27°
Junction Width, µm	2.00	1.35	4.89	3.00	3.00
Film Thickness, nm	150	150	150	120	120
Film Critical Temperature, K	88.0			87.5	
Do we have injectors ?	Y	Y	Y	N	Y
Injection Line Resistances, Ω	5550	5550	5550	×	200000
Measurement summary	**T=280mK**				
Current range, µA	17.00	3.85	9.70	0.73	2.03
Voltage range, mV	1.16	0.32	0.39	0.58	1.28
Rn, Ω					
max	83.0	79.0	46.6	774.0	636.0
min	80.1	67.0	45.9	774.0	636.0
I_c, **µA**					
max	1.80	1.36	1.38	0.24	0.26
min	1.16	0.50	0.43	0.08	0.03
L_{inj}, **pH**					
Upper Line	1.778	4.065	4.731	×	292.724
Lower Line	9.834	4.051	4.820	-	-
SQUID resonance, mV	**0.567**	×	×	**0.247**	**0.264**
Simulated Inductances					
$L_{\mathbf{SQUID}}$ **:**					
0° order, pH	14.438	14.499	12.939	29.923	
1° order, pH/µm²	79.279	87.242	57.392	166.660	
$M_{\mathbf{SQUID\text{-}INJ}}$ **– Upper Line:**					
0° order, pH	0.753	3.932	4.600	21.550	
1° order, pH/µm²	0.193	0.876	1.418	0.834	
Lower Line:					
0° order, pH	7.499	3.932	4.600	-	
1° order, pH/µm²	1.854	0.876	1.418	-	
$L_{\mathbf{INJ}}$ **– Upper Line:**					
0° order, pH	1.772	9.485	13.854	22.963	
1° order, pH/µm²	8.893	22.240	28.316	126.990	
Lower Line:					
0° order, pH	11.889	9.485	13.854	-	
1° order, pH/µm²	38.956	22.240	28.316	-	

Table 3.1: Measured quantities and simulated self and mutual inductances for the different SQUIDs.

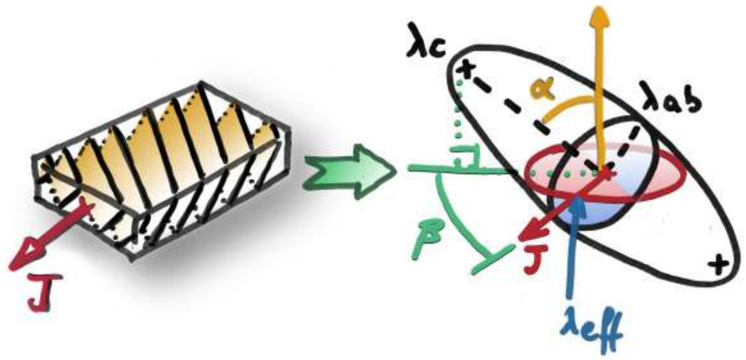

Figure 3.7: Graphical representation of the local current density distribution in a tilted YBCO film (left) and the London penetration depth ellipsoid (right). Employing such ellipsoid, its possible to definite the effective London penetration depth λ_{eff} .

- determinant in the MgO/STO biepitaxial SQUIDs, where the current transport has a very large component in the c-axis direction because of the 45°[100] tilt.

To qualitatively confirm our assumption we try to extract the kinetic inductance contribution from the simulations. Before we do that we need to understand how to deal with the anisotropy of λ_L present in YBCO, which is the cause of the anisotropy in kinetic inductance. We think it is reasonable to define a *London penetration depth ellipsoid*, the axis of which are equal to λ_{ab} and λ_c[3]. At every point of the YBCO crystal where a finite current density $\mathbf{J}$ is present, we can define an *effective London penetration depth* λ_{eff} as the length of the segment which goes from the origin to the intersection of the ellipsoid with the current density direction. A sketchy representation of this idea is given in Figure 3.7.

Indicating with α the [100] tilt — i.e the angle formed by c-axis and the normal to the surface — and with β the angle formed by the current density direction and the projection of the c-axis on the surface of the sample, we can express λ_{eff} as:

$$\lambda_{\text{eff}}^2 = \sum_{\mathbf{e_i}=\hat{a},\hat{b},\hat{c}} \left(\frac{\mathbf{J}\cdot\mathbf{e_i}}{||\mathbf{J}||}\right)\lambda_i^2 = \left(\lambda_{\text{ab}}^2\cos^2\alpha + \lambda_{\text{c}}^2\sin^2\alpha\right)\cos^2\beta + \lambda_{\text{ab}}^2\sin^2\beta$$

The software 3DMSLI, used to simulate the different devices, is not capable of taking into account such anisotropy in London penetration depth

[3]we can consider this ellipsoid as something analog to the inertia ellipsoid, used to describe the motion of a rigid body.

which, at least in theory, is necessary to accurately predict the inductance of any high-T_C SQUID. To avoid this problem, all the SQUIDs have been designed with an elongated structure. In this way, the current density distribution of the SQUID has always one predominant orientation and the simulations done by assigning a single isotropic London penetration depth are still capable of giving reliable results.

By assuming values of λ_c and λ_{ab} close to the ones defined in 1.1, we can calculate λ_{eff} for every device. Moreover the kinetic inductance contribution can be obtained as the product between λ_{eff}^2 and the slope of the linear fit of the simulated injection line self inductance with λ_L^2. The results of all the inductance estimations are summarized in Table 3.2.

For the bicrystal devices, values of λ_{ab} ≈130 nm and λ_{c} ≈1µm are needed to predict the kinetic inductance contribution. These values are in good agreement with the one found in literature[32] for optimally doped YBCO crystals. In the biepitaxial devices the λ_{c} values obtained assuming a λ_{ab} of 150 nm are very close to the ones expected from literature. By fitting linearly the data point (λ_c, T_C) given by Homes and coworkers [32], we have been able to reproduce the T_C of the film measured with an AC susceptometer with good accuracy.
Given that the value of effective London penetration depth makes sense, we can extrapolate a value of SQUID self-inductance and, consequently, extract the junction capacitance. For the bicrystal SQUID YSZ#1 we obtain a junction capacitance of 35 fF while, for the biepitaxial devices, we obtain in both devices junction capacitances smaller than 10 fF. Dividing the estimated capacitance by the product of junction cross section and vacuum dielectric constant ϵ_0 we can extract the ratio t/ϵ_R, where t is the distance between the plates of the parallel plate capacitor of the junction and ϵ_R is the dielectric constant of the material separating the plates. The values of t/ϵ_R obtained in the YSZ devices are much smaller than the one measured by Winkler and coworkers [33], while a comparable value is found for the biepitaxial SQUIDs.

We finally go back to our goal, i.e. designing an all high-T_C single electron transistor. We do this by commenting on the size of an hypothetic square junction realized on the two different technological platforms, i.e. bicrystal and biepitaxial samples, in order to fit the above mentioned resistance and capacitance constrains. A technology is considered unsuitable for SET applications if it is considered not to be possible to realize both:

- superconducting YBCO films thinner than the square junction size, and

Sample Type	YSZ			MgO/STO	
Device ID	**1**	**3**	**5**	**2**	**3**
Junction Width, µm	2.000	1.350	4.890	3.000	3.000
Film Thickness, nm	150.000	150.000	150.000	120.000	120.000
Film Critical Temperature, K		88		87.5	
Extracted Kinetic Inductance					
Kinetic contribution, pH					
Upper Line	**1.026**	**0.133**	**0.131**	×	**271.174**
Lower Line	**2.334**	**0.119**	**0.219**	**-**	**-**
Simulated Kinetic Inductance					
λ_c, **µm**		1.006		2.061	
λ_{ab}, **µm**		0.130		0.150	
ab plane tilt - α, °	12	12	12	45	
current direction - β, °	0	90	90	0	
λ_{eff}, **µm**	0.245	0.130	0.130	1.461	
$\lambda_{\mathrm{eff}}{}^2$	0.060	0.017	0.017	2.135	
$dL_{\mathrm{INJ}}/d\lambda^2$, **pH/µm²**	38.956	22.240	28.316	126.990	
Injector Kinetic Inductance, pH	**2.334**	**0.376**	**0.479**	**271.138**	
SQUID self-Inductance					
λ_{eff}, **µm**	0.245	0.130	0.130	1.461	
L_{SQUID}, **pH**	14.438	14.499	12.939	29.923	
$dL_{\mathrm{SQUID}}/d\lambda_L^2$, **pH/µm²**	79.279	87.242	57.392	166.660	
SQUID loop inductance, pH	19.188	15.973	13.909	385.761	
Extracted Capacitance					
SQUID Loop inductance, pH	19.188	15.973	13.909	385.761	385.761
Estimated Capacitance, fF	35.079	×	×	9.204	8.057
Specific Capacitance, fF/µm²	116.929	×	×	25.567	22.381
t/ϵ, **nm**	0.076	×	×	0.346	0.396
Square Junction size:					
for C **<1 fF, µm**	0.092	×	×	0.198	0.211
for R **>25 kΩ, µm**	0.045	0.036	0.052	0.149	0.135

Table 3.2: Results of Inductance and Capacitance estimations for the different devices.

- junctions whose width is smaller than the square junction size

A square junction with capacitance smaller than 1 fF, has got to have a size smaller than:

- 92 nm in the 12°-tilt YSZ bicrystal technology. Such technology does not fit the requirements for the realization of an high-T_C SET. Higher tilt angles might help to achieve the goal.

- 0.2 µm in the MgO/STO biepitaxial technology. This size is bigger than the film thickness (120 nm) used to realize the devices. We can therefore “trade” the difference between the film thickness and the constraint to gain some junction width, so keep the junction area constant. In other words, with the current technology a junction width of 0.34 µm would be suitable for the SET to fit the Capacitance requirements.

To satisfy the second constraint and have a normal resistance higher than 25 kΩ, a square junction has to be smaller than:

- 45 nm in the bicrystal technology. This size is definitely too small for the High-T_c junction to be realized successfully.

- 140 nm in the biepitaxial technology. This requirement can be fit with the current technology if the junction size is smaller than 170 nm.

We point out that the last estimate is based on the implicit assumption that the junction normal resistance scales inversely with the junction cross-section, like any normal resistor. In the next section we show some measurements performed on SET prototypes which will show that the junction normal resistance constraint can be somehow relaxed.

3.2 SET measurements

The SET prototypes, realized in the YSZ bicrystal chip, have been measured at first both at 6 K and 280 mK. In figure 3.8 the current voltage characteristic of two SETs are shown. Such devices, further indicated as SET#1 and SET#3, had respectively an initial cross section of 0.15×0.6 µm^2 and 0.15×0.8 µm^2. The normal resistance has been found to be lower than 1 kΩ in all devices, a value much lower than the required 50 kΩ. No variation of the current voltage characteristics has been found by sweeping the voltage at the gate electrode, i.e. no modulation due to Coulomb blockade has been observed. Moreover, the estimated capacitance for both devices is

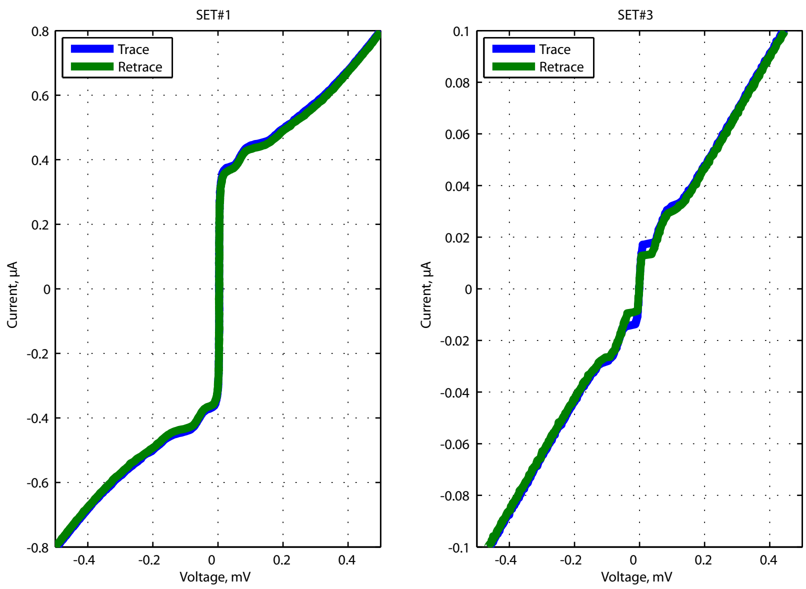

Figure 3.8: Current-voltage characteristic of SET YSZ#1 (left) and YSZ#3 (right) measured at 280 mK before any etching treatment.

bigger than 10 fF, which would make the blockade of tunneling observable at temperatures lower than 84 mK.

To achieve a smaller junction thickness, the device has been etched several times by argon ion milling for few minutes. A Kauffman broad ion beam source has been used for this scope. While etching, the sample has been covered with an aluminum mechanical mask, to avoid the SQUIDs realized on the same chip to be etched away as well. After every etching step the device has been measured at 6 K. The etching-measuring cycle has been stopped when one of the devices – indicated with SET#1 – has developed a resistance higher than 50 kΩ, so that every single junction has a normal resistance higher than the quantum resistance. Figure 3.9 shows the experimental current-voltage characteristic measured of two SET prototypes, measured after every etching step.

No Coulomb blockade has been observed while measuring SET#1 even after the final etching step. No variation in shape or position has been observed in the current-voltage characteristic by the application of a voltage at the gate electrode. A capacitance of 6.7 fF is estimated for the last junction cross section of $0.097 \times 0.6\ \mu m^2$. If any blockade of tunneling is effective in our device, it would be observable at temperatures lower than 138 mK.
We believe that oxygen out diffusion from the YBCO film might be responsible for the loss of superconductivity of the device in the junction region,

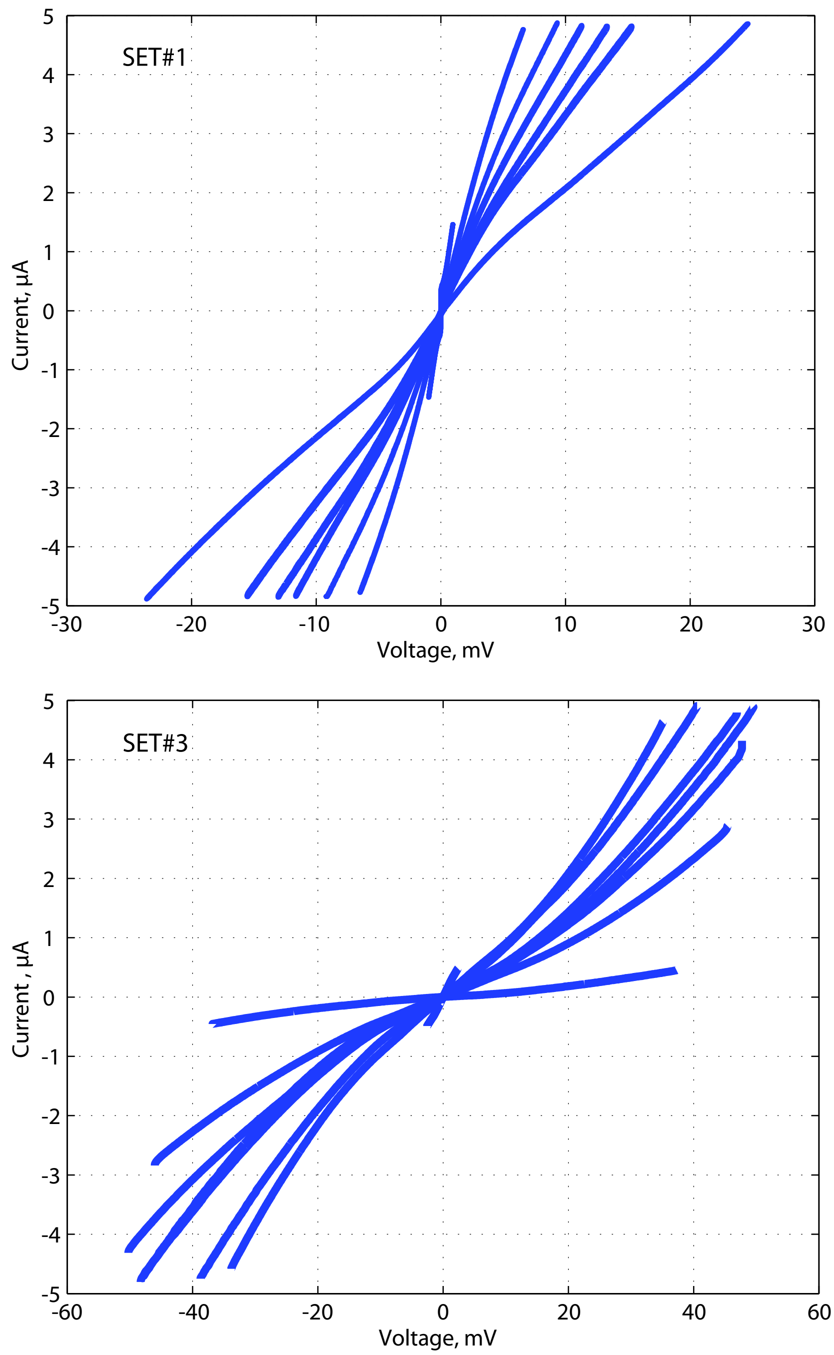

Figure 3.9: Current-voltage characteristic of SET YSZ#1 (top) and YSZ#3 (bottom) measured at 6K after several etching tratments.

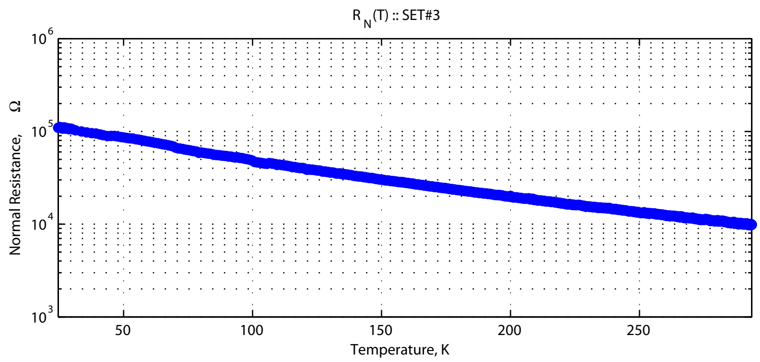

Figure 3.10: $R_N(T)$ of the SET#1 after the last milling step.

causing a transition to an insulating phase. Such transition might be fostered in the last etching step. In support to such observation we show in Figure 3.10 the measurement of the normal resistance while warming up the sample. A clear exponential dependence of the normal resistance is observable, sign of the semiconducting behavior of the junctions caused, perhaps, by a *metal-to-insulator transition*. However, further measurements at lower temperatures could help to verify the existence of the Coulomb blockade.

The data acquired in the etching-measurement cycle can be used to draw some conclusions about the scaling behavior of the normal resistance with the junction size. In order to draw such considerations a relation between etching time and film thickness is needed. An etching rate of 15 Å/min is generally assumed when milling with the settings described in Table C.3. To confirm such etching rate estimate, an AFM image has been taken on the device SET#3 shown in figure 3.11. The YBCO film thickness, measured along the grain boundary position, is about 97 nm. Therefore the above mentioned etching rate can be considered to be reliable. In Figure 3.12 we show the measured behavior of the normal resistance, plotted against both the total etching time and the estimated film thickness.

The SET with smaller junction size has been found to have an increase in resistance almost three times biggeer compared to the other one. To further investigate the scaling behavior of the junction resistance we plot the product $R_N\Sigma$, where R_N is the normal resistance and Σ is the junction cross section. Such product should be theoretically independent on the film thickness if we assume the resistance of junctions to scale according to the following equation:

$$R_N = \rho \frac{l}{\Sigma}$$

where ρ and l are respectively the resistivity and the length of the classical

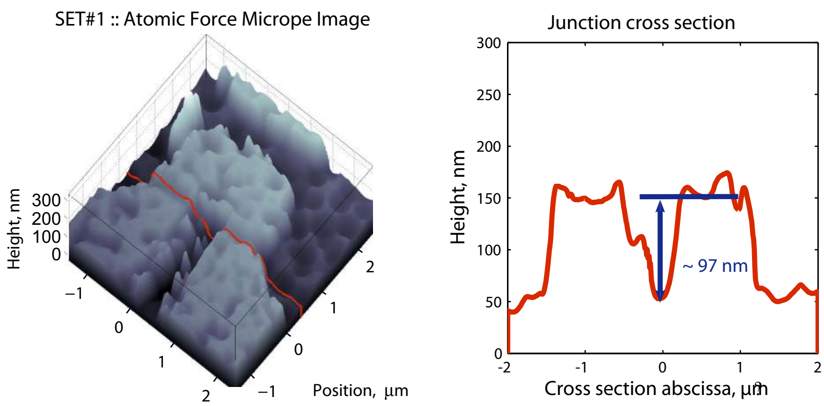

Figure 3.11: Atomic Force micrograph (a) and junction cross section (b) of the device SET#3.

resistor. We will further assume the junction width to be unchanged in the etching process. The scaling behavior of $R_N\Sigma$ with the junction thickness is shown in Figure 3.13 for both devices. According to Figure 3.13 the product $R_N\Sigma$ increases by decreasing the junction cross section , i.e. the normal resistance has the tendency to increase more than expected for a classic resistor. Therefore the SET resistance requirement might be achieved for bigger junction sizes than the ones discussed in the last part of last section and the corresponding junction size limitation might be relaxed.

We remind that the biepitaxial junction are roughly 10 times more resistive than the bicrystal ones. Therefore, reducing the cross section in such junctions might have a bigger impact in the normal resistance, which might be enhanced in a stronger way. If we further assume the biepitaxial junction to scale with the same behavior of SET#1 and take into account the general ratio between the normal resistances in the two different technologies, we might be able to satisfy the 25 kΩ resistance constraint with a junction of cross section 0.3×0.1 µm^2.

We therefore assess the MgO/STO biepitaxial technology as a suitable and very promising technological platform to further develop an all high T_C Single Electron Transistor. We suggest 0.3 µm and 100 nm as suitable junction width and YBCO film thickness for the future realization of a biepitaxial SET prototype. The ion milling procedure or focused ion beam might be further used to shrink the junction thickness and width in case the Coulomb blockade has not been achieved. More systematic investigations on the scaling behavior of the junction normal resistance might be helpful to achieve a better accuracy in the future SET design.

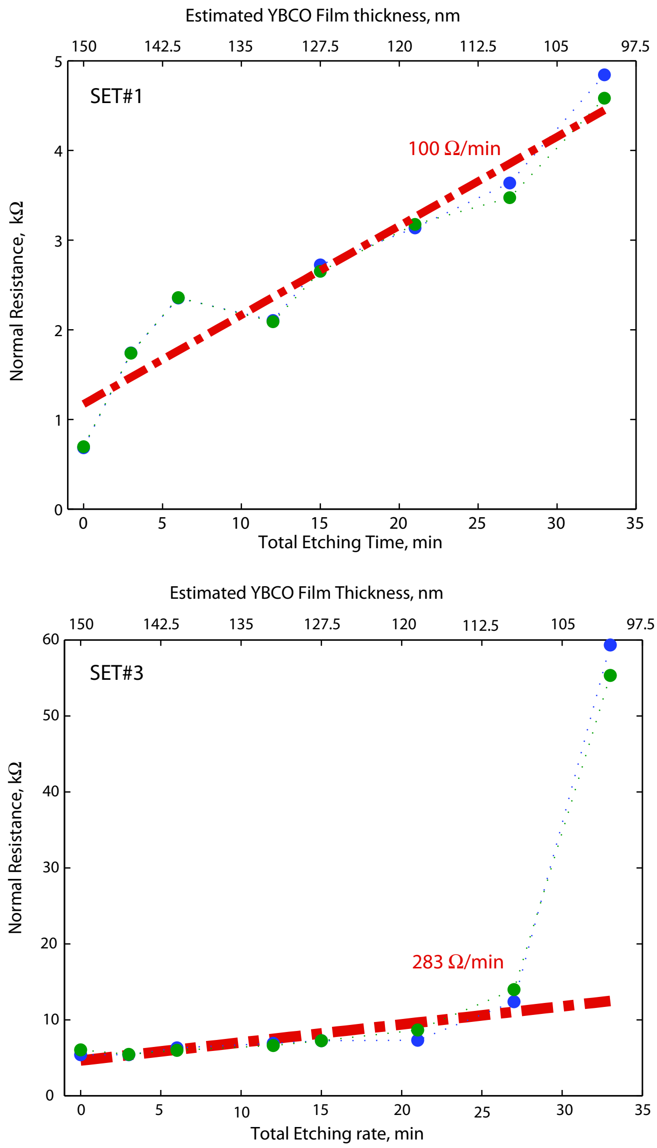

Figure 3.12: Normal resistances of SET YSZ#1 (top) and YSZ#3 (bottom) at different etching times.

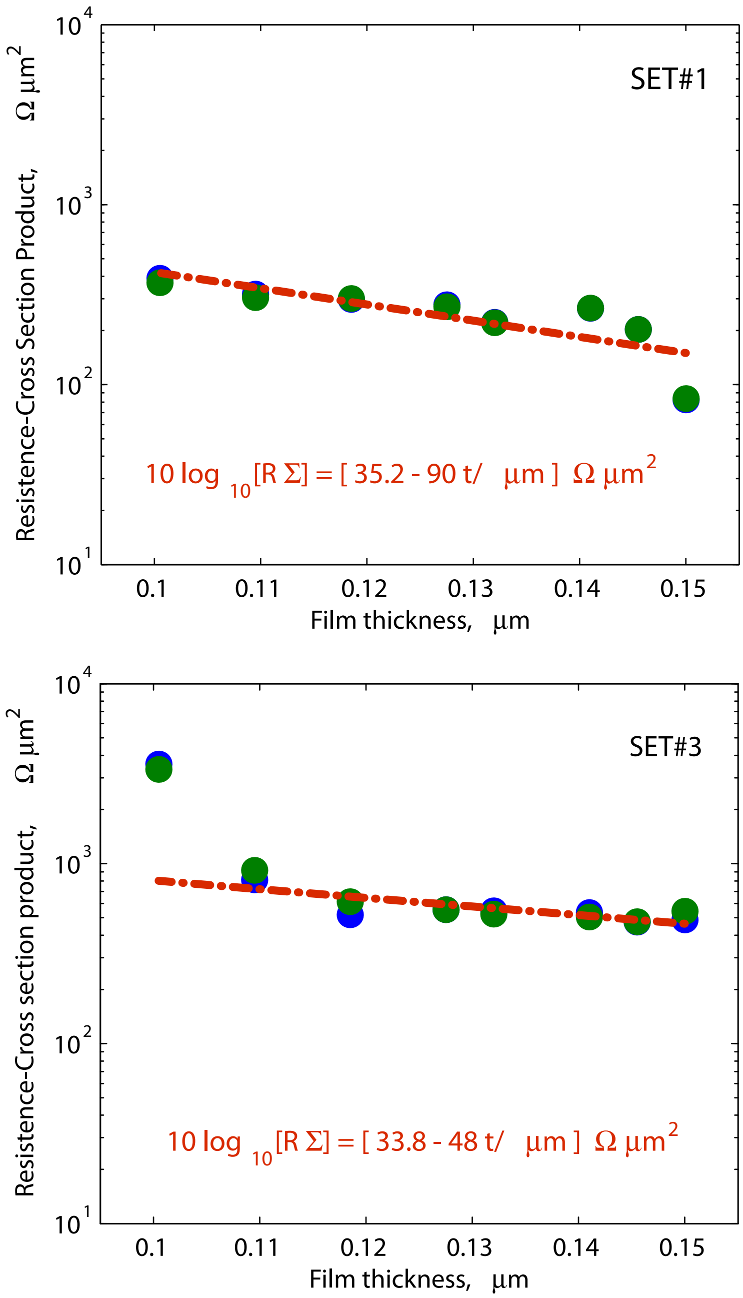

Figure 3.13: Normal Resistance - Cross section product at different junction widths for SET#1 (a) and SET#3 (b).

Chapter 4

Conclusions

This thesis work has been focused on understanding whether two different technologies, used to realize grain boundary Josephson junctions, are suitable for the realization of a single electron transistor (SET).
The importance of realizing an SET with high-T_C superconductors resides on the possibility to measure directly the quasi particle gap in different directions of the momentum space. In particular, such device would permit to directly observe the existence of an imaginary s-wave component of the order parameter in the nodal directions of the d-wave — desired feature for high-T_C phase qubit applications.

$YBa_2Cu_3O_{7-\delta}$ has been used in both the technologies assessed in this work. Such technologies, on the other hand, differ in the way the grain boundary junctions are realized.
In the bicrystal technology the artificial grain boundary is formed because of the different growth direction of the superconducting film in two diversely oriented halves of the substrate — 12°-[100] tilt in both halves, 0°-[001] and 45°-[001] tilt in the two halves of the crystal. In the biepitaxial technology MgO vicinal substrates has been used together with an STO seeding layer. Such technology permits to obtain a bigger [100]-tilt angle of equal to 45°, since the YBCO grows [001] on the bare substrate and [103] on top of the STO seeding layer. YSZ bicrystals and MgO substrates has been used because of the low value of dielectric constant and dielectric losses at radio frequency.

For a single electron transistor to be realized, the Josephson junctions which constitute the device have to satisfy two different constraints. The normal resistance of each junction has to be higher than 25 kΩ while the junction capacitance has to be close to 1 fF. Under such conditions, both quantum and thermal fluctuations will not be able to provide enough energy to perturb the energy level quantization due to charging, i.e. Coulomb blockade of tunneling will play the leading role in charge transport through

the junctions. To extract the capacitance and normal resistance of the grain boundary junctions of this work, we have characterized different DC SQUIDs realized with the two different technologies.
The junction capacitance has been extracted from the voltage at which a current step, caused by SQUID resonance, occurs. Such voltage is related to the product between the SQUID self-inductance and the junction capacitance. The SQUID self-inductance has been estimated indirectly, by measuring the periodicity of the SQUID critical current by applying an injection current through one branch of the interferometer. From this measurement and from the simulation of the SQUID, performed with the 3DMLSI software, it is possible to discriminate between kinetic and geometric contributions of the mutual inductance between SQUID and injection line. The kinetic inductance contribution can be further employed to extract a value of effective London penetration depth, which can be further used to infer the complete SQUID self-inductance. The junction normal resistance has been obtained from the slope of the current-voltage characteristic of the SQUID, measured at high enough bias voltages.

The extracted specific capacitance of the bicrystal SQUIDS has been found to be about 116 fF/μm^2 while, for the biepitaxial SQUIDs, a surprisingly low value of $22 \div 25$ fF/μm^2 has been found. Therefore, to obtain a junction with 1 fF capacitance, the width and the thickness of the junction should be smaller than 92 nm for the bicrystal technology and 200 nm in the biepitaxial technology. The biepitaxial technology seems therefore suitable for the realization of Josephson junctions with small capacitance.
Moreover, the biepitaxial junctions has been found to be very-highly resistive, with $600 \div 700\ \Omega$ normal resistance and cross-section of 0.72 μm^2. The bicrystal junctions appear to be much more conductive, with resistances of about 80 Ω for a 0.6 μm^2 cross-section junction. Consequently, the resistance constraint can be satisfied more easily — with bigger junction cross-section — in the biepitaxial technology. Measurements performed on bicrystal SET prototypes have revealed that the junction resistance can be increased more than expected for a normal tunneling junction. The product cross-section normal resistance, whose value should be cross section independent, is increased when decreasing the cross section of the junction. This effect could further help to achieve the high resistance 25 kΩ goal.

We asses the MgO/STO biepitaxial technology as a suitable and promising platform for the realization of high-T_C single electron transistor. We suggest 300 nm$\times$120 nm as a good cross-section size to realize such devices.

Appendix A

Electron beam lithography

Reference crosses and alignment rulers are defined in the `RUL` layer, exposed in 5^{th} lens mode to obtain an high resolution. The bonding pads structure, defined in the `PAD` layer, has been exposed with the 4^{th} lens at high current to make the exposure fast. These layers have been exposed in the lithography step.
SQUIDs and SETs structures, shown in Figure 2.6 and 2.10, have been defined in the `SDQ` and `SET` layers respectively, to make possible an independent dose optimization. Both layers structures has been exposed in the same lithography steps in 5^{th} lens. Finally the leads, defined in the `CNN` layer, have been exposed with the 4^{th} lens with high current.

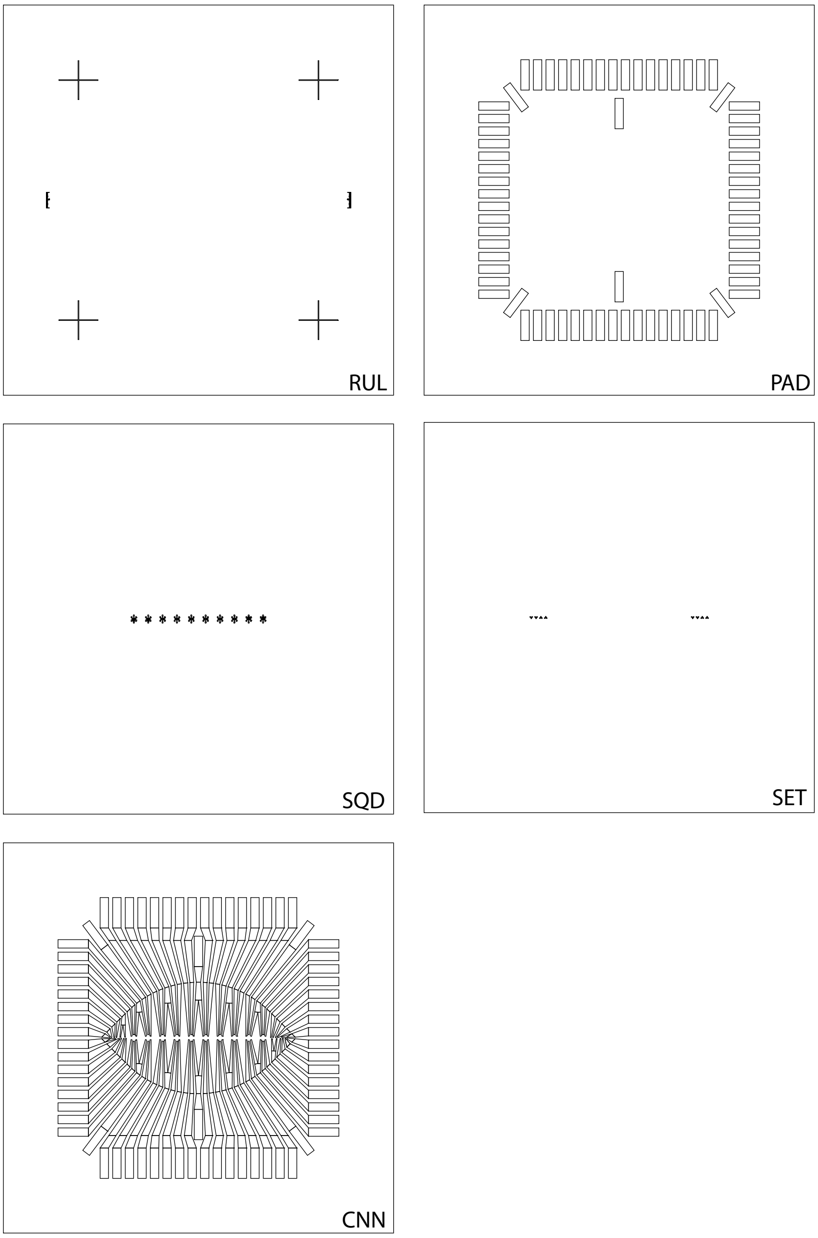

Figure A.1: Layers as defined in AutoCAD file. The injection line of neighbor couple of SQUIDS are connected joined to in the same pad. To allow a single SQUID measurement, such lines has been cut by Focused Ion Beam.

Layer	RUL	PAD	CNN	SET	SQD
Current	100 pA	10 nA	10 nA	40 pA	40 pA
Base Dose, µC/cm^2	90	90	90	90	90
Lens	5	4	4	5	5
EOS	8,7	4,7	4,7	7,7	7,7
# Step / µm	400	40	40	400	400
Field Size, µm	70	700	700	70	70
SubField Size, µm	10	100	100	70	70
PREAD step , µm	0.01	0.1	0.1	0.005	0.005
PREAD resize , µm	0.005	0.05	0.05	0.0025	0.0025
Min Modulation step, %	5.56	5.56	5.56	8.89	8.89
Max Modulation, %	3200	3200	3200	3200	3200
Max Dos, µC/cm^2	2970	2970	2970	3200	3200

Table A.1: Settings used for to expose different e-beam patterns.

Appendix B

Lift-off

Before every lithography the sample has been cleaned in Acetone and Isopropanol and blown dry with Nitrogen. PMMA(8,5)MAA EL10 Copolymer has been used as bottom layer while, for the top one, ZEP520 resist diluted 1:2 in Anisole has been the choice. After the e-beam exposure, the ZEP layer is developed in Oxylene while The bottom layer can be fully developed using ECA in solution 1:5 with Ethanol. Both developments are stopped by rinsing in Isopropanol. The whole resist handling procedure is summarized in Table B.2.
To execute the lift-off the sample is put in a low power ultrasonic bath of Shipley 1165 resist remover or Acetone at 60 °C. The sample is inspected at the optical microscope, to ensure that all the liftoff metal has been removed and, if necessary, the ultrasonic bath is repeated. The sample is then rinsed in Isopropanol and blown dry in nitrogen.

E-beam evaportion	**Au**	**a-C**	**Cr**
Base pressure, mbar	10^{-5}	10^{-7}	10^{-5}
Deposition rate, Å/s	5	1	$3-5$
Film thickness, nm	2400	1200	500

Table B.1: Parameters used in the E-beam evaporation steps.

Resist Layer	**Bottom**	**Top**
Resist	P(MMA)MAA 1:10 EL	ZEP 1:2 Anisole
Spinner Speed, r/min	4000	4000
Spinning Time, min	1	1
Baking Temperature, °C	135	135
Baking Time, min	5	10
Resist Thickness, nm	~ 400	~ 100
Developer	Oxylene	ECA 1:5 Ethanol
Developing time	45 s	7 min
Rinser	Isopropanol	Isopropanol

Table B.2: Parameters used for e-beam resist spin-coating, soft-baking and development.

Appendix C

Other fabrication parameters

We gather here some tables that summarize the parameters used in the Laser ablation deposition, Kauffman Source Argon Ion Milling and Plasma Etching steps.

PLD deposition	**STO**	**YBCO**
Heater Temperature, °C	680	760
Base pressure, mbar	10^{-6}	10^{-6}
Working pressure, mbar	0.2	0.6
Laser pulse frequency, Hz	10	10
Film thickness, nm	30	$100-150$

Table C.1: PLD deposition parameters of STO and YBCO films on MgO substrates for the fabrication of biepitaxial samples.

Plasma treating	**Ashing**	**C-stripping**
Power	50 W	50 W
Pressure	250 mbar	100 mbar
Oxygen pressure	10 cm^3/min	10 cm^3/min
Processing time	15 s	30 min

Table C.2: Parameters used in the plasma treating steps.

Milled Material	**STO**	**YBCO**	**Au**
Voltage, V	300	300	300
Current, mA	15	7	7
Base Pressure, mbar	$2 - 3 \times 10^{-7}$	$2 - 3 \times 10^{-7}$	$2 - 3 \times 10^{-7}$
Working pressure, mbar	2.3×10^{-4}	2.3×10^{-4}	2.3×10^{-4}
Milling angle, °	5	3.5	3.5
Rotation, r/min	3	3	3

Table C.3: Parameters used in the Kauffman-source Argon Ion Milling steps. The YBCO etching rate with such settings is about 15 Å/min. To achieve a low pressure in the chamber an *outgassing procedure* is followed, i.e. the filaments which ignite the Ar^+ Plasma as well as the neutralizer filament are heated up with a current of 7 A for 120 min.

Bibliography

[1] J. R. Kirtley, C. C. Tsuei, J. Z. Sun, C. C. Chi*, Lock See Yu-Jahnes, A. Gupta, M. Rupp, and M. B. Ketchen. Symmetry of the order parameter in the high-tc superconductor $yba_2cu_3o_{7-\delta}$. *Nature*, 373:225, 1995.

[2] C. C. Tsuei and J. R. Kirtley. Pairing symmetry in cuprate superconductors. *Review of Modern Physics*, 72:969, 2000.

[3] H. J. H. Smilde, A. A. Golubov, Ariando, G. Rijnders, J. M. Dekkers, S. Harkema, D. H. A. Blank, H. Rogalla, and H. Hilgenkamp. Admixtures to d-wave gap symmetry in untwinned $yba_2cu_3o_{7-\delta}$ superconducting films measured by angle-resolved electron tunneling. *Physical Review Letters*, 95:257001, 2005.

[4] M. B. Walker and J. Luettmer-Strathmann. Josephson tunneling in high-t_c superconductors. *Physical Review B*, 54:588, 1996.

[5] M. K. Wu, J. R. Ashburn, C. J. Torng, P. H. Hor, R. L. Meng, L. Gao, Z. J. Huang, Y. Q. Wang, and C. W. Chu. Superconductivity at 93 k in a new mixed-phase yb-ba-cu-o compound system at ambient pressure. *Physical Review Letters*, 58:908, 1987.

[6] T. Van Duzer and C. W. Turner. *Superconductive Devices and Circuits*. Prantice Hall, 1998.

[7] M. Tinkham. *Introduction to Superconductivity*. McGraw Hill, 1996.

[8] B.D. Josephson. Possible new effect in superconducting tunneling. *Physics Letters*, 1:251, 1962.

[9] P. W. Anderson and J. M.Rowell. Probable observation of the josephson superconducting tunneling effect. *Physical Review Letters*, 10:230, 1963.

[10] R.P.Feynman, R.B.Leighton, and M.Sands. *The Feynman Lectures on Physics*, volume 3. Addison-Wesley, 1965.

[11] W.C. Stewart. Current-voltage characteristics of josephson junctions. *Applied Physics Letters*, 12:277, 1968.

[12] D.E. McCumber. Tunneling and weak-link superconductor phenomena having potential device applications. *Journal of Applied Physics*, 39:2503, 1968.

[13] D.E. McCumber. Effect of an ac impedence on dc voltage-current characterisitcs of superconductor weak-link junctions. *Journal of Applied Physics*, 39:3113, 1968.

[14] W. J. Johnson. *Non linear wave propagation on superconducting tunneling junctions*. PhD thesis, University of Wisconsin, Madison, 1968.

[15] T.A. Fulton. Quantum interference and supercurrent-phase relations in weak-link junctions. *Solid State Communications*, 8:1353, 1970.

[16] T.A. Fulton, L.N. Dunkleberger, and R.C. Dynes. Quantum interference properties of double josephson junctions. *Physical Review B*, 6:855, 1972.

[17] M. Sigrist and T.M. Rice. Paramagnetic effect in high-t_c superconductors – a hint for d-wave superconductivity. *Journal of the Physical Society of Japan*, 61:4283, 1992.

[18] F. Lombardi, F. Tafuri, F. Ricci, F. Miletto Granozio, A. Barone, G. Testa, E . Sarnelli, J. R. Kirtley, and C. C.Tsuei. Intrinsic d-wave effects in $yba_2cu_3o_{7-\delta}$ grain boundary josephson junctions. *Physical Review Letters*, 20:207001, 2002.

[19] T. Bauch, T. Lindstrm, F. Tafuri, G. Rotoli, P. Delsing, T. Claeson, and F. Lombardi. Quantum dynamics of a d-wave josephson junction. *Science*, 311:57, 2006.

[20] E.J. Tarte, G.A. Wagner, R.E. Somekh, F.J. Baudenbacher, P. Berghuis, and J.E. Evetts. The capacitance of bicrystal josephson junctions deposited on $srtio_3$ substrates. *IEEE Transactions on Applied Superconductivity*, 10:3662, 1997.

[21] P. F. McBriena, R. H. Hadfielda, W. E. Booija, A. Moyaa, F. Kahlmanna, M. G. Blamirea, C. M. Pegrumb, and E. J. Tarte. The capacitance of grain boundaries in superconducting films with strontium titanate and other substrates. *Physica C*, 339:88, 2000.

[22] R. J. Schoelkopf, P. Wahlgren, A. A. Kozhevnikov, P. Delsing, and D. E. Prober. The radio-frequency single-electron transistor(rf-set): A fast and ultrasensitive electrometer. *Science*, 280:1238, 1998.

[23] D.B. Tuckerman and J.H. Magerlein. Resonances in symmetric josephson interferometers. *Journal of Low Temperature Physics*, 101:1099, 1995.

[24] H.H. Zappe and B.S. Landman. Analysis of resonance phenomena in josephson interferometer devices. *Journal of Applied Physics*, 49:334, 1978.

[25] H. Hilgenkamp and J. Mannhart. Grain boundaries in high-t_c superconductors. *Review of Modern Physics*, 74:485, 2002.

[26] F. Tafuri, F. Miletto Granozio, F. Carillo, A. Di Chiara, K. Verbist, and G. Van Tendeloo. Microstructure and josephson phenomenology in 45 tilt and twist $yba_2cu_3o_{7-\delta}$ artificial grain boundaries. *Physical Review B*, 59:11523, 1999.

[27] Julia M. Phillips. Substrate selection for high-temperature superconducting thin films. *Journal of Applied Physics*, 79:1829, 1996.

[28] J. Johansson, K.Cedergren, T.Bauch, and F.Lombardi. Properties of magnetic penetration depth in (103) oriented $yba_2cu_3o_{7-\delta}$ thin films. *Private comunications*, 2007.

[29] M. M. Khapaevy, M. Yu Kupriyanovz, E. Goldobin, and M. Siegel. Current distribution simulation for superconducting multi-layered structures. *Superconductor Science and Technology*, 16:24, 2003.

[30] P. Larsson, B. Nilsson, and Z. G. Ivanov. Fabrication and transport measurements of $yba_2cu_3o_{7-\delta}$ nanostructures. *Journal of Vacuum science and Technology*, 18:25, 2000.

[31] F. Pobell. *Matter and Methods at Low Temperatures*. Springer, 1996.

[32] C.C. Homes, S.V.Dordevic, D.A. Bonn, R. Liang, W.N. Hardy, and T.Timusk. Coherence, incoherence and scaling along the c-axis of $yba_2cu_3o_{7-\delta}$. *Physical Review B*, 71:184515, 2005.

[33] D.Winkler, Y.M.Zhang, P.Å. Nilsson, E.A. Stepantsov, and T.Claeson. Electromagnetic properties at the grain boundary interface of a $yba_2cu_3o_{7-\delta}$ bicrystal jospehson junction. *Physical Review Letters*, 72:1260, 1994.

Acknowledgments

I would like to thank...
...very much Floriana Lombardi, Thilo Bauch for their great leadership and guidance all along the thesis work
...Jesper Johansson, Karin Cedergren, Daniela Stornaiuolo, for introducing me and for the help along the fabrication processes
...David Gustafsson and Shahid Nawaz for providing me the data of the wonderful biepitaxial SQUIDs
...Evgeniy Stepantsov for providing me the YSZ bicrystals
...Thilo Bauch for the help with the measurements
...Thilo Bauch, Samuel Lara Avila, Justin Schneiderman, Mikael Fogelström and John Kirtley for the fruitful discussions, suggestions and support
...Floriana Lombardi, Ermanno Pinotti and Thilo Bauch for carefully reviewing this manuscript
...Jonas Westberg for his support with LaTeX
...Everybody at the Nanofabrication Laboratory in MC2 for their support all along the cleanroom activity; Bengt Nilsson, Piotr Jedrasik and Sergeiy Kubatkin for the patience and support with the JEOL e-beam system
...Staffan Pherson, Henrik Engseth for the help with the aluminum mechanical masks and FIB chip carrier
...Mattias Torstensson for the help with the FIB operation and with the informatics support
...the newborn Sofia Kubatkin, for adding the little potions of her meal in my thesis drafts
...everybody that I wish I remembered but I forgot mentioning in this page, and everybody I misspelled the name of, for their patience.